

**A NOVEL CAD ALGORITHM FOR THE ANALYSIS  
OF PRINTED GEOMETRIES**

A DISSERTATION  
SUBMITTED TO THE DEPARTMENT OF ELECTRICAL AND  
ELECTRONICS ENGINEERING  
AND THE INSTITUTE OF ENGINEERING AND SCIENCE  
OF BILKENT UNIVERSITY  
IN PARTIAL FULFILLMENT OF THE REQUIREMENTS  
FOR THE DEGREE OF  
DOCTOR OF PHILOSOPHY

THESIS  
TA  
174  
K56  
1997

By  
Hoyan Kmayman  
May 1997

A NOVEL CAD ALGORITHM FOR THE ANALYSIS  
OF PRINTED GEOMETRIES

A DISSERTATION  
SUBMITTED TO THE DEPARTMENT OF ELECTRICAL AND ELECTRONICS  
ENGINEERING  
AND THE INSTITUTE OF ENGINEERING AND SCIENCE  
OF BILKENT UNIVERSITY  
IN PARTIAL FULFILLMENT OF THE REQUIREMENTS  
FOR THE DEGREE OF  
DOCTOR OF PHILOSOPHY

By

Noyan Kinayman

May 1997

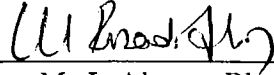
---

*Noyan Kinayman*

TA  
174  
.K56  
1937

B037971

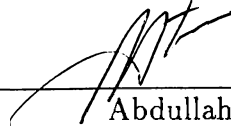
I certify that I have read this thesis and that in my opinion it is fully adequate, in scope and in quality, as a dissertation for the degree of Doctor of Philosophy.



---

M. I. Aksun, Ph. D. (Supervisor)

I certify that I have read this thesis and that in my opinion it is fully adequate, in scope and in quality, as a dissertation for the degree of Doctor of Philosophy.



---

Abdullah Atalar, Ph. D.

I certify that I have read this thesis and that in my opinion it is fully adequate, in scope and in quality, as a dissertation for the degree of Doctor of Philosophy.

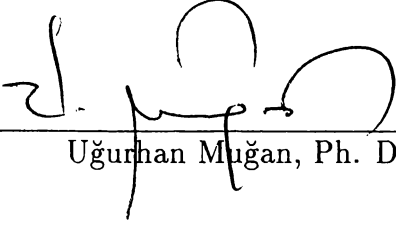


---

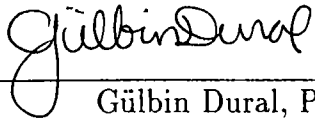
Levent Gürel, Ph. D.




I certify that I have read this thesis and that in my opinion it is fully adequate, in scope and in quality, as a dissertation for the degree of Doctor of Philosophy.

  
Uğurhan Muğan, Ph. D.

I certify that I have read this thesis and that in my opinion it is fully adequate, in scope and in quality, as a dissertation for the degree of Doctor of Philosophy.

  
Gülbin Dural, Ph. D.

Approved for the Institute of Engineering and Science:

  
Mehmet Baray, Ph.D.  
Director of Institute of Engineering and Science

*To my mother and father*

# Abstract

## A NOVEL CAD ALGORITHM FOR THE ANALYSIS OF PRINTED GEOMETRIES

Noyan Kinayman

Ph. D. in Electrical and Electronics Engineering

Supervisor:

Assoc. Prof. M. I. Aksun

May 1997

An efficient and accurate computer aided design (CAD) software for the electromagnetic simulation of passive microwave components, fabricated in planar stratified media, is developed in this work. The numerical technique employed in this software is based on the spatial-domain method of moments (MoM) in conjunction with the closed-form Green's functions. Since the computational efficiency is a major issue in CAD softwares, the spatial-domain MoM is significantly improved in this respect with the use of the closed-form Green's functions and closed-form expressions for the MoM matrix entries. Vertical metalizations in the form of via holes and shorting pins, which are the indispensable parts of the most microwave circuits, are also modeled very efficiently and incorporated into this formulation. The resulting approach is applied to some realistic microwave circuits and planar antennas, with and without vertical metalizations, to validate the formulation. It is also demonstrated that the formulation developed in this work can be efficiently used with an optimization algorithm for design purposes. The results obtained from the formulation proposed in this work are compared to those obtained from a commercial electromagnetic analysis software.

**Keywords:** CAD, Printed structures, Full-wave EM analysis, Planarly layered media, Green's functions, Method of moments

# Özet

## DÜZLEMSEL GEOMETRİLERİN ANALİZİ İÇİN YENİ BİR CAD ALGORİTMASI

Noyan Kınayman  
Elektrik ve Elektronik Mühendisliği Doktora

Tez Yöneticisi:  
Doçent Doktor M. I. Aksun  
Mayıs 1997

Bu çalışmada, düzlemsel çok katmanlı ortamlardaki pasif mikrodalga devrelerinin elektromanyetik simülasyonu için hızlı ve hassas bir bilgisayar destekli tasarım yazılımı geliştirilmiştir. Bu yazılımda kullanılan sayısal tekniğin temelini kapalı formdaki Green's fonksiyonları ile birlikte kullanılan uzay boyutu moment metodu oluşturmaktadır. Analiz hızı, bilgisayar destekli tasarım yazılımlarında önemli bir özellik olduğu için, uzay boyutundaki moment metodu kapalı formdaki Green's fonksiyonları ve matris elemanları kullanılarak oldukça iyileştirilmiştir. Kısa devre bağlantıları ve katmanlar arası geçişi sağlayan bağlantılar şeklindeki düşey metalizasyonlar da verimli bir şekilde modellenmiş ve formülasyona dahil edilmiştir. Elde edilen yazılım, formülasyonu doğrulamak amacıyla, düşey metalizasyon da içeren bazı gerçekçi mikrodalga devrelerine ve düzlemsel antenlere uygulanmıştır. Bu çalışmada geliştirilen formülasyonun bir optimizasyon algoritması ile verimli olarak kullanılabilceği de gösterilmiştir. Bu çalışmada önerilen formülasyondan elde edilen sonuçlar, bu alanda kullanılan ticari bir programın sonuçları ile karşılaştırılmıştır.

**Anahtar** Bilgisayar destekli tasarım, Tam-dalga EM analizi, Düzlemsel çok  
**Sözcükler:** katmanlı ortam, Green's fonksiyonları, Moment metodu

# Acknowledgment

I would like to express my deepest gratitude to Assoc. Prof. M. I. Aksun for his supervision and encouragement in all steps of the development of this work.

My special thanks go to my colleague Lale Alatan for inspiring discussions on many topics in this thesis, and Aydın Alatan for his invaluable helps during my study.

And my dear friends, I was not able to list the names of all of you here, please forgive me about that. Müşerref, Şükrü, and Feyza, it was your continuous encouragement which gave me a great moral support.

I am grateful to the members of my rock band for sharing many pleasant moments with me. Making music has always been a kind of “discharge” for me.

Finally, my sincere thanks go to my family for their love and patience throughout my graduate study. It is their unhesitating self-sacrifice which has enabled me to achieve my goals in my life.



# Contents

## Acknowledgment

Contents	i
List of Figures	iv
List of Tables	viii
<b>1 Introduction</b>	<b>1</b>
1.1 A Brief Review of the Analysis Methods of Printed Structures . . .	2
<b>2 Green's Functions in Planarly Layered Media</b>	<b>5</b>
2.1 Green's Functions in Spectral Domain	6
2.1.1 Horizontal electric dipole (HED) . . . . .	9
2.1.2 Vertical electric dipole (VED) . . . . .	11
2.1.3 Green's functions for electric and magnetic dipoles . . . . .	12
2.2 Closed-form Green's Functions in Spatial Domain . . . . .	14
2.3 Conclusions . . . . .	18
<b>3 Field Analysis in Planarly Layered Media</b>	<b>19</b>
3.1 MPIE Formulation in Planarly Layered Media . . . . .	20
3.1.1 Difficulties and Solutions . . . . .	24
3.1.2 Singularities Encountered in the Application of MoM . . . . .	29
3.2 The Method of De-embedding of the Port Discontinuities . . . . .	31
3.3 Numerical Examples . . . . .	33

3.3.1	Microstrip Patch Antenna . . . . .	35
3.3.2	Microstrip Corner . . . . .	38
3.3.3	Proximity Coupled Microstrip Patch Antenna . . . . .	42
3.3.4	Microstrip Patch Antenna with Parasitic Elements	45
3.3.5	Four-pole Elliptic Band-pass Filter . . . . .	45
3.3.6	3 dB 90° Hybrid Coupler . . . . .	46
3.3.7	Coupled-line Band-pass Filter . . . . .	51
3.3.8	Interdigital MIC Capacitor . . . . .	51
3.3.9	Short-circuited Microstrip Line	56
3.3.10	Air Bridge . . . . .	57
3.3.11	Short-circuited Microstrip Patch Antenna	58
3.3.12	Square-spiral MIC Inductor . . . . .	61
3.4	Conclusions . . . . .	64
<b>4</b>	<b>Methods for Improving the Analysis Time</b>	<b>65</b>
4.1	Evaluation of the MoM Matrix Entries . . . . .	68
4.1.1	Numerical Examples . . . . .	69
4.2	Interpolating Frequency Data . . . . .	78
4.2.1	Numerical Examples . . . . .	80
4.3	Conclusions . . . . .	83
<b>5</b>	<b>Optimization</b>	<b>84</b>
5.1	Genetic Algorithms . . . . .	85
5.2	Numerical Examples . . . . .	87
5.3	Conclusions . . . . .	92
<b>6</b>	<b>Conclusions</b>	<b>93</b>
<b>A</b>	<b>Explicit Forms of the Green's Functions</b>	<b>95</b>
A.1	The Green's function $\tilde{G}_z^q$ . . . . .	95
A.2	The Green's function $\tilde{G}_{zz}^A$ . . . . .	96
A.3	The Green's function $\tilde{G}_{zx}^A$	96

A.4	The Green's function $\tilde{G}_x^q$ . . . . .	97
<b>B</b>	<b>Evaluation of the Inner Products</b>	<b>98</b>
B.1	Evaluation of $\left\langle \frac{\partial}{\partial z} T_{zm}, G_x^q * \frac{\partial J_{zn}}{\partial x} \right\rangle$ . . . . .	98
B.2	Evaluation of $\left\langle \frac{\partial}{\partial x} T_{xm}, G_z^q * \frac{\partial J_{zn}}{\partial z} \right\rangle$ . . . . .	99
B.3	Evaluation of $\left\langle \frac{\partial}{\partial z} T_{zm}, G_z^q * \frac{\partial J_{zn}}{\partial z} \right\rangle$ . . . . .	100
B.4	Evaluation of $\left\langle T_{zm}, G_{zz}^A * J_{zn} \right\rangle$ . . . . .	101
B.5	Evaluation of the other terms . . . . .	101
<b>C</b>	<b>Generalized Pencil of Function Algorithm</b>	<b>102</b>
<b>D</b>	<b>Method of Moments</b>	<b>108</b>
D.1	Variational Interpretation . . . . .	109
<b>E</b>	<b>Series Acceleration Methods Used in EM</b>	<b>112</b>
E.1	The Transformation Methods . . . . .	113
E.1.1	Euler's Transformation . . . . .	114
E.1.2	Shanks' Transformation . . . . .	114
E.1.3	Method of Averages . . . . .	116
E.1.4	The $\Theta$ Algorithm . . . . .	117
E.1.5	The Chebyshev-Toeplitz Algorithm . . . . .	117
E.1.6	The Poisson Transformation . . . . .	118
E.1.7	Ewald's Transformation . . . . .	119
E.1.8	Kummer's Transformation . . . . .	120
E.1.9	Method of Exponentials . . . . .	121
E.2	Results and Discussion . . . . .	122
E.2.1	Integration Involving Bessel Functions . . . . .	122
E.2.2	Free-Space Periodic Green's Functions . . . . .	126
E.2.3	Quasi-Dynamic Green's Function . . . . .	129
E.3	Conclusion . . . . .	130
<b>Vita</b>		<b>143</b>

# List of Figures

2.1	A general source placed in a planarly stratified medium.	7
2.2	The path used in exponential approximation. . . . .	16
3.1	A typical multilayer printed geometry. . . . .	20
3.2	Basis functions used for horizontal and vertical connections in the MoM solution. . . . .	22
3.3	Cross-section of a planar circuit with a vertical connection showing the discontinuous basis functions. . . . .	30
3.4	Meaning of $\varepsilon_{eff}$ for a microstrip transmission line. . . . .	34
3.5	Typical gridding which is used in the simulation software. . . . .	35
3.6	Geometry of a patch antenna. . . . .	36
3.7	$\Gamma_{in}$ of the patch antenna shown in Fig. 3.6. Frequency increases in the clock-wise direction ( $f_{start}=2200$ MHz, $f_{stop}=2400$ MHz). . . . .	37
3.8	$x$ -directed current density of the patch antenna shown in Fig. 3.6 at $f = 2300$ MHz. . . . .	38
3.9	$y$ -directed current density of the patch antenna shown in Fig. 3.6 at $f = 2300$ MHz. . . . .	39
3.10	Geometry of a microstrip corner. . . . .	40
3.11	Magnitude of $S_{11}$ of the microstrip corner shown in Fig. 3.10. . . . .	40
3.12	Phase of $S_{11}$ of the microstrip corner shown in Fig. 3.10. . . . .	41
3.13	Equivalent lumped circuit model of the microstrip corner shown in Fig. 3.10. . . . .	42
3.14	Geometry of a proximity coupled patch antenna. . . . .	43

3.15	$\Gamma_{in}$ of the proximity coupled patch antenna shown in Fig. 3.14. Frequency increases in the clock-wise direction ( $f_{start}=3000$ MHz, $f_{stop}=4000$ MHz). . . . .	44
3.16	Equivalent lumped circuit model of the proximity coupled patch antenna shown in Fig. 3.14. . . . .	44
3.17	Geometry of the microstrip patch antenna with parasitics. . . . .	46
3.18	Input VSWR of the microstrip patch antenna with parasitics shown in Fig. 3.17. . . . .	47
3.19	Geometry of a band-pass filter. . . . .	48
3.20	Magnitude of $S_{11}$ of the band-pass filter shown in Fig. 3.19 for different $s$ values. . . . .	48
3.21	Magnitudes of $S_{11}$ and $S_{21}$ of the band-pass filter shown in Fig. 3.19 for $s=0.175$ cm. . . . .	49
3.22	Geometry of a hybrid coupler. . . . .	49
3.23	Magnitudes of $S_{13}$ and $S_{14}$ of the hybrid coupler shown in Fig. 3.22. . . . .	50
3.24	Phases of $S_{13}$ and $S_{14}$ of the hybrid coupler shown in Fig. 3.22. . . . .	50
3.25	Geometry of a multilayer band-pass filter. . . . .	51
3.26	Magnitudes of $S_{11}$ and $S_{21}$ of the band-pass filter shown in Fig. 3.25. . . . .	52
3.27	Phases of $S_{11}$ and $S_{21}$ of the band-pass filter shown in Fig. 3.25. . . . .	52
3.28	Geometry of an interdigital MIC capacitor. . . . .	53
3.29	Magnitudes of $S_{11}$ and $S_{21}$ of the MIC capacitor shown in Fig. 3.28. . . . .	54
3.30	Phases of $S_{11}$ and $S_{21}$ of the MIC capacitor shown in Fig. 3.28. . . . .	54
3.31	Magnitudes of $S_{11}$ and $S_{21}$ of the MIC capacitor shown in Fig. 3.28. . . . .	55
3.32	Equivalent lumped circuit model of the interdigital capacitor shown in Fig. 3.28. . . . .	56
3.33	Geometry of a short-circuited microstrip line. . . . .	57
3.34	Current distribution on the microstrip line shown in Fig. 3.33 with a single shorting pin. . . . .	58
3.35	Current distribution on the microstrip line shown in shown in Fig. 3.33 with three shorting pins. . . . .	59
3.36	Geometry of an air bridge. . . . .	59



3.37	Magnitude of $S_{11}$ of the air bridge shown in Fig. 3.36. . . . .	60
3.38	Phase of $S_{11}$ of the air bridge shown in Fig. 3.36. . . . .	60
3.39	Geometry of a shorted microstrip patch antenna. . . . .	61
3.40	Resonant frequency of the patch antenna, shown in Fig. 3.39, vs. shorting pin location. . . . .	62
3.41	Geometry of a MIC square-spiral inductor. . . . .	63
3.42	Magnitude of the input impedance of the MIC inductor shown in Fig. 3.41. . . . .	63
4.1	Flow-chart of the hybrid method for evaluating the MoM matrix entries. . . . .	70
4.2	Matrix fill-time vs. auxiliary parameter $s$ for the patch antenna. .	71
4.3	Magnitude of the input impedance of the patch antenna for different values of $s$ . . . . .	72
4.4	Phase of input impedance of the patch antenna for different values of $s$ . . . . .	73
4.5	Mean matrix fill-time vs. auxiliary parameter $s$ for the interdigital capacitor. . . . .	74
4.6	Magnitudes of $S_{11}$ and $S_{21}$ of the interdigital capacitor for different values of $s$ . . . . .	75
4.7	Phases of $S_{11}$ and $S_{21}$ of the interdigital capacitor for different values of $s$ . . . . .	76
4.8	Magnitudes of $S_{11}$ and $S_{21}$ of the interdigital capacitor for different number of sampling points. . . . .	76
4.9	Magnitudes of $S_{11}$ and $S_{21}$ of the interdigital capacitor for different number of sampling points and interpolation scheme. . . . .	77
4.10	Flow-chart of the frequency interpolation. . . . .	79
4.11	Magnitude of $S_{11}$ of the patch antenna shown in Fig. 3.6 (exact:21 points, interpolated:7 points). . . . .	80
4.12	Phase of $S_{11}$ of the patch antenna shown in Fig. 3.6 (exact:21 points, interpolated:7 points). . . . .	81

4.13	Magnitudes of $S_{11}$ and $S_{21}$ of the band-pass filter shown in Fig. 3.25 (exact:41 points, interpolated:15 points). . . . .	81
4.14	Phases of $S_{11}$ and $S_{21}$ of the band-pass filter shown in Fig. 3.25 (exact:41 points, interpolated:15 points). . . . .	82
5.1	Flowchart of a typical genetic algorithm used in the optimization process. . . . .	86
5.2	Geometry of the the proximity coupled microstrip antenna with tuning stub. . . . .	88
5.3	$\Gamma_{in}$ of the the proximity coupled microstrip antenna shown in Fig. 5.2 before and after optimization. . . . .	90
5.4	Matrix solve times during the optimization process on a SUN SPARC 20 workstation for each analysis. . . . .	91
5.5	Matrix fill times during the optimization process on a SUN SPARC 20 workstation for each analysis. . . . .	91
E.1	Relative errors for the integral given in Eq. (E.39) . . . . .	124
E.2	Relative errors for the integral given in Eq. (E.39) . . . . .	124
E.3	Relative errors for the integral given in Eq. (E.35) . . . . .	125
E.4	CPU times for different number of evaluation points for the integral given in Eq. (E.35) . . . . .	126
E.5	Relative errors for the summation given in Eq. (E.40) . . . . .	127
E.6	Relative errors for the summation given in Eq. (E.42) . . . . .	128
E.7	Relative errors for the summation given in Eq. (E.42) . . . . .	128
E.8	CPU times for different acceleration methods applied to Eq. (E.19)	129
E.9	Relative errors for the summation given in Eq. (E.43) . . . . .	130

# List of Tables

3.1	Equivalent lumped circuit values for the microstrip corner shown in Fig. 3.10. . . . .	42
3.2	Equivalent lumped circuit values for the proximity coupled patch antenna shown in Fig. 3.14. . . . .	45
3.3	Equivalent lumped circuit values for the interdigital capacitor shown in Fig. 3.28. . . . .	56
4.1	CPU times in terms of seconds consumed in the analysis of some typical geometries on a SUN SPARC 20 workstation. . . . .	67
4.2	CPU times in terms of seconds consumed in the analysis of some typical geometries with adaptive $s$ parameter selection on a SUN SPARC 20 workstation. . . . .	77
5.1	Parameters of the genetic algorithm used in the optimization.	89
E.1	Summary of the transformations used in the examples . . . . .	123

# Chapter 1

## Introduction

The history of microwave printed circuits begins with the invention of flat-strip coaxial transmission lines by V. H. Rumsey and H. W. Jamieson to use in an antenna system and power division network during World War II [1]. Later, Hewlett Packard Co. developed the “slotted line” which was a commercial application of a planar coaxial system. Then, it was shown by Robert M. Barrett that the planar circuits could be also used to build passive microwave components like filters, directional couplers, and hybrids [1]. After the realization of the potential of the printed circuits, R&D facilities have been concentrated in this field to explore the possible application areas. Some of the research centers worked on this field were Tufts University, the Airborne Instruments Laboratory (Strip Line), the Polytechnic Institute of Brooklyn, Sanders Associates (Tri-Plate). and Federal Communications Research Laboratories (Micro-Strip) [1]. Because the printed circuits are rugged, easy to produce and reproducible, and because they have low cross-section and weight which make them useful in airborne applications, they have quickly gained a lot of interest and have been used in many applications in places of their waveguide and coaxial line counterparts.

The advent of monolithic microwave integrated circuits (MMIC) has increased the importance of printed structures in planarly layered media. Thus, development of a rigorous and efficient technique to characterize such structures has become an important issue in computational electromagnetics. Once the

analysis is performed with the use of a rigorous full-wave method, the lumped circuit model of the passive structure can be extracted to use in a circuit simulation program with active devices. In addition, interactions between the passive circuits, like coupling between array elements in a microstrip antenna array, can also be investigated more rigorously.

## 1.1 A Brief Review of the Analysis Methods of Printed Structures

There have been a flurry of activities in the area of computational electromagnetics to develop computationally efficient and accurate numerical techniques for modeling and simulating the electrical performances of printed circuits. Basically, there are two approaches in the characterization of such structures: approximate but numerically efficient methods, like quasi-static methods [2–4] and accurate but computationally expensive methods such as the method of moments (MoM) [5, 6], the finite element method (FEM) [7] and the finite-difference time domain (FDTD) method [8].

The FDTD method is formulated by discretizing the Maxwell's equations both in the space and time domains. One of the advantages of the FDTD method is that the frequency response of the circuit can be extracted through a band of frequency by applying a narrow Gaussian pulse excitation in the time domain. The FEM is a general numerical technique to find approximate solutions to the boundary value problems. In the FEM, the entire volume is divided into sub-volumes in which the unknown function is represented by simple interpolating functions. Then, a set of algebraic equations is obtained by applying the Rayleigh-Ritz procedure. Common advantages of the above mentioned methods are that they are quite general and versatile and that the resulting matrix equations are sparse yielding an efficient memory and CPU time requirements for solving this system of linear equations. However, both methods have difficulties when they are applied to open geometries, like radiating structures, because they require



discretization or segmentation of the whole volume of interest. In this case, artificial absorbing boundaries should be introduced to satisfy the radiating condition. On the other hand, the MoM is applied to an integral equation that accounts for the geometry, so the problem domain is reduced to regions where the surface or volume current densities can be defined. The advantage of this technique, as compared to the FEM and the FDTD, is the reduced number of unknowns and its suitability for planar geometries. However, the major disadvantage is that the MoM matrix entries are double or triple integrals of complex functions.

Since the MoM is used as the main numerical technique throughout this work, it would be instructive to give a brief introduction of the technique as applied to planar printed geometries in electromagnetics. The formulation of the MoM starts with writing an integral equation describing the problem, which could be electric field integral equation (EFIE), magnetic field integral equation (MFIE) or mixed potential integral equation (MPIE). The formulations of EFIE and MFIE involve the Green's functions of the electric and magnetic fields as their kernels, respectively, while the MPIE uses the Green's functions of the scalar and vector potentials. Since the Green's functions of the electric and magnetic fields are more singular than those of the scalar and vector potentials, the MPIE formulation has recently become more popular in the application of the MoM to the characterization of planar printed geometries [9–12]. Therefore, the MPIE formulation is employed in this work and its solution is obtained via the MoM. The MoM can be applied either in the spectral domain or in the spatial domain. The spectral domain version is applied to the spectral domain representation of the EFIE while the spatial domain version is applied to the MPIE. In this thesis, the spatial-domain MoM is employed because of the aforementioned advantage of the MPIE. Although the Green's functions used in the spectral-domain representation of the EFIE can be expressed in closed forms for planar printed geometries, the MoM matrix entries become double integrals of complex functions over infinite domain, which requires the use of computationally expensive numerical integration algorithms. On the other hand, the MoM matrix

entries for the spatial-domain MoM are double integrals over finite domains, but the integrands are in terms of the spatial-domain Green's functions of the potentials, which are expressed as the Hankel transforms of the corresponding spectral-domain Green's functions [13, 14]. Since the Hankel transforms of the spectral-domain Green's functions are oscillatory and slow convergent in nature, the use of the spatial-domain MoM was not popular until the recent introduction of an efficient algorithm to approximate the spatial-domain Green's functions in closed forms [15, 16]. This closed-form approximation of the spatial-domain Green's functions not only improves the calculation of the Green's functions, but also results in the MoM matrix entries that can be evaluated analytically [17]. Therefore, the computational efficiency of the spatial-domain MoM in the solution of the MPIE has been significantly improved without sacrificing the accuracy in the results.

In this thesis, the MPIE in the spatial-domain employing the closed-form Green's functions is used to find the current distribution on the conductors which are immersed in a planarly layered medium. The organization of this thesis is as follows: In Chapter 2, the spectral- and spatial-domain Green's functions for planarly stratified media are introduced. Then, in Chapter 3, a general MPIE formulation for planarly stratified media is presented using the closed-form spatial-domain Green's functions, and some numerical examples are given. Chapter 4 discusses some approaches that are used to improve the total solution time of the circuits. Then in Chapter 5, a brief introduction is provided for the optimization of printed circuits with genetic algorithms. Finally the conclusions are given in Chapter 6.

## Chapter 2

# Green's Functions in Planarly Layered Media

For a planarly layered medium, the spatial-domain Green's functions are obtained from the spectral-domain Green's functions via the Hankel transformation, in which the spectral-domain Green's functions are known in closed forms for layered media [18, 19]. This transformation, also known as Sommerfeld integral, contains oscillatory integrand over an infinite domain whose evaluation is computationally very expensive [20], hence the apparent disadvantage of the spatial-domain MoM formulation.

Recently it was demonstrated that the computational burden in the calculation of the spatial-domain Green's functions can be circumvented by approximating the spectral-domain Green's functions in terms of complex exponentials, whose Hankel transforms can be analytically obtained via the Sommerfeld identity [15]. Hence, the spatial-domain Green's functions for the vector and scalar potentials can be cast into so-called closed forms, which are finite sums of complex images. In this approach the crucial step is the numerical implementation of the exponential approximation, which can be performed by using Prony's techniques [21] or techniques based on the pencil of functions [22, 23]. The original derivation of the closed-form Green's functions, as proposed by Chow et. al. [15], employed the original Prony method and was limited in

use to thick and single layer structures, which was due to inadequacy of the original Prony method. This problem was eliminated by employing the least squares Prony method [24], and then the approximation was further improved by using the generalized pencil of functions method (GPOF) [19], which is less noise sensitive and more robust as compared to the Prony methods (see Appendix C). However, the algorithm for the exponential approximation was still computationally expensive, because Prony's methods and the GPOF method require uniform sampling of the function to be approximated along the range of approximation. This, in turn, makes it necessary to take a large number of samples for functions with local oscillations and fast variations, like spectral-domain Green's functions in general, rendering the algorithm computationally expensive and not robust. Recently, a two-level approach that requires piecewise uniform sampling has been introduced to eliminate this problem, and is demonstrated to be much more efficient and robust [25]. Hence, the spatial-domain closed-form Green's functions can be employed efficiently in the solution of MPIE for planar, multilayer geometries. There are also other approaches where an asymptotic closed-form Green's functions are obtained [26,27], however it should be noted that the closed-form Green's functions derived by the method given in this thesis are valid in all spatial regions.

In Section 2.1, the spectral-domain Green's functions for planarly stratified media are given. Then, Section 2.2 describes the method of obtaining the closed-form spatial-domain Green's functions. And finally, conclusions are given in Section 2.3.

## 2.1 Green's Functions in Spectral Domain

Consider a general source placed in a planarly stratified medium which is shown in Fig. 2.1. It is assumed that all layers extend to infinity in the horizontal plane, and, the thickness and the relative permittivity of  $i$ -th layer are denoted by  $d_i$  and  $\epsilon_{r,i}$ , respectively. Note that the origin of the coordinate axis is placed at the bottom of the source layer, and the time convention of  $e^{j\omega t}$  has been adopted

through the formulation.

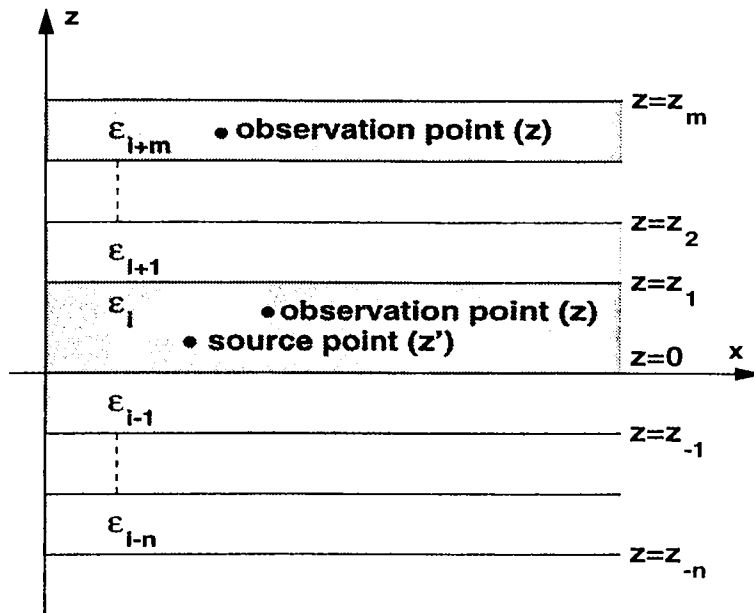


Figure 2.1: A general source placed in a planarly stratified medium.

In a planarly layered medium, the electrical properties of the structure change only in one direction, e.g., in the  $z$  direction. For that reason, the vector wave equations need not be solved in their full forms. In fact, in the source-free case, the vector wave equations can be reduced to two scalar equations representing  $TE$  and  $TM$  waves which are decoupled from each other [18].

In the MPIE formulation, the Green's functions of both vector and scalar potentials are used. It is known that for a horizontal dipole, two components of the vector potential are required to satisfy the boundary conditions [28, 29]. Traditionally, the  $z$ -component is selected in addition to the component which is in the same direction with the dipole. The Green's function, in this case, will have the following form:

$$\bar{\mathbf{G}}_{\mathbf{A}} = (\hat{x}\hat{x} + \hat{y}\hat{y})G_{xx} + \hat{x}\hat{x}G_{zx} + \hat{z}\hat{y}G_{zy} + \hat{z}\hat{z}G_{zz} \quad (2.1)$$

The scalar potential due to a single point charge associated with a time-harmonic



Hertzian dipole can be derived from the vector potential via [28]

$$\frac{j\omega}{k^2} \nabla \cdot \bar{\mathbf{G}}_{\mathbf{A}} = \frac{1}{j\omega} \nabla' G_q \quad (2.2)$$

However, since the scalar potential depends on the chosen form of the magnetic vector potential in a layered medium, it is not unique. That is, the scalar potential associated with a vertical dipole is different from the scalar potential of a horizontal dipole when the medium is stratified. Therefore, a single scalar potential  $G_q$  satisfying (2.2) does not, in general, exist if the traditional form of the vector Green's function  $\bar{\mathbf{G}}_{\mathbf{A}}$ , given in (2.1), is employed.

To find the spectral-domain Green's functions, the field components of a Hertzian dipole in the  $\hat{\alpha}$  direction, which is placed in a homogeneous medium, are written as

$$\mathbf{E}(\mathbf{r}) = -j\omega\mu \left( \bar{\mathbf{I}} + \frac{\nabla\nabla}{k^2} \right) \cdot \hat{\alpha} Il \frac{e^{-jkr}}{4\pi r} \quad (2.3)$$

$$\mathbf{H}(\mathbf{r}) = \nabla \times \hat{\alpha} Il \frac{e^{-jkr}}{4\pi r} \quad (2.4)$$

from which the *TM* and *TE* field components of the dipole can be derived easily. Since the dipole is in a layered medium, the spherical wave behavior in (2.3) and (2.4) must be modified. This is achieved by expanding the spherical wave terms in terms of plane waves using the Weyl identity

$$\frac{e^{-jkr}}{r} = -\frac{j}{2\pi} \int_{-\infty}^{\infty} \int_{-\infty}^{\infty} dk_x dk_y \frac{e^{-jk_x x - jk_y y - jk_z |z|}}{k_z} \quad (2.5)$$

where  $k_x^2 + k_y^2 + k_z^2 = k_0^2$ . Then reflections from the planar boundaries of the stratified medium, can be easily accounted for the field expressions. Note that since the medium is translationally invariant in the  $xy$  plane, the phase matching condition requires that  $k_x$  and  $k_y$  are the same in all layers.

The spectral-domain Green's functions are first derived in the source layer by considering the direct wave, and the reflected waves from the boundaries, as shown in the next sections. Then, the field in any other layer can be obtained from the field expression of the source layer.

### 2.1.1 Horizontal electric dipole (HED)

Derivation of the spectral-domain Green's functions for an HED starts with writing  $E_z$  ( $TM_z$ ) and  $H_z$  ( $TE_z$ ) components of the fields in the source layer. So,  $E_z$  and  $H_z$  are first written in a homogeneous medium as

$$E_z = -\frac{jIl}{4\pi\omega\varepsilon} \frac{\partial^2}{\partial z \partial x} \frac{e^{-jkr}}{r} \quad (2.6)$$

$$H_z = -\frac{Il}{4\pi} \frac{\partial}{\partial y} \frac{e^{-jkr}}{r} \quad (2.7)$$

Then, the spherical wave terms are expressed as an integral summation of the plane waves propagating in all directions using the Weyl identity

$$E_z = \frac{Il}{8\pi^2\omega\varepsilon_i} \int_{-\infty}^{\infty} \int_{-\infty}^{\infty} dk_x dk_y k_x e^{-jk_x x - jk_y y - jk_{z_i} |z|} \quad (2.8)$$

$$H_z = \frac{Il}{8\pi^2} \int_{-\infty}^{\infty} \int_{-\infty}^{\infty} dk_x dk_y k_y \frac{e^{-jk_x x - jk_y y - jk_{z_i} |z|}}{k_{z_i}} \quad (2.9)$$

Since these expressions are valid in a homogeneous medium, the fields in a layered medium are obtained by considering the reflected waves from the boundaries as follows:

$$E_z = \frac{Il}{8\pi^2\omega\varepsilon_i} \int_{-\infty}^{\infty} \int_{-\infty}^{\infty} dk_x dk_y k_x e^{-jk_x x - jk_y y} F_{TM} \quad (2.10)$$

$$H_z = \frac{Il}{8\pi^2} \int_{-\infty}^{\infty} \int_{-\infty}^{\infty} dk_x dk_y k_y \frac{e^{-jk_x x - jk_y y}}{k_{z_i}} F_{TE} \quad (2.11)$$

where

$$F_{TE} = \begin{cases} e^{-jk_{z_i}(z-z')} + A_h^e e^{jk_{z_i}(z-z')} + C_h^e e^{-jk_{z_i}(z-z')} & z > z' \\ e^{-jk_{z_i}(z'-z)} + A_h^e e^{jk_{z_i}(z-z')} + C_h^e e^{-jk_{z_i}(z-z')} & z < z' \end{cases} \quad (2.12a)$$

$$F_{TE} = \begin{cases} e^{-jk_{z_i}(z-z')} + A_h^e e^{jk_{z_i}(z-z')} + C_h^e e^{-jk_{z_i}(z-z')} & z > z' \\ e^{-jk_{z_i}(z'-z)} + A_h^e e^{jk_{z_i}(z-z')} + C_h^e e^{-jk_{z_i}(z-z')} & z < z' \end{cases} \quad (2.12b)$$

$$F_{TM} = \begin{cases} e^{-jk_{z_i}(z-z')} + B_h^e e^{jk_{z_i}(z-z')} + D_h^e e^{-jk_{z_i}(z-z')} & z > z' \\ -e^{-jk_{z_i}(z'-z)} + B_h^e e^{jk_{z_i}(z-z')} + D_h^e e^{-jk_{z_i}(z-z')} & z < z' \end{cases} \quad (2.13a)$$

$$F_{TM} = \begin{cases} e^{-jk_{z_i}(z-z')} + B_h^e e^{jk_{z_i}(z-z')} + D_h^e e^{-jk_{z_i}(z-z')} & z > z' \\ -e^{-jk_{z_i}(z'-z)} + B_h^e e^{jk_{z_i}(z-z')} + D_h^e e^{-jk_{z_i}(z-z')} & z < z' \end{cases} \quad (2.13b)$$

Note that the origin is at the bottom of the source layer in this derivation (see Fig. 2.1). The down-going wave in the source layer is the consequence of the

reflection of the up-going wave at  $z = d_i$ , similarly, the up-going wave is the consequence of the reflection of the down-going wave at  $z = 0$ . Hence,

$$B_h^e e^{jk_{z_i}(d_i-z')} = \tilde{R}_{TM}^{i,i+1} \left( e^{-jk_{z_i}(d_i-z')} + D_h^e e^{-jk_{z_i}(d_i-z')} \right) \quad (2.14)$$

$$D_h^e e^{jk_{z_i}z'} = \tilde{R}_{TM}^{i,i-1} \left( -e^{-jk_{z_i}z'} + B_h^e e^{-jk_{z_i}z'} \right) \quad (2.15)$$

where  $\tilde{R}_{TM}$  is the generalized reflection coefficient at the boundaries [18]. By solving (2.14) and (2.15) simultaneously, the unknown coefficients  $B_h^e$  and  $D_h^e$  are found as

$$B_h^e = \frac{\tilde{R}_{TM}^{i,i+1} e^{-j2k_{z_i}(d_i-z')} - \tilde{R}_{TM}^{i,i+1} \tilde{R}_{TM}^{i,i-1} e^{-j2k_{z_i}d_i}}{1 - \tilde{R}_{TM}^{i,i+1} \tilde{R}_{TM}^{i,i-1} e^{-j2k_{z_i}d_i}} \quad (2.16)$$

$$D_h^e = \frac{-\tilde{R}_{TM}^{i,i-1} e^{-j2k_{z_i}z'} + \tilde{R}_{TM}^{i,i-1} \tilde{R}_{TM}^{i,i+1} e^{-j2k_{z_i}d_i}}{1 - \tilde{R}_{TM}^{i,i+1} \tilde{R}_{TM}^{i,i-1} e^{-j2k_{z_i}d_i}} \quad (2.17)$$

Since the same approach is used to find the other coefficients,  $A_h^e$  and  $C_h^e$ , their derivations are not given here for the sake of brevity. To derive the vector Green's functions, one can proceed as follows:

$$\begin{aligned} A_x &= -\mu_i \int H_z dy \\ &= \frac{Il}{j8\pi^2} \int_{-\infty}^{\infty} \int_{-\infty}^{\infty} dk_x dk_y \frac{e^{-jk_x x - jk_y y}}{k_{z_i}} F_{TE} \end{aligned} \quad (2.18)$$

$$\Rightarrow \tilde{G}_{xx}^A = \frac{\mu_i}{j2k_{z_i}} \left\{ e^{-jk_{z_i}|z-z'|} + A_h^e e^{jk_{z_i}(z-z')} + C_h^e e^{-jk_{z_i}(z-z')} \right\} \quad (2.19)$$

$$A_z = \mu_i \int H_x dy = \mu_i \int \frac{1}{k_\rho^2} \left[ \frac{\partial^2}{\partial z \partial x} H_z + j\omega\epsilon \frac{\partial}{\partial y} E_z \right] dy \quad (2.20)$$

$$= \frac{\mu_i Il}{8\pi^2} \int_{-\infty}^{\infty} \int_{-\infty}^{\infty} dk_x dk_y e^{-jk_x x - jk_y y} \left\{ \frac{k_x}{k_{z_i} k_\rho^2} \frac{\partial}{\partial z} F_{TE} + \frac{jk_x}{k_\rho^2} F_{TM} \right\}$$

$$\Rightarrow \tilde{G}_{zx}^A = -\frac{\mu_i k_x}{2jk_\rho^2} \left\{ (A_h^e + B_h^e) e^{jk_{z_i}(z-z')} + (D_h^e - C_h^e) e^{-jk_{z_i}(z-z')} \right\} \quad (2.21)$$

and for the scalar Green's function,

$$\phi_d = -\frac{\nabla \cdot \mathbf{A}}{j\omega\mu_i\epsilon_i} = -\frac{1}{j\omega\mu_i\epsilon_i} \left( \frac{\partial A_x}{\partial x} + \frac{\partial A_z}{\partial z} \right) \quad (2.22)$$

$$\phi_d = \frac{\partial}{\partial x'} \phi_q \quad (2.23)$$

$$\Rightarrow \check{G}_x^q = \frac{-j}{2\epsilon_i k_\rho^2} \left\{ \frac{k_\rho^2}{k_{z_i}} e^{-jk_{z_i}|z-z'|} + \frac{k_i^2 A_h^e + k_{z_i}^2 B_h^e}{k_{z_i}} e^{jk_{z_i}(z-z')} \right. \\ \left. + \frac{k_i^2 C_h^e - k_{z_i}^2 D_h^e}{k_{z_i}} e^{-jk_{z_i}(z-z')} \right\} \quad (2.24)$$

### 2.1.2 Vertical electric dipole (VED)

The derivation of the spectral-domain Green's functions for a VED is similar to the approach used for HED, therefore it will be briefly given here. As a first step,  $E_z$  and  $H_z$  components of the fields due to a VED are written as follows:

$$E_z = -\frac{jI\omega\mu}{4\pi k^2} \left( k^2 + \frac{\partial^2}{\partial z^2} \right) \frac{e^{-jk_r}}{r} \quad (2.25)$$

$$H_z = 0 \quad (2.26)$$

Then, by using the Weyl identity, (2.25) is expanded as

$$E_z = -\frac{I\omega\mu}{8\pi^2 k^2} \int_{-\infty}^{\infty} \int_{-\infty}^{\infty} dk_x dk_y \left( \frac{k^2}{k_{z_i}} - k_{z_i} \right) e^{-jk_x x - jk_y y - jk_{z_i}|z|} \quad (2.27)$$

Next, the field expression in a layered medium is obtained by considering the reflected waves as

$$E_z = \frac{Il}{8\pi^2 \omega \epsilon_i} \int_{-\infty}^{\infty} \int_{-\infty}^{\infty} dk_x dk_y k_x e^{-jk_x x - jk_y y} F_{TM} \quad (2.28)$$

where

$$F_{TM} = \begin{cases} e^{-jk_{z_i}(z-z')} + A_y^e e^{-jk_{z_i}(z-z')} + B_y^e e^{jk_{z_i}(z-z')} & z > z' \\ e^{-jk_{z_i}(z'-z)} + A_y^e e^{-jk_{z_i}(z-z')} + B_y^e e^{jk_{z_i}(z-z')} & z < z' \end{cases} \quad (2.29a)$$

$$(2.29b)$$

Using the boundary conditions at the interface of the layers, the unknown coefficients  $A_y^e$  and  $B_y^e$  obtained as before. To derive the vector Green's function, one can proceed as follows:

$$A_z = \mu_i \int H_x dy = \mu_i \int \frac{1}{k_\rho^2} \left[ j\omega\epsilon \frac{\partial}{\partial y} E_z \right] dy \quad (2.30)$$

$$\begin{aligned}
 &= j \frac{\mu_i l l}{8\pi^2} \int_{-\infty}^{\infty} \int_{-\infty}^{\infty} dk_x dk_y e^{-jk_x x - jk_y y} \left( \frac{k^2}{k_{z_i} k_\rho^2} - \frac{k_{z_i}}{k_\rho^2} \right) F_{TM} \\
 \Rightarrow \check{G}_{zz}^A &= \frac{\mu_i}{2j k_{z_i}} \left\{ e^{-jk_{z_i}|z-z'|} + A_v^e e^{-jk_{z_i}(z-z')} + B_v^e e^{jk_{z_i}(z-z')} \right\} \quad (2.31)
 \end{aligned}$$

and for the scalar Green's function,

$$\phi_d = -\frac{\nabla \cdot \mathbf{A}}{j\omega\mu_i\epsilon_i} = -\frac{1}{j\omega\mu_i\epsilon_i} \frac{\partial A_z}{\partial z} \quad (2.32)$$

$$\phi_d = \frac{\partial}{\partial z'} \phi_q \quad (2.33)$$

$$\Rightarrow \check{G}_z^q = \frac{1}{2j\epsilon_i k_{z_i}} \left\{ e^{-jk_{z_i}|z-z'|} + C_v^e e^{-jk_{z_i}(z-z')} + D_v^e e^{jk_{z_i}(z-z')} \right\} \quad (2.34)$$

where the unknown coefficients are obtained from the boundary conditions as before.

### 2.1.3 Green's functions for electric and magnetic dipoles

In summary, the spectral-domain Green's functions in the source layer for different kind of sources and orientations, are obtained by using the described method as follows [19]:

$$\check{G}_{xx}^A = \frac{\mu_i}{2j k_{z_i}} \left[ e^{-jk_{z_i}|z-z'|} + A_h^e e^{jk_{z_i}(z-z')} + C_h^e e^{-jk_{z_i}(z-z')} \right] \quad (2.35)$$

$$\check{G}_{zx}^A = \frac{-\mu_i}{2j k_{z_i}} \left[ \frac{k_x k_{z_i}}{k_\rho^2} (A_h^e + B_h^e) e^{jk_{z_i}(z-z')} + \frac{k_x k_{z_i}}{k_\rho^2} (D_h^e - C_h^e) e^{-jk_{z_i}(z-z')} \right] \quad (2.36)$$

$$\begin{aligned}
 \check{G}_x^{q_e} &= \frac{1}{2j\epsilon_i k_{z_i}} \left[ e^{-jk_{z_i}|z-z'|} + \frac{k_{z_i}^2 B_h^e + k_i^2 A_h^e}{k_\rho^2} e^{jk_{z_i}(z-z')} \right. \\
 &\quad \left. + \frac{k_i^2 C_h^e - k_{z_i}^2 D_h^e}{k_\rho^2} e^{-jk_{z_i}(z-z')} \right] \quad (2.37)
 \end{aligned}$$

$$\check{G}_{xx}^F = \frac{\epsilon_i}{2j k_{z_i}} \left[ e^{-jk_{z_i}|z-z'|} + A_h^m e^{jk_{z_i}(z-z')} + C_h^m e^{-jk_{z_i}(z-z')} \right] \quad (2.38)$$

$$\check{G}_{zx}^F = \frac{-\epsilon_i}{2j k_{z_i}} \left[ \frac{k_x k_{z_i}}{k_\rho^2} (A_h^m + B_h^m) e^{jk_{z_i}(z-z')} + \frac{k_x k_{z_i}}{k_\rho^2} (D_h^m - C_h^m) e^{-jk_{z_i}(z-z')} \right] \quad (2.39)$$

$$\begin{aligned}
 \check{G}_x^{q_m} &= \frac{1}{2j\mu_i k_{z_i}} \left[ e^{-jk_{z_i}|z-z'|} + \frac{k_{z_i}^2 B_h^m + k_i^2 A_h^m}{k_\rho^2} e^{jk_{z_i}(z-z')} \right. \\
 &\quad \left. + \frac{k_i^2 C_h^m - k_{z_i}^2 D_h^m}{k_\rho^2} e^{-jk_{z_i}(z-z')} \right] \quad (2.40)
 \end{aligned}$$

$$\check{G}_{zz}^A = \frac{\mu_i}{2jk_{z_i}} \left[ e^{-jk_{z_i}|z-z'|} + A_v^e e^{-jk_{z_i}(z-z')} + B_v^e e^{jk_{z_i}(z-z')} \right] \quad (2.41)$$

$$\check{G}_z^{q_e} = \frac{1}{2j\epsilon_i k_{z_i}} \left[ e^{-jk_{z_i}|z-z'|} + C_v^e e^{-jk_{z_i}(z-z')} + D_v^e e^{jk_{z_i}(z-z')} \right] \quad (2.42)$$

$$\check{G}_{zz}^F = \frac{\epsilon_i}{2jk_{z_i}} \left[ e^{-jk_{z_i}|z-z'|} + A_v^m e^{-jk_{z_i}(z-z')} + B_v^m e^{jk_{z_i}(z-z')} \right] \quad (2.43)$$

$$\check{G}_z^{q_m} = \frac{1}{2j\mu_i k_{z_i}} \left[ e^{-jk_{z_i}|z-z'|} + C_v^m e^{-jk_{z_i}(z-z')} + D_v^m e^{jk_{z_i}(z-z')} \right] \quad (2.44)$$

where the superscript  $A$  and  $F$  denote the electric and magnetic vector potentials, respectively,  $q_e$  and  $q_m$  denote the electric and magnetic scalar potentials, respectively. The coefficients,  $A_{h,v}^{e,m}$ ,  $B_{h,v}^{e,m}$ ,  $C_{h,v}^{e,m}$ , and  $D_{h,v}^{e,m}$  are the functions of the generalized reflection coefficients and are given [18,19] as

$$A_h^{e,m} = \check{R}_{TE,TE}^{i,i+1} M_i^{TE,TE} \left[ e^{-2jk_{z_i}(d_i-z')} + \check{R}_{TE,TE}^{i,i-1} e^{-2jk_{z_i}d_i} \right] \quad (2.45)$$

$$B_h^{e,m} = \check{R}_{TM,TE}^{i,i+1} M_i^{TM,TE} \left[ e^{-2jk_{z_i}(d_i-z')} - \check{R}_{TM,TE}^{i,i-1} e^{-2jk_{z_i}d_i} \right] \quad (2.46)$$

$$C_h^{e,m} = \check{R}_{TE,TE}^{i,i-1} M_i^{TE,TE} \left[ e^{-2jk_{z_i}z'} + \check{R}_{TE,TE}^{i,i+1} e^{-2jk_{z_i}d_i} \right] \quad (2.47)$$

$$D_h^{e,m} = \check{R}_{TM,TE}^{i,i-1} M_i^{TM,TE} \left[ -e^{-2jk_{z_i}z'} + \check{R}_{TM,TE}^{i,i+1} e^{-2jk_{z_i}d_i} \right] \quad (2.48)$$

$$A_v^{e,m} = \check{R}_{TM,TE}^{i,i-1} M_i^{TM,TE} \left[ e^{-2jk_{z_i}z'} + \check{R}_{TM,TE}^{i,i+1} e^{-2jk_{z_i}d_i} \right] \quad (2.49)$$

$$B_v^{e,m} = \check{R}_{TM,TE}^{i,i+1} M_i^{TM,TE} \left[ e^{-2jk_{z_i}(d_i-z')} + \check{R}_{TM,TE}^{i,i-1} e^{-2jk_{z_i}d_i} \right] \quad (2.50)$$

$$C_v^{e,m} = \check{R}_{TM,TE}^{i,i-1} M_i^{TM,TE} \left[ -e^{-2jk_{z_i}z'} + \check{R}_{TM,TE}^{i,i+1} e^{-2jk_{z_i}d_i} \right] \quad (2.51)$$

$$D_v^{e,m} = \check{R}_{TM,TE}^{i,i+1} M_i^{TM,TE} \left[ -e^{-2jk_{z_i}(d_i-z')} + \check{R}_{TM,TE}^{i,i-1} e^{-2jk_{z_i}d_i} \right] \quad (2.52)$$

where

$$M_i^{TE,TE} = \left[ 1 - \check{R}_{TE,TE}^{i,i+1} \check{R}_{TE,TE}^{i,i-1} e^{-jk_{z_i}2d_i} \right]^{-1} \quad (2.53)$$

$$\check{R}_{TE,TE}^{j+1,j} = \frac{R_{TE,TE}^{j+1,j} + \check{R}_{TE,TE}^{j,j-1} e^{-jk_{z_j}2d_j}}{1 - R_{j,j+1} \check{R}_{TE,TE}^{j,j-1} e^{-jk_{z_j}2d_j}} \quad (2.54)$$

Here  $R$  and  $\check{R}$  are the Fresnel and generalized reflection coefficients [18] for which the subscripts  $TE$  and  $TM$  represent the polarization of the wave, and the superscripts show the layer numbers. The subscripts  $h$  and  $v$  represent the orientation of the source, horizontal and vertical, respectively, while the superscripts  $e$  and  $m$  denote the type of the source, electric and magnetic, respectively. It should be noted that the Green's functions for  $y$ -oriented dipoles

can be obtained simply by setting  $\tilde{G}_{yy}^{A,F} = \tilde{G}_{xx}^{A,F}$ ,  $\tilde{G}_{zy}^{A,F}/k_y = \tilde{G}_{zx}^{A,F}/k_x$ , and  $\tilde{G}_y^{qe,m} = \tilde{G}_x^{qe,m}$ .

When the observation layer is different from the source layer, the Green's functions are modified by using the appropriate boundary conditions and following iterative expressions [18]:

$$A_j^- = A_{j+1}^- \frac{T_{j+1,j} e^{-j(k_{z_{j+1}} - k_{z_j})(z' + z_{i-j+1})}}{1 - R_{j,j+1} \tilde{R}_{j,j-1} e^{-jk_{z_j} 2d_j}} \quad (2.55)$$

$$A_j^+ = A_{j-1}^+ \frac{T_{j-1,j} e^{-j(k_{z_{j-1}} - k_{z_j})(z_{i-j-1} + d_i - z')}}{1 - R_{j,j-1} \tilde{R}_{j,j+1} e^{-jk_{z_j} 2d_j}} \quad (2.56)$$

where  $A_j^-$  and  $A_j^+$  are the amplitudes of the down- and up-going waves, respectively, and  $T$  is the transmission coefficient. So, the field expressions in any layer can be obtained iteratively starting from the source layer.

## 2.2 Closed-form Green's Functions in Spatial Domain

The spatial-domain Green's functions are obtained from the spectral-domain counterparts through an integral transformation, called the Hankel transform or the Sommerfeld integral in electromagnetics [13]. This transformation is given as

$$G = \frac{1}{4\pi} \int_{SIP} dk_\rho k_\rho H_0^{(2)}(k_\rho \rho) \tilde{G}(k_\rho) \quad (2.57)$$

where  $G$  and  $\tilde{G}$  are the Green's functions in the spatial and spectral domains, respectively,  $H_0^{(2)}$  is the Hankel function of the second kind and  $SIP$  is the Sommerfeld integration path. The spectral-domain Green's function, which is the integrand of the Sommerfeld integral given in Eq. (2.57), contains branch-point and pole singularities. The branch-point singularities correspond to radiating modes in the outermost layers, whereas, the pole singularities correspond to guided modes in the dielectric layers.

In principle, there are two ways for evaluating the Sommerfeld integral when the exact analytical integration is not possible: *i.*) Asymptotic methods like

the method of stationary phase and the method of steepest descent [18], and *ii.*) numerical integration methods [14]. Although the asymptotic methods give better physical understanding of the integral itself, they must be re-formulated for different geometries, hence they are not suitable to use in a CAD software. On the other hand, the numerical integration of the Sommerfeld integral is computationally expensive procedure because the integrand is an oscillatory complex function with the singularities mentioned above, and because the limits of integration extent to infinity. As a conclusion, the evaluation of the Sommerfeld integral with the aforementioned methods is not suitable for a CAD algorithm [20, 25].

To eliminate the numerical integration of the Sommerfeld integral, the spectral-domain Green's functions are approximated by complex exponentials, whose Hankel transforms can be evaluated analytically, thus the spatial-domain Green's functions can be written in closed-forms [15, 25]. This procedure was first proposed by Chow et.al. [15] for a horizontal electric dipole over a thick substrate and extended to a geometry with a substrate and superstrate with arbitrary thickness by Aksun and Mittra [24].

The original approach of getting the closed-form Green's functions in the spatial domain requires some trial-and-error iterations for deciding the approximation parameters, like the number of exponentials, the number of sampling points and the maximum range of the approximation. Moreover, the quasi-dynamic images and the surface wave poles need to be found and extracted from the Green's function prior to the approximation in order to ease the difficulties in the algorithm. However, with the introduction of the two-level approach, which is robust and very efficient, these difficulties are eliminated, and hence the method becomes very suitable for CAD implementation [25]. It should be noted that the sampling of the spectral-domain Green's functions should be performed along the SIP or along a path legitimately deformed from the SIP, details of which can be found in [15, 25]. In this thesis, we have employed a deformed path from the SIP as depicted in Fig. 2.2, consisting of three connected paths denoted as  $C_{ap1}$ ,  $C_{ap2}$  and  $C_{ap3}$ , respectively, and described by the following



parametric equations:

$$\text{For } C_{ap3}: k_{z_i} = -jk_i [T_{o1} + T_{o2} + t] \quad 0 \leq t \leq T_{o3} \quad (2.58)$$

$$\text{For } C_{ap2}: k_{z_i} = -jk_i [T_{o1} + t] \quad 0 \leq t \leq T_{o2} \quad (2.59)$$

$$\text{For } C_{ap1}: k_{z_i} = k_i \left[ -jt + \left( 1 - \frac{t}{T_{o1}} \right) \right] \quad 0 \leq t \leq T_{o1} \quad (2.60)$$

where  $t$  is the running variable sampled uniformly on the corresponding ranges,  $T_{o1}$ ,  $T_{o2}$ , and  $T_{o3}$ . This approach is named hereafter as three-level approach, which is an extension of the two-level approach introduced recently [25], so its details are not included in this thesis. Because the spectral-domain Green's functions might have fast variations locally, and because the GPOF method requires uniform sampling along the range of approximation, the use of multi-level approach prevents taking thousands of samples. However, it is not necessary to use the three-level approach for smooth functions, for which one may use the two-level or one-level approach, simply by setting  $T_{o3}$  to zero or  $T_{o2}$  and  $T_{o3}$  to zero, respectively.

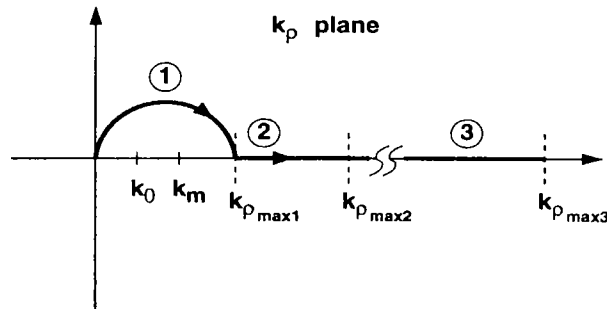


Figure 2.2: The path used in exponential approximation.

The exponential approximation process begins with sampling the function to be approximated, and then the algorithm for exponential approximation is employed for the sampled values of the function. In other words, one needs to know the values of the function at the points of samples, which requires fixing the parameters, like  $z$  and  $z'$  in Eqs. (2.35)-(2.44). After having sampled the spectral-domain Green's function to be approximated, apart from the term  $1/j2k_{z_i}$ , the

GPOF method is used to obtain the exponential approximation of the function, which results in an approximation as follows:

$$\tilde{G} \cong \frac{1}{j2k_z} \left\{ \sum_{n=1}^{N_1} a_{1n} e^{-b_{1n}k_z} + \sum_{n=1}^{N_2} a_{2n} e^{-b_{2n}k_z} + \sum_{n=1}^{N_3} a_{3n} e^{-b_{3n}k_z} \right\} \quad (2.61)$$

Once the spectral-domain Green's functions are represented as the sum of complex exponentials, each exponential term in (2.61) can be transformed to the spatial domain via the Sommerfeld identity

$$\frac{e^{-jkr}}{r} = \frac{1}{2j} \int_{SIP} dk_\rho k_\rho H_0^{(2)}(k_\rho \rho) \frac{e^{-jk_z|z|}}{k_z} \quad (2.62)$$

yielding the following Green's function expression in the spatial domain

$$G \cong \sum_{n=1}^{N_1} a_{1n} \frac{e^{-jk_i r_{1n}}}{r_{1n}} + \sum_{n=1}^{N_2} a_{2n} \frac{e^{-jk_i r_{2n}}}{r_{2n}} + \sum_{n=1}^{N_3} a_{3n} \frac{e^{-jk_i r_{3n}}}{r_{3n}} \quad (2.63)$$

where  $r_{1n} = \sqrt{\rho^2 - b_{1n}^2}$ ,  $r_{2n} = \sqrt{\rho^2 - b_{2n}^2}$ ,  $r_{3n} = \sqrt{\rho^2 - b_{3n}^2}$ , and  $\rho = \sqrt{x^2 + y^2}$ , and,  $a_n$ 's and  $b_n$ 's are complex numbers in general.

The extraction of the surface wave poles and the quasi-dynamic images helps to the exponential approximation technique, as stated before, by rendering the Green's functions in the spectral domain well-behaved and rapidly converging functions. However, since the contribution of the surface wave poles is small for geometries on a thin substrate, and it is not possible to find the quasi-dynamic images for multilayer planar structures analytically except for some simple cases, the spatial-domain Green's functions are obtained for a multilayer medium without extracting the surface wave poles and quasi-dynamic images in order to obtain a general-purpose algorithm.

## 2.3 Conclusions

The use of the closed-form Green's functions has eliminated the numerical integration of the Sommerfeld integrals improving the computational efficiency of the spatial-domain MoM for planar geometries in multilayer media.

The original algorithm developed for obtaining the closed-form spatial-domain Green's functions has the disadvantage of choosing the proper approximation parameters for each different geometry. Moreover, the extraction of the surface wave poles and quasi-dynamic images may not be possible or efficient for multilayer geometries when the original version of the approach is employed. The new approach based on a three-level approximation is developed to overcome these difficulties and to make the use of the closed-form Green's functions attractive for those developing the EM software as well as for researchers in the field.

## Chapter 3

# Field Analysis in Planarly Layered Media

Formulation of the spatial-domain MoM for the analysis of printed geometries begins with writing the MPIE in terms of the Green's functions of vector and scalar potentials in a multilayer medium. Then, the integral equation is discretized by expanding the unknown current densities in terms of known basis functions and by applying the boundary conditions in integral sense, which is called as the testing procedure in the MoM. This formulation has the advantage of employing the MPIE, whose kernel shows a weak surface integrable singularity while the EFIE involves stronger singularity, but it requires the Green's functions in the spatial domain. The spatial-domain Green's functions are obtained in closed form by using the technique presented in Chapter 2. After solving the linear system obtained by the application of the MoM, the current distribution on the conductors is found. For more information about the MoM, one can refer to Appendix E.

In Section 3.1, a general formulation of the problem is given. Section 3.2 presents the de-embedding algorithm which is used in the S-parameter calculation of the printed circuits. Then, in Section 3.3, some numerical examples are given. Finally, the conclusions are presented in Section 3.4.

### 3.1 MPIE Formulation in Planarly Layered Media

Consider, for the sake of illustration, a general microstrip structure in a multilayer environment as shown in Fig. 3.1. It is assumed that all layers and the ground plane extend to infinity in the horizontal plane, and the conductors are lossless and infinitesimally thin. The thickness and the permittivity of  $i$ -th layer are denoted by  $d_i$  and  $\epsilon_{r_i}$ , respectively. Although the geometry depicted in Fig. 3.1

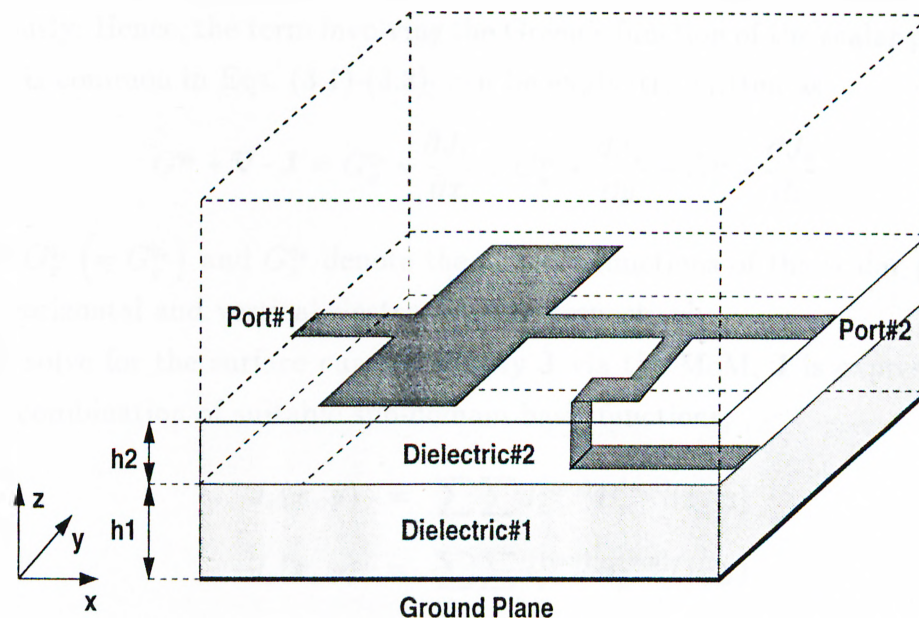


Figure 3.1: A typical multilayer printed geometry.

shows only one vertical metalization, the formulation given here can be applied to printed geometries which contain multiple vertical metalizations.

The tangential components of the electric field on the plane of the patch and on the vertical strips can be written in terms of the surface current density  $\mathbf{J}$ , and the associated Green's functions of the vector and scalar potentials as follows:

$$E_x = -j\omega G_{xx}^A * J_x + \frac{1}{j\omega} \frac{\partial}{\partial x} (G^{qe} * \nabla \cdot \mathbf{J}) \quad (3.1)$$

$$E_y = -j\omega G_{yy}^A * J_y + \frac{1}{j\omega} \frac{\partial}{\partial y} (G^{qe} * \nabla \cdot \mathbf{J}) \quad (3.2)$$

$$E_z = -j\omega G_{zx}^A * J_x - j\omega G_{zy}^A * J_y - j\omega G_{zz}^A * J_z + \frac{1}{j\omega} \frac{\partial}{\partial z} (G^{qe} * \nabla \cdot \mathbf{J}) \quad (3.3)$$

where  $*$  denotes convolution and  $G_{xx}^A = G_{yy}^A$ . The term  $G_{ij}^A$  represents the  $i$ -directed vector potential at  $\mathbf{r}$  due to a  $j$ -directed electric dipole of unit strength located at  $\mathbf{r}'$ , while  $G^{qe}$  represents the scalar potential by a unit point charge associated with an electric dipole. Since the traditional form of the Green's functions are employed in the formulation, the Green's function of the scalar potential is not unique for horizontal and vertical electric dipoles as stated previously. Hence, the term involving the Green's function of the scalar potential, which is common in Eqs. (3.1)-(3.3), can be explicitly written as

$$G^{qe} * \nabla \cdot \mathbf{J} = G_x^{qe} * \frac{\partial J_x}{\partial x} + G_y^{qe} * \frac{\partial J_y}{\partial y} + G_z^{qe} * \frac{\partial J_z}{\partial z} \quad (3.4)$$

where  $G_x^{qe}$  ( $= G_y^{qe}$ ) and  $G_z^{qe}$  denote the Green's functions of the scalar potential for a horizontal and vertical electric dipoles, respectively.

To solve for the surface current density  $\mathbf{J}$  via the MoM,  $\mathbf{J}$  is expressed as a linear combination of suitable sub-domain basis functions;

$$J_x(x, y) = \sum_m \sum_n I_x^{(mn)} B_x^{(mn)}(x, y) \quad (3.5)$$

$$J_y(x, y) = \sum_m \sum_n I_y^{(mn)} B_y^{(mn)}(x, y) \quad (3.6)$$

$$J_z(x, y, z) = \sum_l I_z^{(l)} B_z^{(l)}(x, y, z) \quad (3.7)$$

where  $B_x^{(mn)}$ ,  $B_y^{(mn)}$  and  $B_z^{(l)}$  are the basis functions with the unknown coefficients  $I_x^{(mn)}$ ,  $I_y^{(mn)}$  and  $I_z^{(l)}$ , defined at  $(mn)$ -th position on the subdivided horizontal conductor and at  $(l)$ -th position on the subdivided vertical conductor. In this thesis, rooftop functions are chosen as the basis functions to represent x-, y-, and z-components of the current density, as shown in Fig. 3.2. The sources are modeled as current filaments, therefore it is suitable to use half-rooftop basis functions at the source terminals, as well as at the sink terminals where the shorting pins or via holes are terminated in the ground plane. At the

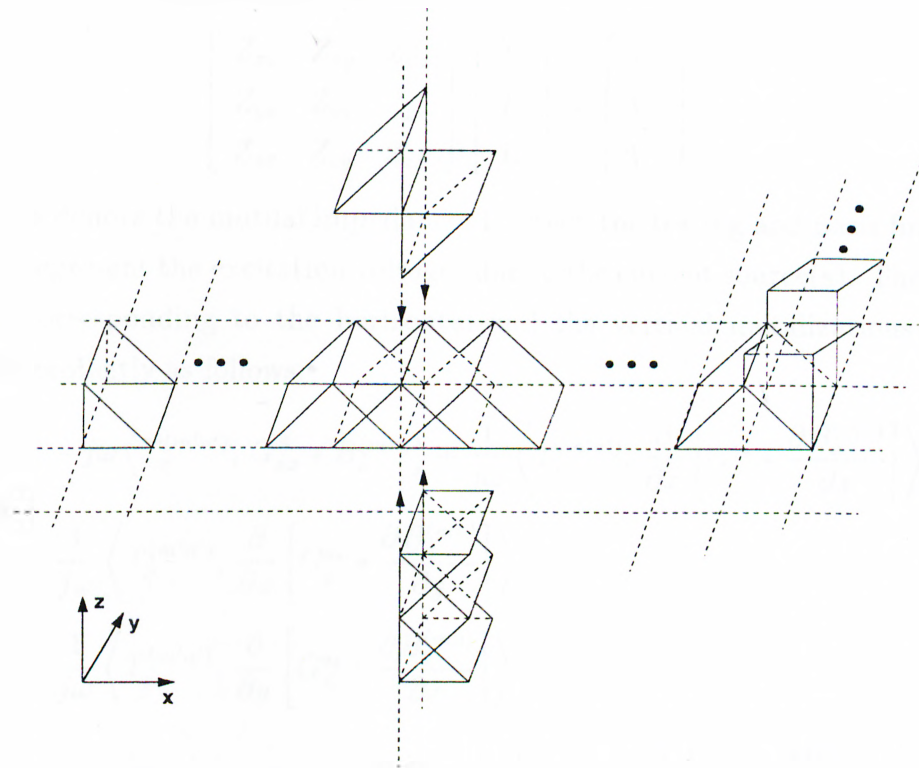


Figure 3.2: Basis functions used for horizontal and vertical connections in the MoM solution.

intersections of the vertical and horizontal conductors, half-rooftop and sawtooth basis functions are employed on the vertical and the horizontal conductors, respectively, whose amplitudes are related to satisfy the conservation of charges, Fig. 3.2.

Following the substitution of Eqs. (3.5)-(3.7) into Eqs. (3.1)-(3.3), the boundary conditions for the tangential electric fields are implemented in integral sense through the testing procedure of the MoM, for which the field expressions multiplied by some testing functions  $T_x^{(m'n')}$ ,  $T_y^{(m'n')}$  and  $T_z^{(l')}$  are integrated on the conductors and are set to zero. This leads to a matrix equation for the unknown

coefficients of the basis functions as

$$\begin{bmatrix} Z_{xx} & Z_{xy} & Z_{xz} \\ Z_{yx} & Z_{yy} & Z_{yz} \\ Z_{zx} & Z_{zy} & Z_{zz} \end{bmatrix} \begin{bmatrix} I_x \\ I_y \\ I_z \end{bmatrix} = \begin{bmatrix} V_x \\ V_y \\ V_z \end{bmatrix} \quad (3.8)$$

where  $Z$ s denote the mutual impedances between the testing and basis functions, and  $V$ s represent the excitation voltages due to the current source(s). The matrix entries corresponding to the horizontal and the vertical metalizations can be written explicitly as follows:

$$Z_{xx} = -j\omega \langle T_x^{(m'n')}, G_{xx}^A * B_x^{(mn)} \rangle + \frac{1}{j\omega} \left\langle T_x^{(m'n')}, \frac{\partial}{\partial x} \left[ G_x^{qe} * \frac{\partial B_x^{(mn)}}{\partial x} \right] \right\rangle \quad (3.9)$$

$$Z_{xy} = \frac{1}{j\omega} \left\langle T_x^{(m'n')}, \frac{\partial}{\partial x} \left[ G_y^{qe} * \frac{\partial B_y^{(mn)}}{\partial y} \right] \right\rangle \quad (3.10)$$

$$Z_{yx} = \frac{1}{j\omega} \left\langle T_y^{(m'n')}, \frac{\partial}{\partial y} \left[ G_x^{qe} * \frac{\partial B_x^{(mn)}}{\partial x} \right] \right\rangle \quad (3.11)$$

$$Z_{yy} = -j\omega \langle T_y^{(m'n')}, G_{yy}^A * B_y^{(mn)} \rangle + \frac{1}{j\omega} \left\langle T_y^{(m'n')}, \frac{\partial}{\partial y} \left[ G_y^{qe} * \frac{\partial B_y^{(mn)}}{\partial y} \right] \right\rangle \quad (3.12)$$

$$Z_{zx} = -j\omega \langle T_z^{(l')}, G_{zx}^A * B_x^{(mn)} \rangle + \frac{1}{j\omega} \left\langle T_z^{(l')}, \frac{\partial}{\partial z} \left[ G_x^{qe} * \frac{\partial B_x^{(mn)}}{\partial x} \right] \right\rangle \quad (3.13)$$

$$Z_{xz} = \frac{1}{j\omega} \left\langle T_x^{(m'n')}, \frac{\partial}{\partial x} \left[ G_z^{qe} * \frac{\partial B_z^{(l)}}{\partial z} \right] \right\rangle \quad (3.14)$$

$$Z_{zy} = -j\omega \langle T_z^{(l')}, G_{zy}^A * B_y^{(mn)} \rangle + \frac{1}{j\omega} \left\langle T_z^{(l')}, \frac{\partial}{\partial z} \left[ G_y^{qe} * \frac{\partial B_y^{(mn)}}{\partial y} \right] \right\rangle \quad (3.15)$$

$$Z_{yz} = \frac{1}{j\omega} \left\langle T_y^{(m'n')}, \frac{\partial}{\partial y} \left[ G_z^{qe} * \frac{\partial B_z^{(l)}}{\partial z} \right] \right\rangle \quad (3.16)$$

$$Z_{zz} = -j\omega \langle T_z^{(l')}, G_{zz}^A * B_z^{(l)} \rangle + \frac{1}{j\omega} \left\langle T_z^{(l')}, \frac{\partial}{\partial z} \left[ G_z^{qe} * \frac{\partial B_z^{(l)}}{\partial z} \right] \right\rangle \quad (3.17)$$

where  $\langle, \rangle$  and  $*$  denote inner product and convolution operators, respectively, and they are defined as follows:

$$\langle f(x, y), g(x, y) \rangle = \iint dx dy f(x, y) \cdot g(x, y) \quad (3.18)$$



$$f(x, y) * g(x, y) = \iint dx' dy' f(x - x', y - y') \cdot g(x', y') \quad (3.19)$$

The entries of the array  $V$  have the same form except the basis function, which is a half-rooftop function with unit amplitude to model the current source, therefore they are not given here. After evaluation of the inner product terms and substituting into Eq. (3.8), the current densities on the conductors are obtained by solving the matrix equation. Then, the scattering parameters are extracted from the current distribution.

The use of the closed-form Green's functions in conjunction with the MoM has been demonstrated to improve the computational efficiency of the MoM when applied to simple geometries like those consisting of only horizontal conductors. After having improved the computational efficiency and robustness of the derivation of the closed-form Green's functions, the natural step towards the goal of developing an accurate and efficient EM simulator is to study this approach for general geometries. A preliminary study shows that the application of the MoM in conjunction with the closed-form Green's functions to a geometry with vertical metalization is not as straightforward as its applications to only horizontal geometries, i.e., there are some difficulties in cases of vertical metalizations [30].

### 3.1.1 Difficulties and Solutions

The difficulties originate from the way the closed-form Green's functions are derived, more specifically, from the exponential approximation of the spectral-domain Green's functions. In Chapter 2, the representative form of the spectral-domain Green's functions is given and it is stated that the parameters,  $z$  and  $z'$ , have to be fixed in order to be able to sample the function over the range of approximation. In other words, the exponential approximation is valid for only those fixed values of the parameters, so are the closed-form Green's functions. For horizontal conductors, fixing  $z$  and  $z'$  does not pose a problem because the conductors are situated on constant  $z$ -planes requiring the Green's functions to be evaluated at these planes only. Therefore, one can fix these parameters prior

to the derivation of the closed-form Green's functions, and use these Green's functions for those values of the parameters only. However, the evaluations of the MoM matrix entries corresponding to the vertical metalizations require the convolution integrals and the inner-product integrals given in Eqs. (3.13)-(3.17), which are to be integrated over  $z$  and/or  $z'$ . So, the closed-form Green's functions, derived as described in Chapter 2, can not be used efficiently in the evaluation of such matrix entries.

This difficulty can be eliminated by recognizing that the amplitudes of the up- and down-going waves in the spectral-domain Green's functions are the exponential functions of  $z'$  that can be factored out (see Appendix A). As an example, the spectral-domain Green's function for the scalar potential due to a VED can be written as

$$\begin{aligned} \tilde{G}_z^{\eta} = & \frac{1}{2jk_{z_i}\epsilon_i} \left\{ e^{-jk_{z_i}|z-z'|} + \tilde{R}_{TM}^{i,i-1} M_i^{TM} \left[ -e^{-jk_{z_i}(z+z')} + \tilde{R}_{TM}^{i,i+1} e^{-jk_{z_i}(z-z'+2d_i)} \right] \right. \\ & \left. + \tilde{R}_{TM}^{i,i+1} M_i^{TM} \left[ -e^{-jk_{z_i}(2d_i-z-z')} + \tilde{R}_{TM}^{i,i-1} e^{-jk_{z_i}(z'-z+2d_i)} \right] \right\} \end{aligned} \quad (3.20)$$

after having substituted the amplitudes of the up- and down-going waves. Note that  $\tilde{R}_{TM}$  and  $M_i^{TM}$  are not functions of  $z$  and  $z'$ , and their explicit expressions are given in Chapter 2. A brief study of Eq. (3.20) shows that there are two approaches to overcome the difficulty: *i.*) application of the exponential approximation to each amplitude term, and *ii.*) performing the integration over  $z$  and  $z'$  analytically in the spectral domain, then applying the exponential approximation process. In the first approach, one needs to deal with each term in Eq. (3.20) separately; the first one is the direct term with unity amplitude, so no need for approximation, and the rest have amplitudes as functions of  $k_\rho$ . In other words, the approximation of  $\tilde{G}_z^{\eta}$  in terms of complex exponentials with the exponents including  $z$  and  $z'$  explicitly requires to approximate only the amplitude functions of the four exponentials in Eq. (3.20), namely  $\tilde{R}_{TM}^{i,i-1} M_i^{TM}$ ,  $\tilde{R}_{TM}^{i,i-1} M_i^{TM} \tilde{R}_{TM}^{i,i+1}$  and  $\tilde{R}_{TM}^{i,i+1} M_i^{TM}$ . The cost of having  $z$  and  $z'$  explicitly in the approximation of a Green's function is to apply the GPOF method three times more and is to use exponentials four times more as compared to approximating the same Green's function as a whole. The second solution is based on the fact

that  $z$  and  $z'$  dependence of the spectral-domain Green's functions is always in exponential form and analytically integrable over  $z$  and  $z'$  for most basis functions. Therefore, the integration over  $z$  and  $z'$ , which are due to the testing and convolution integrals along a vertical metalization, respectively, can be evaluated analytically if the spatial-domain Green's functions in the inner-product expressions are written as the inverse transforms of their spectral-domain representations. Then, the exponential approximation procedure is implemented on the resulting spectral-domain function. This approach eliminates the application of the exponential approximation for each term in the spectral-domain Green's function. However, it requires the application of the exponential approximation as many times as the number of testing functions, or number of basis functions, or number of basis times testing functions on the vertical metalization for the inner-product terms involving  $z$ , or  $z'$ , or  $z$  and  $z'$  integrations, respectively. Although the second approach seems to employ the exponential approximation algorithm more than the first one, it is more efficient for short vertical metalizations for which only a few basis functions are used. For one basis function on the vertical metalization which is usually sufficient for a practical geometry, the number of exponential approximation in the second approach is less than that in the first approach, and moreover it requires less number of exponentials even for several basis functions. Also note that some of the commercial em simulation softwares, like *em* from SONNET, use only one basis function along a vertical metalization [31].

The first approach described above is quite straightforward, where one needs to write the spectral-domain Green's functions in terms of exponentials of  $z$  and  $z'$  with complex coefficients and to apply the GPOF method for each complex coefficient. Therefore, there is no need to give further details for this approach. On the other hand, since the application of the second approach requires some work in the spectral-domain, it would be instructive to give the procedure and the details:

1. Write the spectral-domain Green's functions into the sum of exponentials of  $z$  and  $z'$  with complex coefficients.

2. Express the spatial-domain Green's functions in the MoM matrix entries as the inverse transforms of their spectral-domain representations using Eq. (2.57).
3. Evaluate the integrals over  $z$  and/or  $z'$  variables analytically.
4. Approximate the resultant expression by complex exponentials via the GPOF method.
5. Transform the whole expression into the spatial domain via the Sommerfeld identity Eq. (2.62), getting an auxiliary function  $F_{x,zz,zz}^{q-A}$  which has the same form as Eq. (2.63).
6. Evaluate the remaining inner-product integrals analytically in the spatial domain.

The exponential approximation with the GPOF method in item 4, should be performed with care, because it has been observed that the functions obtained after evaluating  $z$  and  $z'$  integrals may contain peaks for intermediate values of  $k_\rho$ . Therefore, to capture such behaviors efficiently, the two-level approximation scheme is extended to three levels for these terms, as explained in Chapter 2. Hence, it is guaranteed that the spectral-domain auxiliary functions are approximated successfully. It should also be noted that addition of multiple vertical strips will not increase the computational cost of this technique, provided that all vertical strips employ the same number of basis functions. This is because the MoM matrix entries corresponding to the basis functions on a vertical strip are obtained as a function of  $\rho$  and because the domains of integrations along the vertical strips are the same. In other words, once the interaction between a basis and a testing functions on a vertical strip is calculated, the same expression can be used with a different value of  $\rho$  for the calculation of the reaction of the same basis function and a testing function (or vice versa) located on another vertical strip at a distance of  $\rho$ .

To demonstrate this technique on an example, the following inner-product

term involving an integration on  $z$ -variable is considered:

$$\begin{aligned} \langle T_z^{(l')}, G_{zx}^A * B_x^{(mn)} \rangle &= \iint dz dy T_z^{(l')}(y, z) \\ &\cdot \iint dx' dy' G_{zx}^A(x - x', y - y', z, z' = \text{cons.}) B_x^{(mn)}(x', y') \quad (3.21) \end{aligned}$$

The first step of the procedure is to write the spectral-domain Green's function  $\tilde{G}_{zx}^A$  (2.36) in the form of Eq. (A.6), where  $z$  and  $z'$  dependencies are explicit. Then, the spatial-domain Green's function  $G_{zx}^A$  in Eq. (3.21) is replaced by the inverse transform of the spectral-domain Green's function  $\tilde{G}_{zx}^A$ , (A.6). Hence, the inner-product term in Eq. (3.21) becomes

$$\begin{aligned} \langle T_z^{(l')}, G_{zx}^A * B_x^{(mn)} \rangle &= \iint dz dy T_z^{(l')}(y) T_z^{(l')}(z) \\ &\cdot \iint dx' dy' \left\{ \frac{1}{4\pi} \int_{SIP} dk_\rho k_\rho H_0^{(2)}(k_\rho |\rho - \rho'|) \tilde{G}_{zx}^A(k_\rho, z) \right\} B_x^{(mn)}(x', y') \quad (3.22) \end{aligned}$$

where the separability of the basis functions is utilized,  $T_z^{(l')}(y, z) = T_z^{(l')}(y) T_z^{(l')}(z)$ . After changing the order of integrations, the following auxiliary function is defined and cast into closed form via the Sommerfeld identity:

$$\begin{aligned} F_{zx}^A &\stackrel{\text{def}}{=} \int dz T_z^{(l')}(z) \frac{1}{4\pi} \int_{SIP} dk_\rho k_\rho H_0^{(2)}(k_\rho |\rho - \rho'|) \frac{\tilde{G}_{zx}^A(k_\rho, z)}{-jk_x} \\ &\cong \frac{1}{4\pi} \int_{SIP} dk_\rho k_\rho H_0^{(2)}(k_\rho |\rho - \rho'|) \cdot \text{GPOF} \left\{ \int dz T_z^{(l')}(z) \frac{\tilde{G}_{zx}^A(k_\rho, z)}{-jk_x} \right\} \quad (3.23) \end{aligned}$$

where  $\text{GPOF}\{\cdot\}$  designates the approximation process with complex exponentials via the GPOF method. Note that  $\tilde{G}_{zx}^A$  has a multiplicative term of  $-jk_x$ , which needs to be eliminated for being able to apply the GPOF method. This is the reason why  $\tilde{G}_{zx}^A$  is divided by  $-jk_x$  and its effect is added in the spatial domain as a derivative with respect to  $x'$ . Therefore, the argument of the  $\text{GPOF}\{\cdot\}$  operator is approximated with complex exponentials without  $-jk_x$  term, resulting in the following inner product expression:

$$\langle T_z^{(l')}, G_{zx}^A * B_x^{(mn)} \rangle = - \int dy T_z^{(l')}(y) \iint dx' dy' B_x^{(mn)}(x', y') \frac{\partial}{\partial x'} F_{zx}^A \quad (3.24)$$

The derivative of  $F_{zx}^A$  with respect to  $x'$  is carried over to the basis function by using the chain rule

$$\frac{\partial}{\partial x'} \left[ B_x^{(mn)}(x', y') F_{zx}^A \right] = \frac{\partial}{\partial x'} B_x^{(mn)}(x', y') F_{zx}^A + B_x^{(mn)}(x', y') \frac{\partial}{\partial x'} F_{zx}^A \quad (3.25)$$

and the inner-product (3.21) reduces to

$$\begin{aligned} \langle T_z^{(l')}, G_{zx}^A * B_x^{(mn)} \rangle &= - \int dy T_z^{(l')}(y) \int dy' \left[ B_x^{(mn)}(x', y') F_{zx}^A \right] \Big|_{x' \in \Omega_B} \\ &\quad + \int dy T_z^{(l')}(y) \iint dx' dy' F_{zx}^A \frac{\partial}{\partial x'} B_x^{(mn)}(x', y') \end{aligned} \quad (3.26)$$

where  $\Omega_B$  is the boundary of the domain of the basis function. Following the substitutions  $x - x' = u$  and  $y - y' = v$ , the inner-product expression (3.26) is further simplified to

$$\begin{aligned} \langle T_z^{(l')}, G_{zx}^A * B_x^{(mn)} \rangle &= \int dv F_{zx}^A \int dy \left[ T_z^{(l')}(y) B_x^{(mn)}(x - u, y - v) \right] \Big|_{x' \in \Omega_B} \\ &\quad + \iint du dv F_{zx}^A \int dy T_z^{(l')}(y) \frac{\partial}{\partial x'} B_x^{(mn)}(x - u, y - v) \end{aligned} \quad (3.27)$$

where  $x = x_i$ ,  $x$ -coordinate of the vertical metalization, and the integrals over  $y$  are evaluated analytically. Note that the first term in Eq. (3.27) drops for the rooftop basis functions, but it must be evaluated for the basis functions that are not zero at the boundaries such as half-rooftop functions. The evaluation of the other inner-products, given in Eqs. (3.13)-(3.17), are performed similarly, so they are not given here for the sake of brevity, but presented in Appendix B.

### 3.1.2 Singularities Encountered in the Application of MoM

Let us consider, for the sake of illustration, the cross-section of a planar circuit with a vertical connection as shown in Fig. 3.3, where the vertical strip is placed in the  $y$  direction. Note that the continuity of the current at the intersection of the horizontal and vertical conductors is satisfied by simply setting  $2I_x = -I_z$  where  $I_x$  and  $I_z$  are the magnitudes of  $B_x$  and  $B_z$ , respectively. Therefore, the inner-product terms due to the basis functions indicated by dashed lines in the figure, are combined in the same matrix term. Since discontinuous basis functions are to be used at the intersection points, singularities are encountered in the evaluations of the MoM matrix entries due to the differentiations of the basis functions. Note

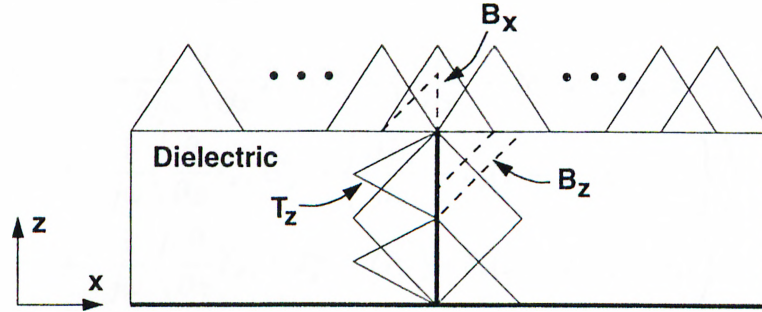


Figure 3.3: Cross-section of a planar circuit with a vertical connection showing the discontinuous basis functions.

that the derivatives of the testing functions do not create any singularity since rooftop functions are used for the testing functions on both horizontal and vertical metalizations.

In order to study these singularities, a MoM matrix entry involving the basis functions in the horizontal and the vertical directions at the intersection point is written as follows:

$$Z_{xz}^{qe} = -\frac{1}{2j\omega} \left\langle T_x, \frac{\partial}{\partial x} \left[ G_x^{qe} * \frac{\partial B_x}{\partial x} \right] \right\rangle + \frac{1}{j\omega} \left\langle T_x, \frac{\partial}{\partial x} \left[ G_z^{qe} * \frac{\partial B_z}{\partial z} \right] \right\rangle \quad (3.28)$$

where both  $B_x$  and  $B_z$  are discontinuous at the junction, and the vertical metalization is like a ribbon with a finite width in  $y$ -direction. Since the basis functions are discontinuous, their derivatives can be written as the sum of continuous and singular parts, respectively, as

$$\begin{aligned} Z_{xz}^{qe} = & -\frac{1}{2j\omega} \left\langle \frac{\partial}{\partial x} T_x, G_x^{qe} * \left\{ \frac{\partial B_x}{\partial x} - 2\delta_y(x - x_i, z - z_i) \right\} \right. \\ & + \left. G_x^{qe} * 2\delta_y(x - x_i, z - z_i) \right\rangle + \frac{1}{j\omega} \left\langle \frac{\partial}{\partial x} T_x, G_z^{qe} * \left\{ \frac{\partial B_z}{\partial z} - \delta_y(x - x_i, z - z_i) \right\} \right. \\ & + \left. G_z^{qe} * \delta_y(x - x_i, z - z_i) \right\rangle \end{aligned} \quad (3.29)$$

Where,  $\delta_y(x - x_i, z - z_i)$  represents a line source in  $y$ -direction at the junction point which is created by the derivatives of the discontinuous basis functions. By

recombining the terms, one can obtain the following expression:

$$\begin{aligned}
 Z_{xz}^{qe} &= -\frac{1}{2j\omega} \left\langle \frac{\partial}{\partial x} T_x, G_x^{qe} * \left\{ \frac{\partial B_x}{\partial x} - 2\delta_y(x - x_i, z - z_i) \right\} \right\rangle \\
 &+ \frac{1}{j\omega} \left\langle \frac{\partial}{\partial x} T_x, G_z^{qe} * \left\{ \frac{\partial B_z}{\partial z} - \delta_y(x - x_i, z - z_i) \right\} \right\rangle \\
 &+ \frac{1}{j\omega} \left\langle \frac{\partial}{\partial x} T_x, \{G_z^{qe} - G_x^{qe}\} * \delta_y(x - x_i, z - z_i) \right\rangle \quad (3.30)
 \end{aligned}$$

For small  $\rho$  values, the last term in Eq. 3.30 can be neglected since  $G_z^{qe} \approx G_x^{qe}$  at  $z = z'$  as  $\rho \rightarrow 0$ , that is, the contribution of the line sources resulted from the derivatives of the basis functions, is ignored. The accuracy of this assumption is verified on some examples.

## 3.2 The Method of De-embedding of the Port Discontinuities

Because there exists fringing, reactive and evanescent fields in the vicinity of the source and load terminals, circuit parameters, such as input impedance and S-parameters, are obtained by removing these higher order effects from the calculations, which is called de-embedding [32]. Note that the EM simulation technique presented in this thesis uses impressed current sources to characterize an N-port circuit [33].

Since the current densities on the conductors, including the port transmission lines, have already been calculated, the current on each port transmission line is written as a linear combination of complex exponentials by using the GPOF method as

$$I(l) \approx \sum_{i=1}^N I_i e^{(\alpha_i + j\beta_i)l} \quad (3.31)$$

where  $l$  is the distance along the port transmission line. If the magnitudes of the higher order modes on the port transmission lines are sufficiently small, the current can be expressed by only two exponentials with complex coefficients corresponding to the incident and reflected current waves at the



corresponding ports. Then, the S-parameters are calculated from the coefficients of these exponentials and transferred to the desired reference planes [34]. These S-parameters are inherently normalized and referenced to the characteristic impedances of the port transmission lines. Note that, the propagation constants on the transmission lines are also found as the by-product of this method which enables us to extract the effective permittivity at each frequency of operation. However, in some cases, it might be numerically difficult to extract the propagation constant and the unknown coefficients of the exponentials with sufficient precision from the same current samples by direct application of the GPOF method. This situation occurs in MIC structures where the electrical length of the port transmission line is very small. In such cases, one can find the propagation constant from a sufficiently long test transmission line, which has the same characteristics with the original port transmission line, and then use this propagation constant to fit the current on the original line with complex exponentials through a linear least-squares algorithm [35]. Finally, the S-parameters obtained are converted to the S-parameters with the reference impedance of  $50 \Omega$ . For a two port-network, the matrix relation, used to find the S-parameters, can be written in the following form

$$\begin{bmatrix} I_{11}^+ & I_{12}^+ & 0 & 0 \\ 0 & 0 & I_{11}^+ & I_{12}^+ \\ I_{21}^+ & I_{22}^+ & 0 & 0 \\ 0 & 0 & I_{21}^+ & I_{22}^+ \end{bmatrix} \begin{bmatrix} S_{11} \\ S_{12} \\ S_{21} \\ S_{22} \end{bmatrix} = \begin{bmatrix} -I_{11}^- \\ -I_{12}^- \\ -I_{21}^- \\ -I_{22}^- \end{bmatrix} \quad (3.32)$$

where  $I_{ij}^+$  and  $I_{ij}^-$  are the current coefficients for the incident and reflected waves, respectively, for  $i$ 'th port excitation and  $j$ 'th port observation. Note that, in the calculation of the S-parameters it is not necessary to terminate the ports because both the transmitted and reflected waves are considered in the calculations.

This derivation of the S-parameters does not require the knowledge of the characteristic impedances of the port transmission lines. However, the need to convert these S-parameters to the S-parameters with a known reference impedance (usually  $50 \Omega$ ) makes it necessary to know the characteristic impedances of the port transmission lines. Since rigorous calculation of the

characteristic impedance of a microstrip line in a multilayer medium is quite time consuming, a method based on a quasi-TEM approach is used here, which provides a closed-form expression for the characteristic impedance of a microstrip line and a stripline [36,37]. This method is valid when the transverse components of the current densities on the port transmission lines are very small as compared to the longitudinal components, which is usually the case for printed circuits. Note that the characteristic impedance found from the quasi-TEM approach does not change with frequency, whereas in reality it changes with frequency [38, 39]. By using a frequency dependent effective permittivity in the closed-form expression for the characteristic impedance, the quasi-TEM approximation is somewhat improved (see Fig. 3.4).

To calculate the S-parameters of a general N-port network with different characteristic impedances  $Z_0$ , at port  $i$ , the following pseudo code, which fills the matrices in Eq. (3.32), is given here for convenience

```

A ← 0
n ← number of ports
for i = 0, 1, 2, ..., n - 1
begin
  for l = 0, 1, 2, ..., n - 1
  begin
    for m = 0, 1, 2, ..., n - 1
    begin
       $A_{i*n+m, l+m*n} \leftarrow I_{il}^+ * \text{sqrt}(Z_{0l})$ 
    end
     $B_{i*n+l} \leftarrow -I_{il}^- * \text{sqrt}(Z_{0l})$ 
  end
end
end

```

Then, the S-parameters are found from  $\mathbf{S} = \mathbf{A}^{-1}\mathbf{B}$ .

### 3.3 Numerical Examples

In this section, the application of the formulation presented in this thesis is demonstrated on some practical geometries and the results are compared to those

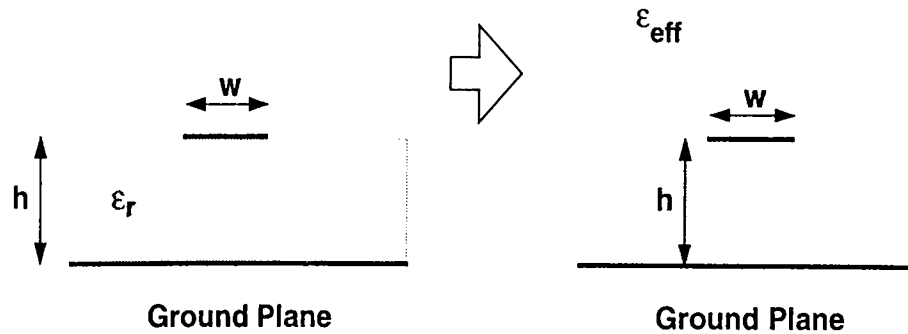


Figure 3.4: Meaning of  $\epsilon_{eff}$  for a microstrip transmission line.

obtained from a commercial EM analysis software, *em* from SONNET Software Inc.

The main difference between *em* and this formulation is that *em* puts the circuit in a conducting box whose default wall conductivities are infinite [31]. The analysis of radiating structures in *em* requires adding loss to the system, but with the formulation presented here these structures can be characterized better, in the sense of accuracy and computational efficiency. One can refer to Carroll and Chang [40] for a general information on *em* software.

A typical uniform gridding of a planar circuit is shown in Fig. 3.5, where  $\Delta x$  and  $\Delta y$  are constant through the whole geometry. Note that the simulation software developed to implement the algorithm which is presented in this thesis, can accept non-uniform gridding as well. However, it should be stated that non-uniform gridding increases the matrix-fill time in some cases due to the increased complexity of the evaluation of reaction integrals. In addition to that, similarities between the reaction integrals are significantly reduced in the case of a non-uniform gridding. Therefore, one should not use non-uniform gridding unless it is necessary. The arrows on the port transmission lines in Fig. 3.5 show the reference planes used in the calculation and in the de-embedding of the circuit

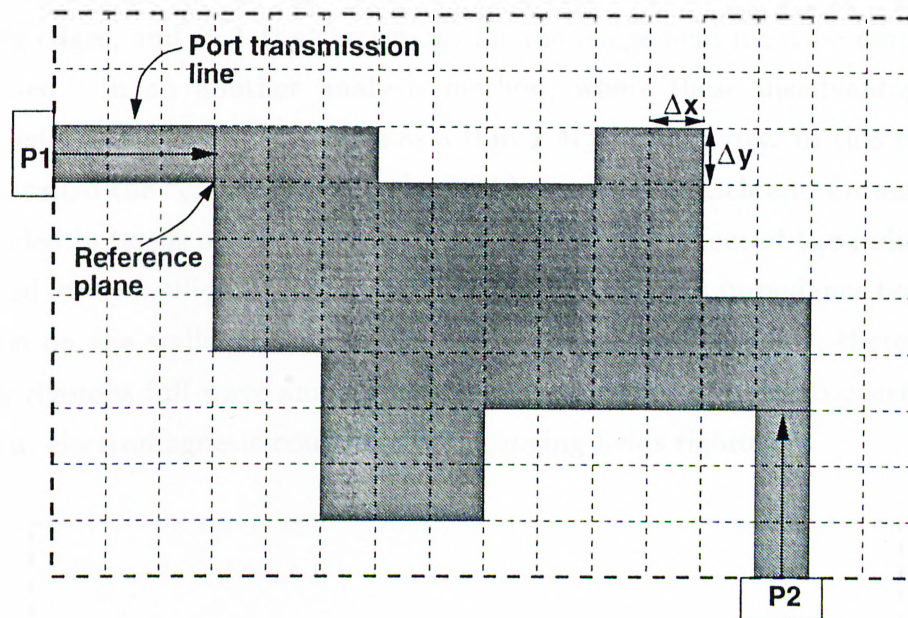


Figure 3.5: Typical gridding which is used in the simulation software.

parameters. The S-parameters provided here are normalized with respect to  $50 \Omega$  reference impedance.

### 3.3.1 Microstrip Patch Antenna

A single microstrip patch antenna is one of the simplest radiating structure that can be built on a multilayer medium. Single patch antennas and patch antenna arrays are widely used in mobile microwave communication systems and airborne applications [41–44]. Moreover, the possibility of incorporating the antenna with active circuits on the same substrate increases the importance of the microstrip antennas.

The simplest model of a rectangular microstrip patch antenna considers the antenna as a transmission line which connects two parallel radiating slot impedances and called as the “transmission line model”. Although the transmission line model is simple, it has several disadvantages: *i.*) it is only useful

for the patches of rectangular shape, *ii.*) it ignores the field variations along the radiating edges, and *iii.*) the corrections for the fringe field must be empirically determined. In an another analysis method, where these disadvantages are eliminated, the antenna is modeled as a thin  $TM_z$  mode cavity. In this method, which is called the “cavity model”, the field between the patch and ground plane is expanded in terms of the cavity resonant modes. The effect of the radiation is accounted for by artificially increased dielectric loss or by an impedance boundary condition on the walls. However, despite of these simple models, there is still need for rigorous full-wave analysis of microstrip patch antennas to consider the radiation, electromagnetic couplings, and fringing fields rigorously.

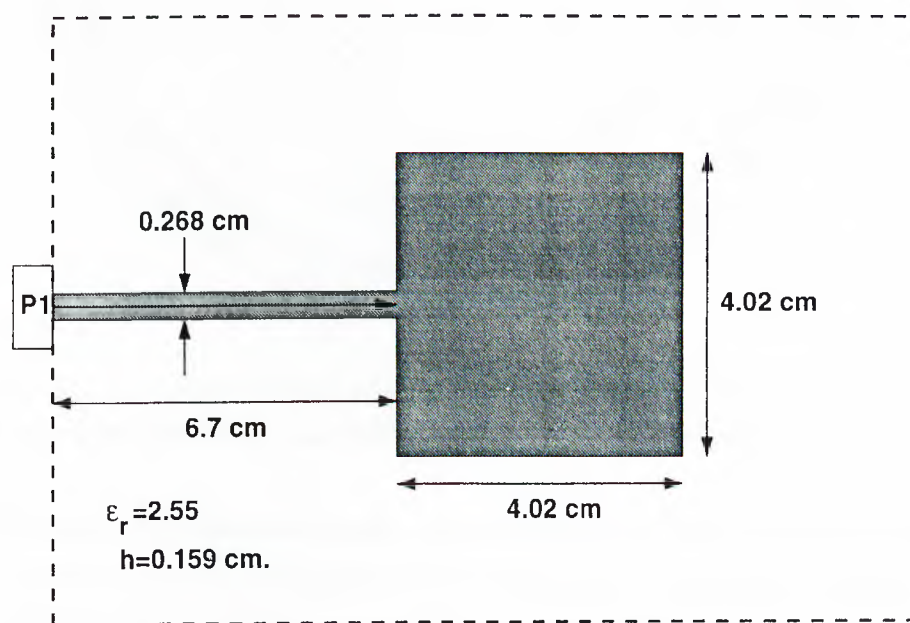


Figure 3.6: Geometry of a patch antenna.

A microstrip patch antenna, shown in Fig. 3.6, is analyzed as a first example and the results are given in Fig. 3.7. Note that the results of  $em$  are not smooth and contain artifacts. As stated previously, the formulation presented in this thesis has the advantage that the radiating structures can be analyzed rigorously since the radiation condition is automatically satisfied. In addition to that,



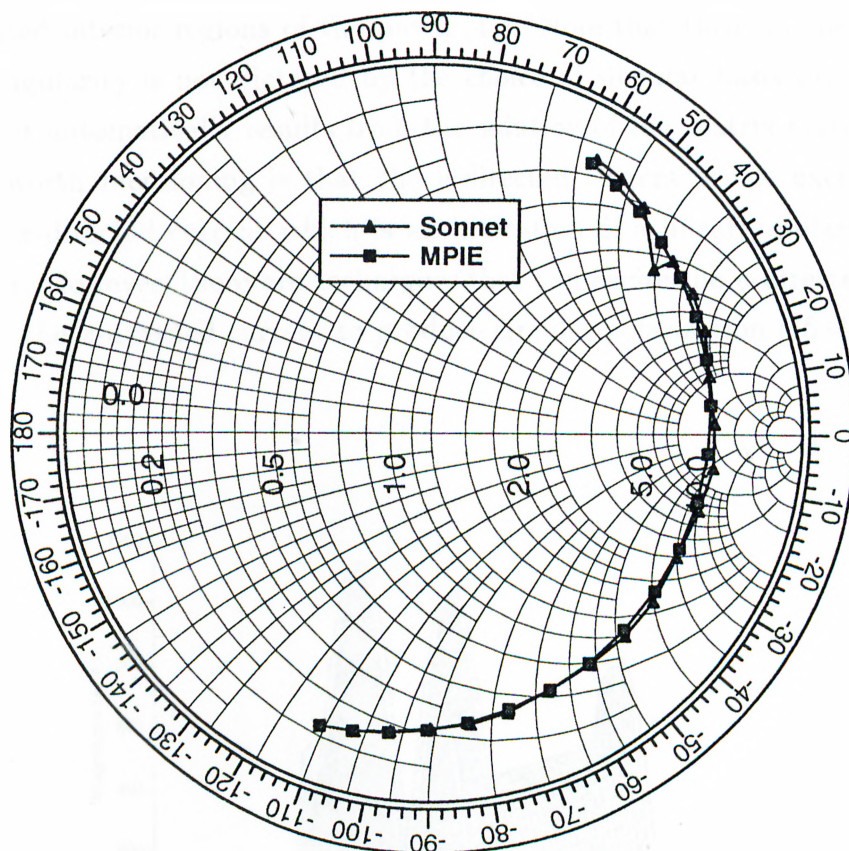


Figure 3.7:  $\Gamma_{in}$  of the patch antenna shown in Fig. 3.6. Frequency increases in the clock-wise direction ( $f_{start}=2200$  MHz,  $f_{stop}=2400$  MHz).

consideration of the surface waves is also inherent to the formulation resulting a rigorous analysis of coupling between the elements of an antenna array.

In order to give an idea about the current distribution on a planar structure, 3-D plots of the current density on the patch antenna near resonance are also given in Figs. 3.8 and 3.9. Note that at the edges of the patch parallel to x-axis, tangential components of the electric current density exhibit peaks due to the phenomena called as “edge singularity”. The reason of this behavior is that since it is assumed that the patch is perfectly conducting, the tangential electric field on the patch surface should be zero and this necessity requires a strong charge density at the edges to cancel the field generated by the charges which are

deposited interior regions of the patch [45]. Note that through the formulation this singularity is not dictated by the choice of singular basis functions at the edges, it automatically results from the solution of the matrix system. Another point worth mentioning is that the  $y$ -directed current is not excited as much as the  $x$ -directed current which is an indication of a linearly polarized far-field pattern. However, there are techniques that can excite the  $y$ -directed current as well as the  $x$ -directed current to produce circular polarization [46–48].

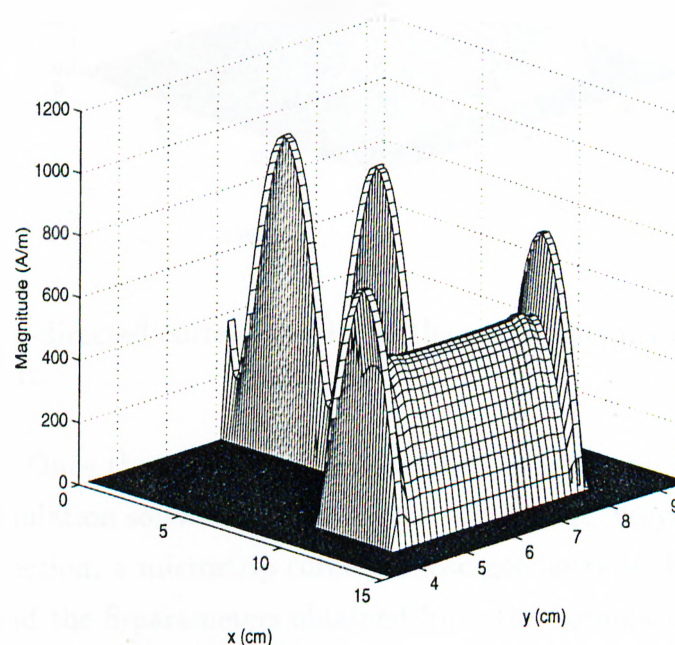


Figure 3.8:  $x$ -directed current density of the patch antenna shown in Fig. 3.6 at  $f = 2300$  MHz.

### 3.3.2 Microstrip Corner

Since the full-wave analysis of a MIC, including both passive and active components, requires a significant amount of CPU time, the accurate and fast characterization of passive components, like microstrip discontinuities, coupled lines, hybrids etc., plays an important role to find the equivalent lumped circuit

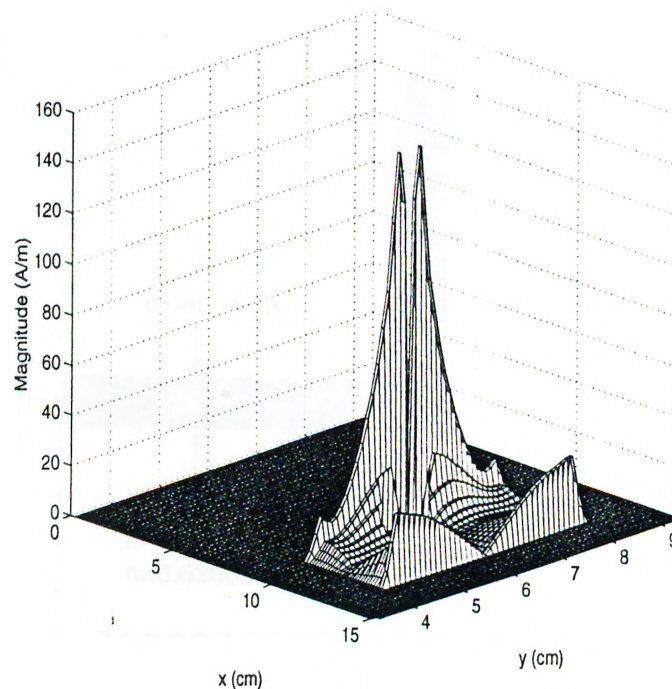


Figure 3.9:  $y$ -directed current density of the patch antenna shown in Fig. 3.6 at  $f = 2300$  MHz.

parameters. Once the lumped circuit parameters are found they can be used in a circuit simulation software to analyze the whole MIC very efficiently.

In this section, a microstrip corner, whose geometry is shown in Fig. 3.10, is analyzed, and the S-parameters obtained from the formulation presented in this thesis and from the *em* software are compared and are given in Figs. 3.11 and 3.12. Note that the capacitive behavior dominates at lower frequencies and as the frequency increases, the inductive behavior of the corner starts to be pronounced. To obtain better response in terms of the reflection coefficient, a small square region as indicated in the Fig. 3.10, is extracted from the corner resulting in a significant improvement through the operation band, Fig. 3.11. In practice, a mitered corner is commonly used instead of extracting a small square region.

Once the S-parameters of the microstrip corner have been obtained, the lumped circuit model parameters can easily be extracted for a given circuit model.



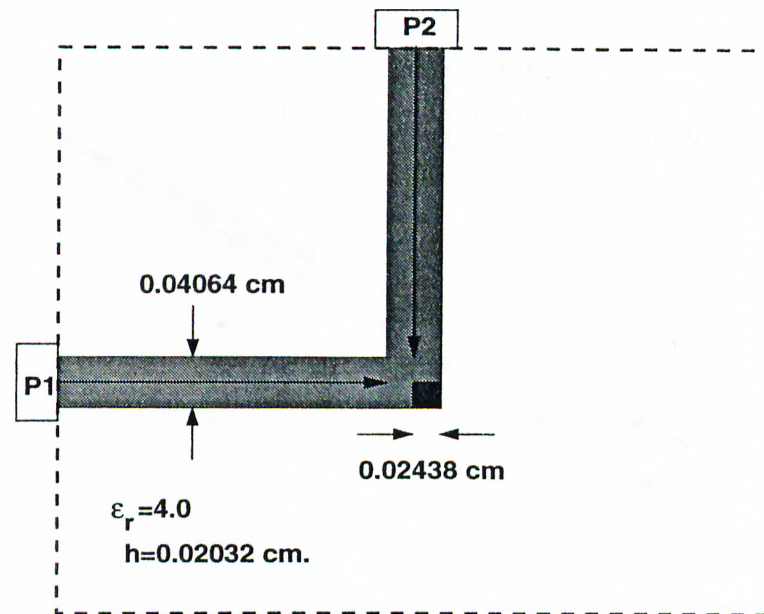
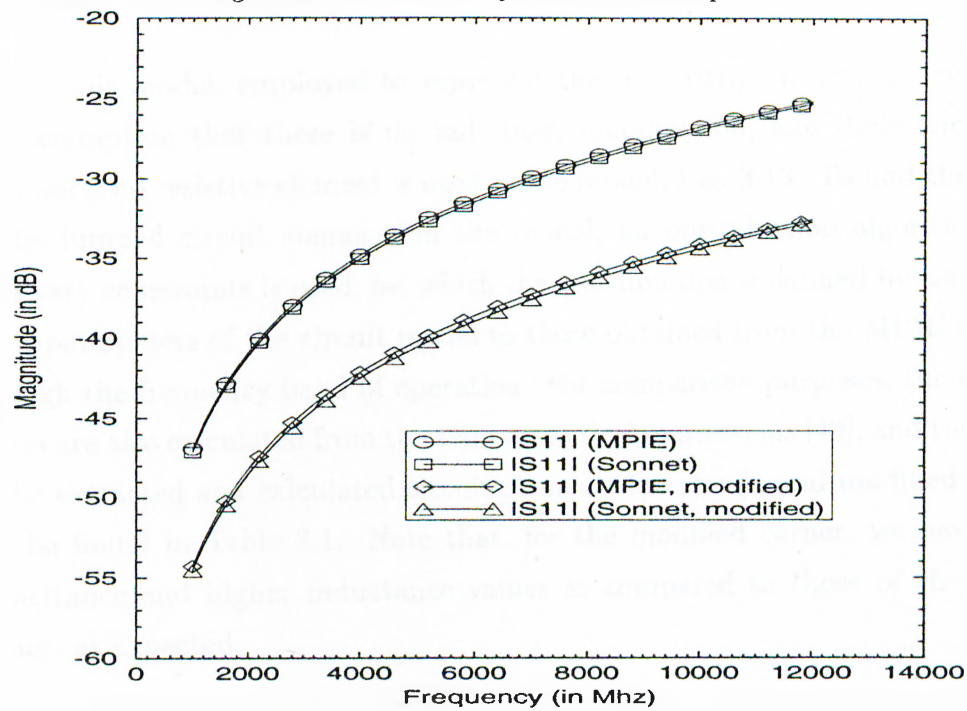


Figure 3.10: Geometry of a microstrip corner.

Figure 3.11: Magnitude of  $S_{11}$  of the microstrip corner shown in Fig. 3.10.

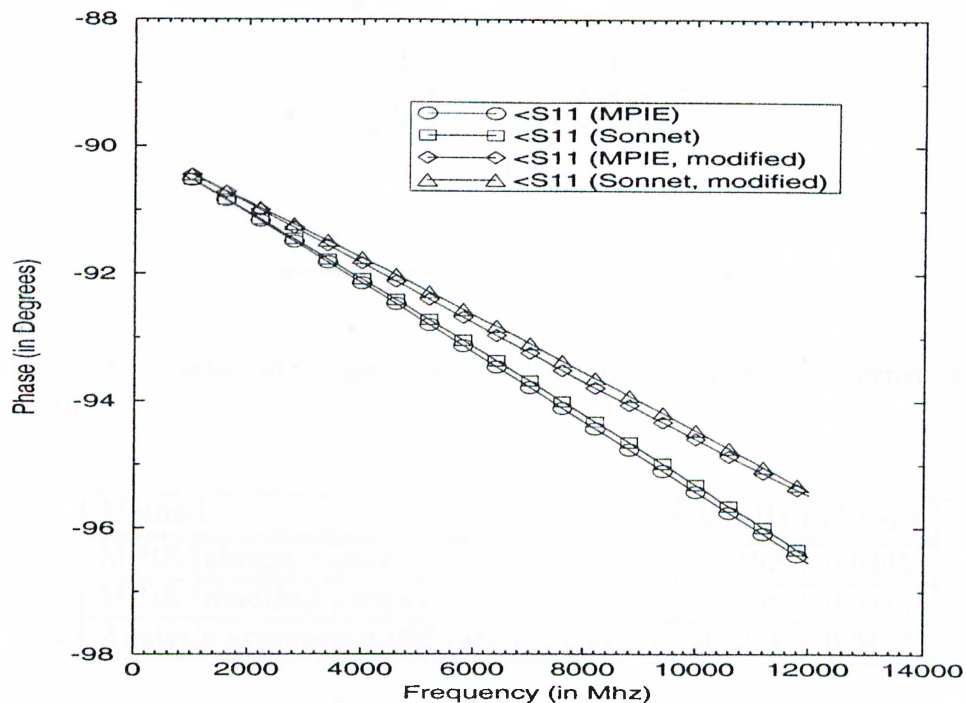


Figure 3.12: Phase of  $S_{11}$  of the microstrip corner shown in Fig. 3.10.

The circuit model, employed to represent the microstrip corner, is devised on the assumption that there is no radiation, metalization, and dielectric losses. Therefore, no resistive element is used in the model, Fig. 3.13. To find the values of the lumped circuit elements in the model, an optimization algorithm with necessary constraints is used, for which the cost function is defined by comparing the S-parameters of the circuit model to those obtained from the MPIE analysis through the frequency band of operation. For comparison purposes, the element values are also calculated from the semi-analytical expressions [49], and the values of the extracted and calculated circuit elements for abrupt and modified corners can be found in Table 3.1. Note that, for the modified corner, we have lower capacitance and higher inductance values as compared to those of the abrupt corner, as expected.

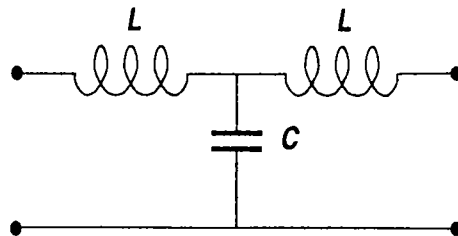


Figure 3.13: Equivalent lumped circuit model of the microstrip corner shown in Fig. 3.10.

Method	$L$ (nH)	$C$ (pF)
MPIE (abrupt corner)	0.0192	0.0445
MPIE (modified corner)	0.0236	0.0313
Analytic expressions [49] (abrupt corner)	0.0294	0.0432

Table 3.1: Equivalent lumped circuit values for the microstrip corner shown in Fig. 3.10.

### 3.3.3 Proximity Coupled Microstrip Patch Antenna

There are typically three definitions for the bandwidth of a microstrip patch antenna or an array: impedance bandwidth, pattern bandwidth and polarization bandwidth. The limiting factor for a single element is the impedance bandwidth, the pattern and polarization bandwidths vary relatively slow with frequency. One way to increase the impedance bandwidth is to increase the thickness of the dielectric material. However, as the thickness of the substrate increases, the impedance locus of the antenna becomes inductive, which makes the matching of the antenna difficult, and the surface wave excitation becomes higher, which causes spurious radiation. There are other techniques used to increase the impedance bandwidth of a patch antenna which can be listed as follows: *i.*) using a matching network to match the feed to the antenna over a broadband [50–52], *ii.*) using multiple resonators which are tuned to slightly different frequencies [53–57], *iii.*) introducing loss to the system at the expense of power efficiency,

and *iv.*) modifying the feeding structure of the antenna [58].

In this section, a proximity coupled patch antenna, as shown in Fig. 3.14, is analyzed, and the effects of the coupling is investigated for different coupling lengths,  $s$ . It is observed that the impedance locus of the antenna moves from the capacitive reactance region to the inductive reactance region as the coupling length increases, Fig. 3.15.

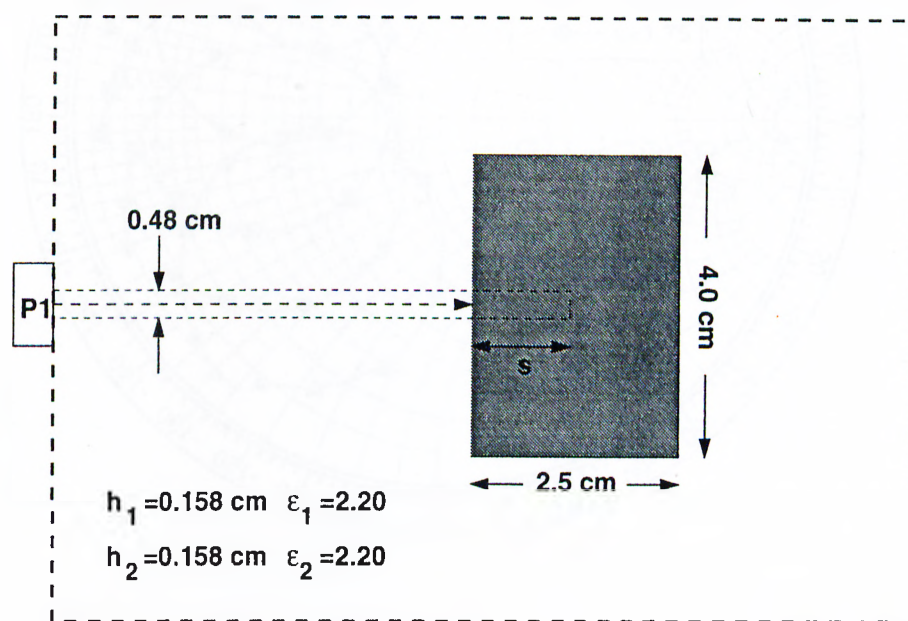


Figure 3.14: Geometry of a proximity coupled patch antenna.

The elements of the equivalent circuit model of the patch antenna, which is shown in Fig. 3.16, are also extracted by using the method described in the example of the microstrip corner. Note that the resistance in the model simulates the loss mechanisms due to the radiation and the surface waves. The element values of the lumped circuit model, which are obtained in this study for the coupling length of  $s=1.25$  cm, are compared to the values found in the literature, which were extracted from an experimental data, see Table 3.2. The difference in  $C_1$  could be attributed to the optimization algorithm, weights used in the optimization for the magnitude and phase terms, and the frequency band of interest, since it is found that the value of  $C_1$  depends considerably on these



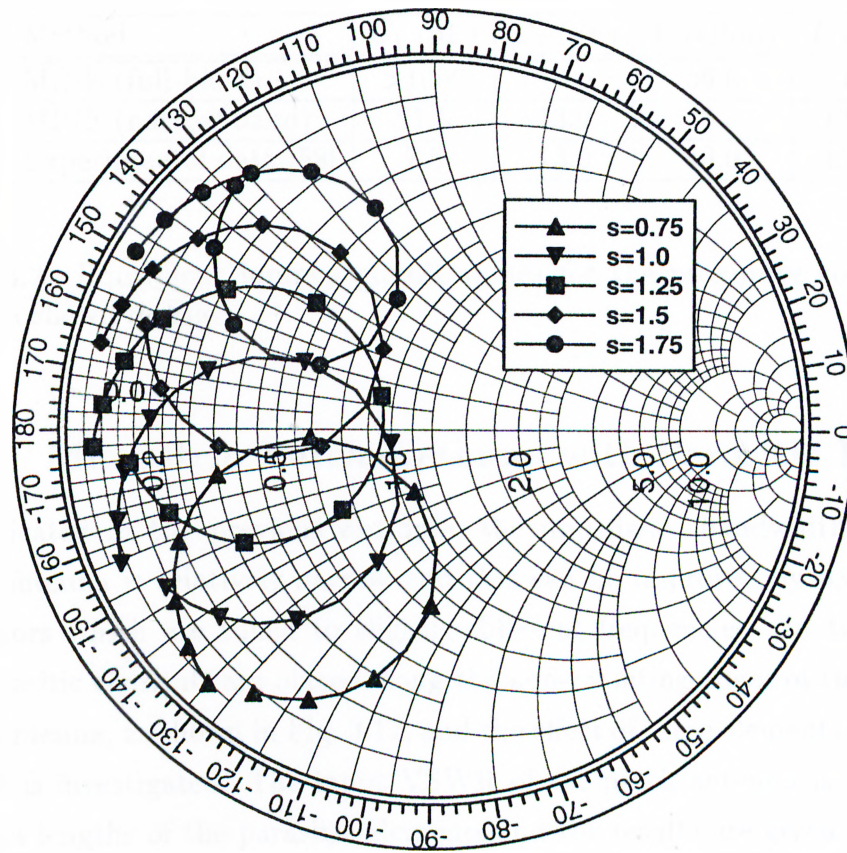


Figure 3.15:  $\Gamma_{in}$  of the proximity coupled patch antenna shown in Fig. 3.14. Frequency increases in the clock-wise direction ( $f_{start}=3000$  MHz,  $f_{stop}=4000$  MHz).

parameters.

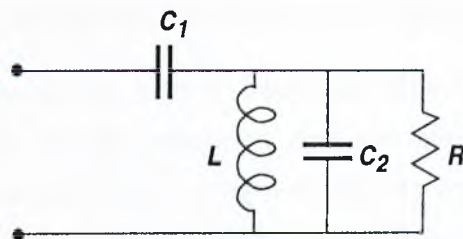


Figure 3.16: Equivalent lumped circuit model of the proximity coupled patch antenna shown in Fig. 3.14.

Method	$C_1$ (pF)	$C_2$ (pF)	$R$ (Ohm)	$L$ (pH)
MPIE (full-band)	>1000	16.5	36.6	116.8
MPIE (narrow-band)	21.5	13.9	40.3	138.2
Experimental data [58]	7.5	13.0	40.0	151.0

Table 3.2: Equivalent lumped circuit values for the proximity coupled patch antenna shown in Fig. 3.14.

### 3.3.4 Microstrip Patch Antenna with Parasitic Elements

As indicated in the previous example, the impedance bandwidth of a single patch antenna is relatively narrow and this can be improved by using multiple resonators which are tuned to slightly different frequencies. In this example, the parasitic elements are placed along the non-radiating edges of the microstrip patch antenna, as shown in Fig. 3.17, and the effect of these elements on the input VSWR is investigated. The input VSWR of the patch antenna is obtained for different lengths of the parasitic elements and the results are given in Fig. 3.18. Note that when the lengths of the resonators are equal to each other, the input VSWR has one global minimum and the antenna can only be operated around that point. On the other hand, it is also possible to select the resonator lengths different for which the input VSWR would have two local minimums, resulting in a dual-frequency operation of the antenna.

### 3.3.5 Four-pole Elliptic Band-pass Filter

It is highly desirable to obtain narrow band-pass filters with strong frequency selectivity, linear phase in the passband and low insertion loss. For some applications, requirements on the frequency selectivity and the insertion loss of a filter need to be strictly satisfied. For such applications, the elliptic filter is the optimum choice in the sense that it provides much steeper transition band for a given order, and relatively small insertion losses as compared to Butterworth

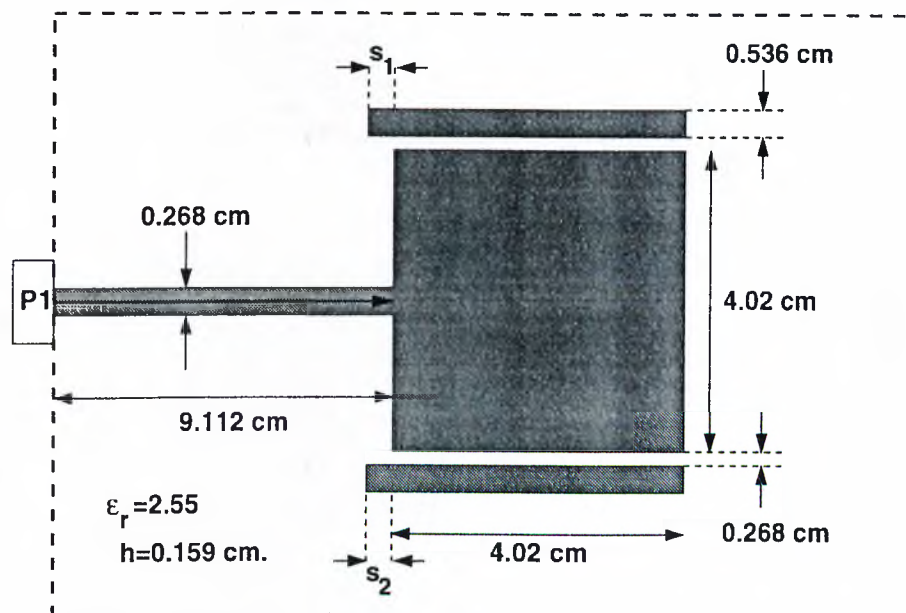


Figure 3.17: Geometry of the microstrip patch antenna with parasitics.

and Chebyshev filters. [59,60]. In circuits which have transmission channels in parallel, the poles of attenuation are created when the signals from different paths are added with proper phase and magnitude. Hence, such filters can be realized with low-loss cavity resonators which have cross-couplings between them.

In this example, a four-pole elliptic band-pass filter realized by cross-coupled resonators [61], Fig. 3.19, is analyzed, and the effect of the spacing,  $s$ , to the filter response is investigated. It is observed from Figs. 3.20 and 3.21 that the results of the method presented here and obtained from *em* are in good agreement with each other, and that there is an optimum spacing between the resonators for minimum insertion loss or broader bandwidth.

### 3.3.6 3 dB 90° Hybrid Coupler

Hybrid couplers are widely used in microwave engineering due to their unique features. One of the application areas of the hybrid couplers is the design of balanced amplifier in which the total input and output reflections of the whole

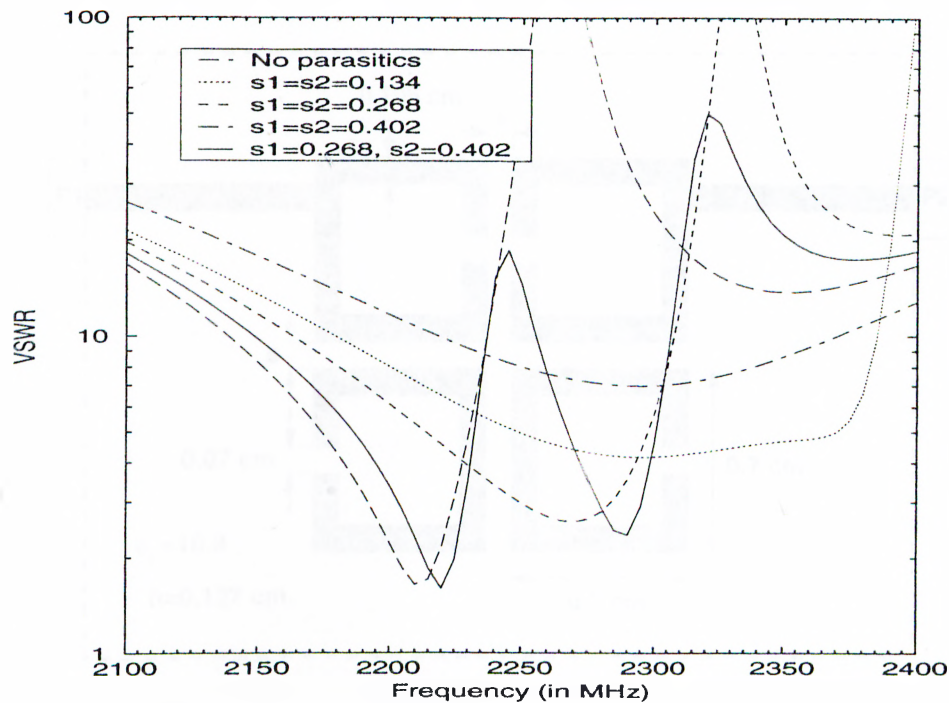


Figure 3.18: Input VSWR of the microstrip patch antenna with parasitics shown in Fig. 3.17.

amplifier can be reduced significantly with the use of the hybrid couplers.

In this section, a multilayer 3 dB  $90^\circ$  hybrid coupler, as shown in Fig. 3.22, is analyzed. The results obtained from the method presented in this thesis show a very good agreement with the results obtained from the *em* software, Figs. 3.23 and 3.24. Note that the phase difference and power coupling between the coupled ports are nearly constant and equal to  $90^\circ$  and 3 dB, respectively, through the operation band.



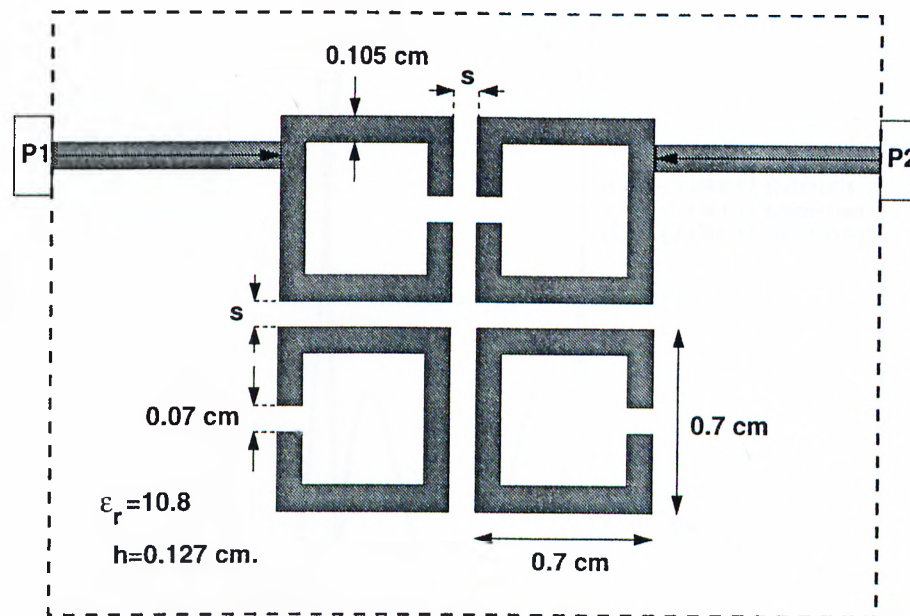
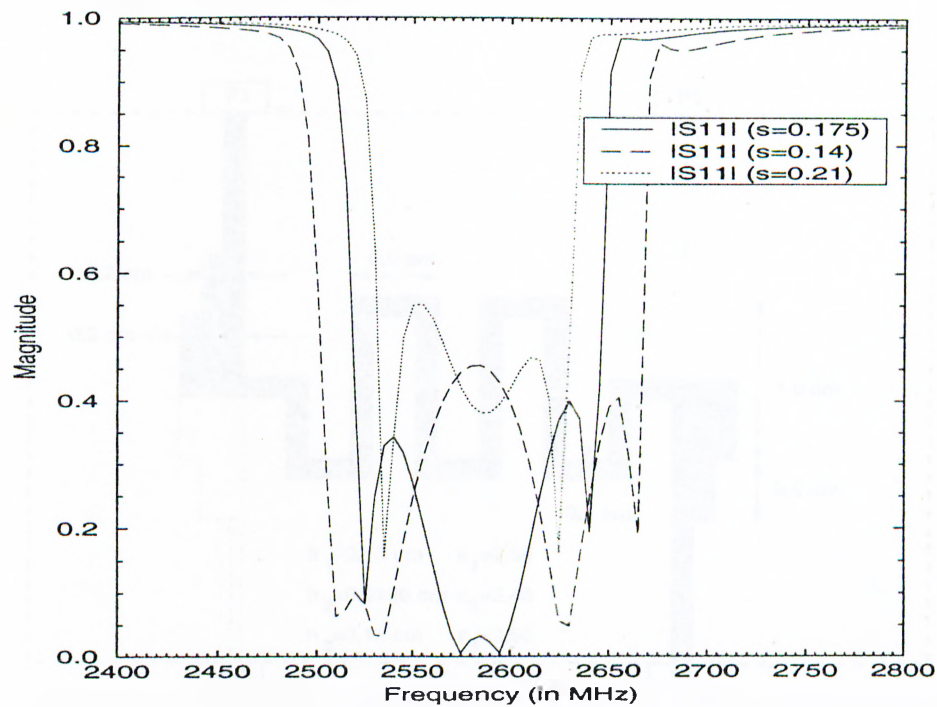


Figure 3.19: Geometry of a band-pass filter.

Figure 3.20: Magnitude of  $S_{11}$  of the band-pass filter shown in Fig. 3.19 for different  $s$  values.

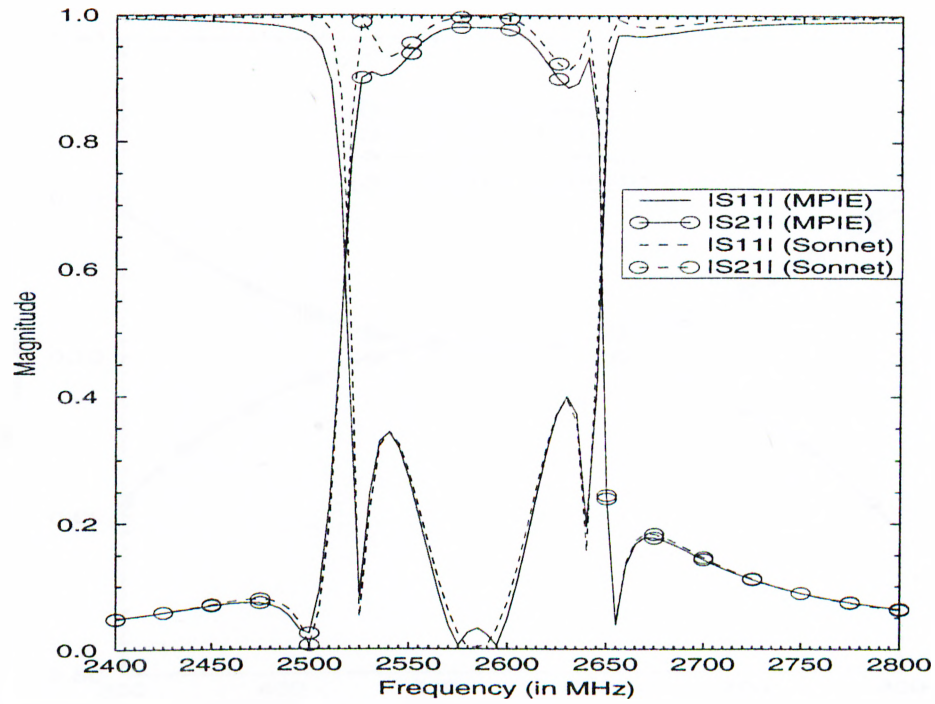


Figure 3.21: Magnitudes of  $S_{11}$  and  $S_{21}$  of the band-pass filter shown in Fig. 3.19 for  $s=0.175$  cm.

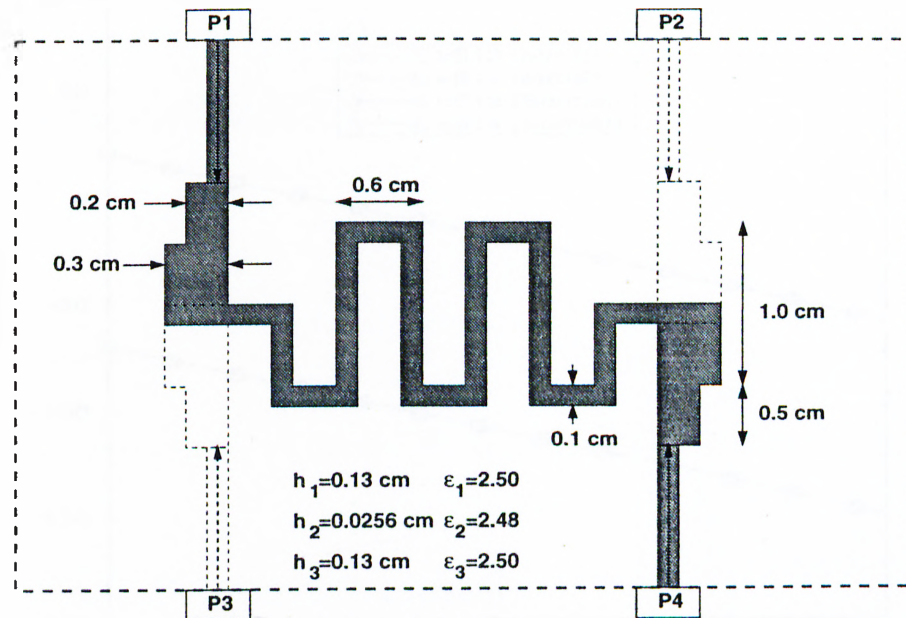
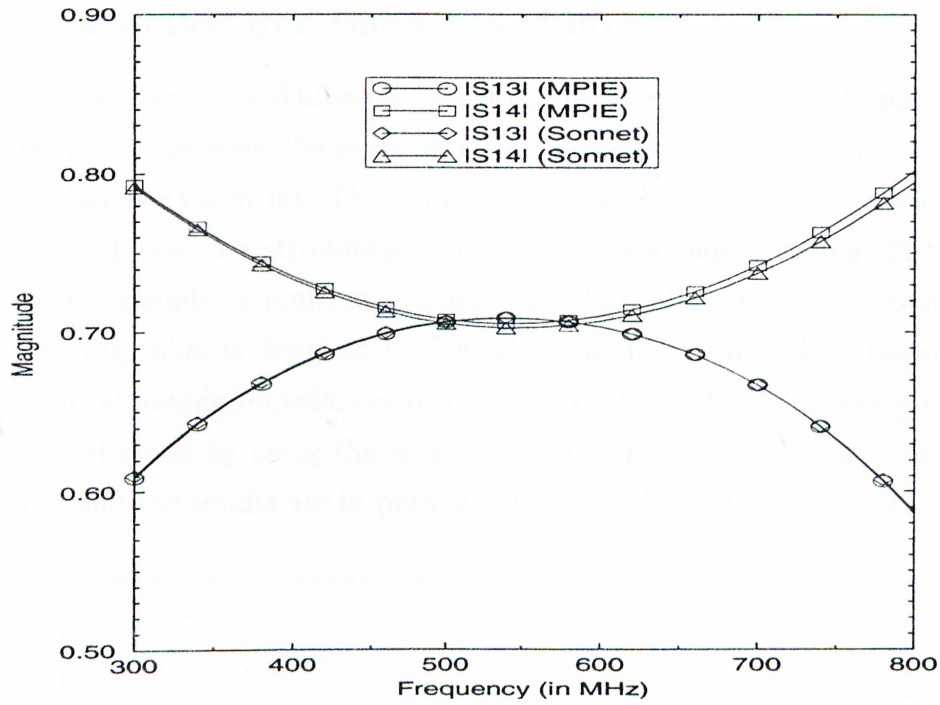
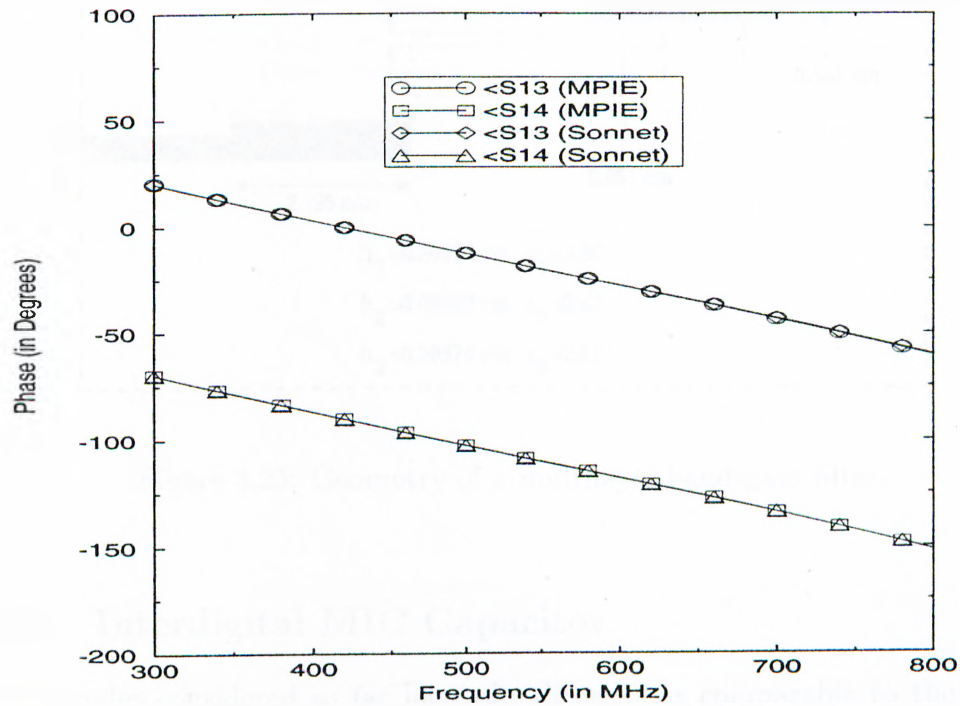


Figure 3.22: Geometry of a hybrid coupler.

Figure 3.23: Magnitudes of  $S_{13}$  and  $S_{14}$  of the hybrid coupler shown in Fig. 3.22.Figure 3.24: Phases of  $S_{13}$  and  $S_{14}$  of the hybrid coupler shown in Fig. 3.22.

### 3.3.7 Coupled-line Band-pass Filter

In designing edge-coupled filters, it might be necessary to have small spacings, i.e., large couplings, between the resonant elements which would make the production of such filters very difficult. This difficulty can be circumvented by implementing such coupled lines in a stripline geometry with broad-side coupling [62,63].

In this example, a multilayer band-pass filter with broad-side coupling, as shown in Fig. 3.25, is designed by following the design procedure based on the even- and odd-mode impedances of the coupled lines [37]. The analysis of this filter is performed by using the method described in this thesis and by the *em* software, and the results are in perfect agreement, Figs. 3.26 and 3.27.

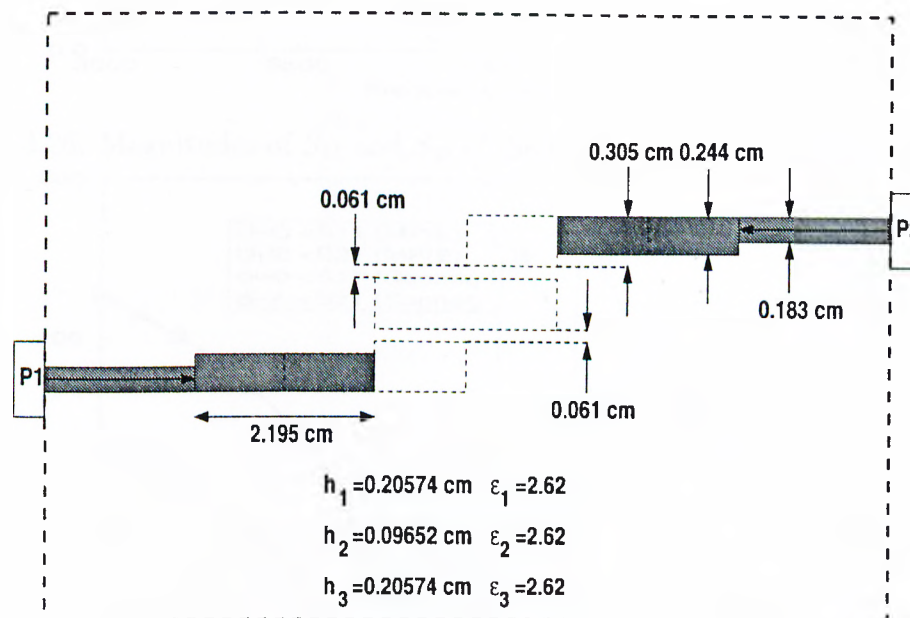


Figure 3.25: Geometry of a multilayer band-pass filter.

### 3.3.8 Interdigital MIC Capacitor

All examples considered so far have the dimensions comparable to the guided wavelength at the operating frequency. Since most of the integrated circuit



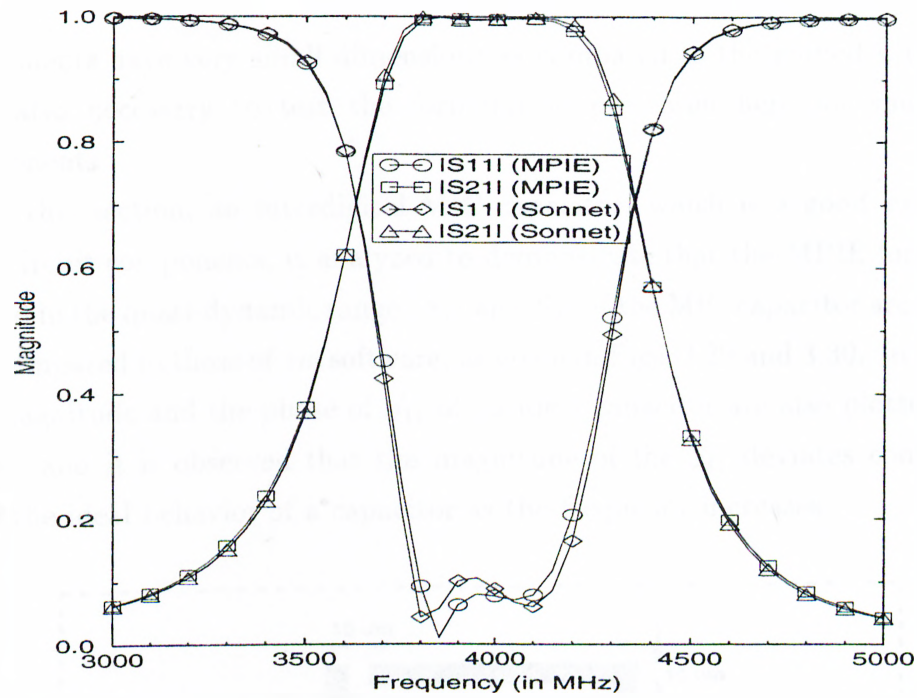


Figure 3.26: Magnitudes of  $S_{11}$  and  $S_{21}$  of the band-pass filter shown in Fig. 3.25.

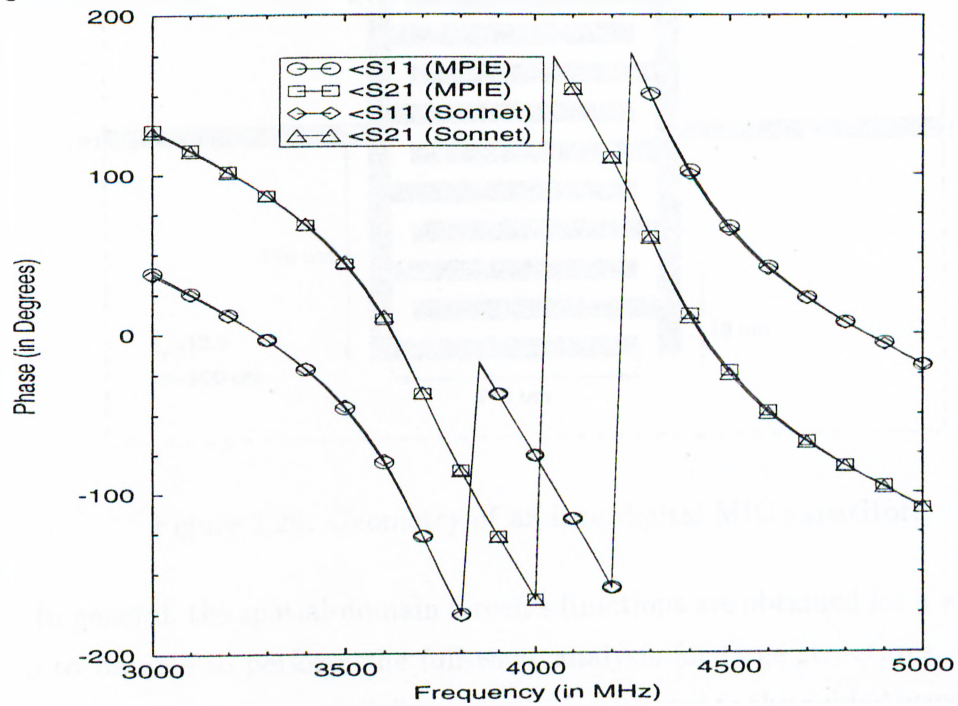


Figure 3.27: Phases of  $S_{11}$  and  $S_{21}$  of the band-pass filter shown in Fig. 3.25.

components have very small dimensions as compared to the guided wavelength, it is also necessary to test the formulation presented here for such circuit components.

In this section, an interdigital MIC capacitor, which is a good example of such circuit components, is analyzed to demonstrate that the MPIE formulation is valid in the quasi-dynamic range.  $S_{11}$  and  $S_{21}$  of the MIC capacitor are obtained and compared to those of *em* software, as given in Figs. 3.29 and 3.30. In addition, the magnitude and the phase of  $S_{11}$  of an ideal capacitor are also plotted on the figures and it is observed that the magnitude of the  $S_{11}$  deviates considerably from the ideal behavior of a capacitor as the frequency increases.

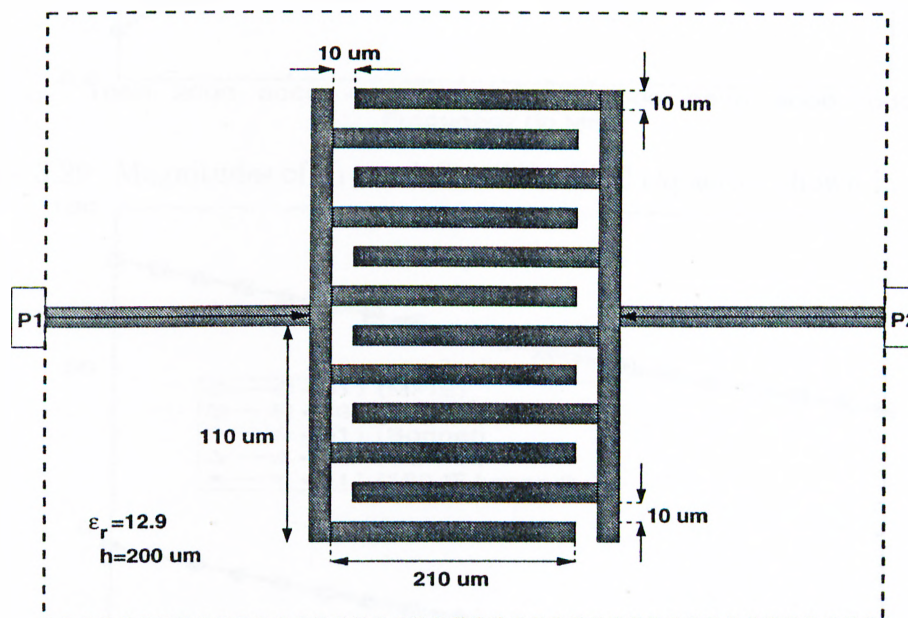


Figure 3.28: Geometry of an interdigital MIC capacitor.

In general, the spatial-domain Green's functions are obtained for a wide range of  $\rho$  to be able to perform the full-wave analysis for large structures. However, since this structure has small dimensions as compared to the guided wavelength, it would be instructive to investigate the effects of using less number of exponentials for the paths  $C_{ap2}$  and  $C_{ap1}$  shown in Fig. 2.2 in the application of GPOF. In other

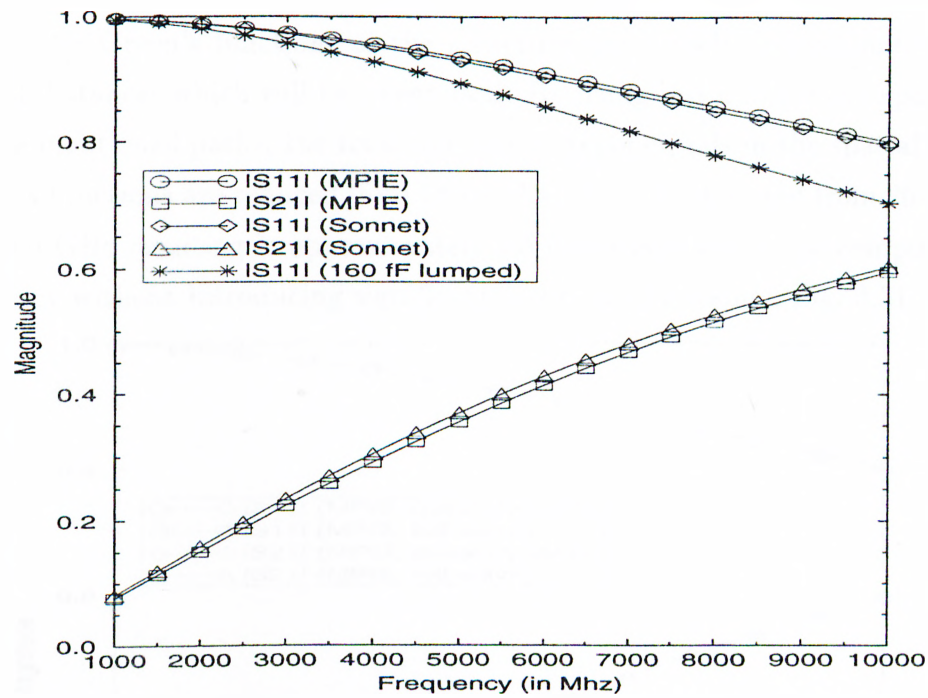


Figure 3.29: Magnitudes of  $S_{11}$  and  $S_{21}$  of the MIC capacitor shown in Fig. 3.28.

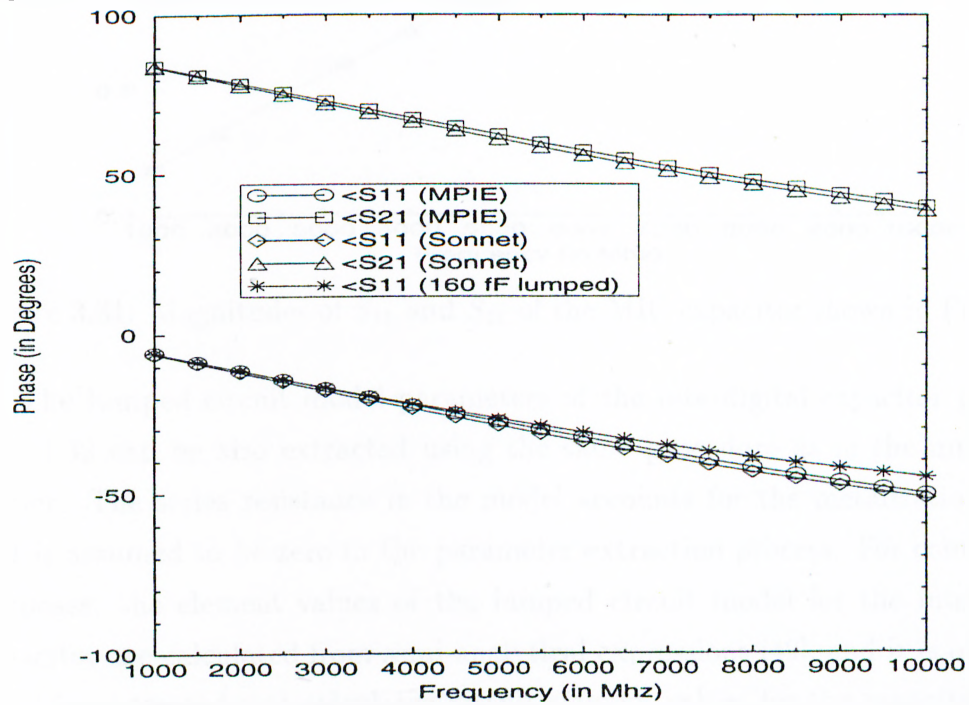


Figure 3.30: Phases of  $S_{11}$  and  $S_{21}$  of the MIC capacitor shown in Fig. 3.28.

words, the Green's functions of the structure are weakly approximated in the spatial distances which will be never used. By using less number of exponentials for the mentioned paths, the total number of exponentials in the spatial-domain Green's functions are reduced from 18 to 12 at  $f = 1.0$  GHz, and from 26 to 17 at  $f = 10.0$  GHz resulting in approximately 1.5 times increase in the computational efficiency without introducing significant errors to the results, Fig. 3.31.

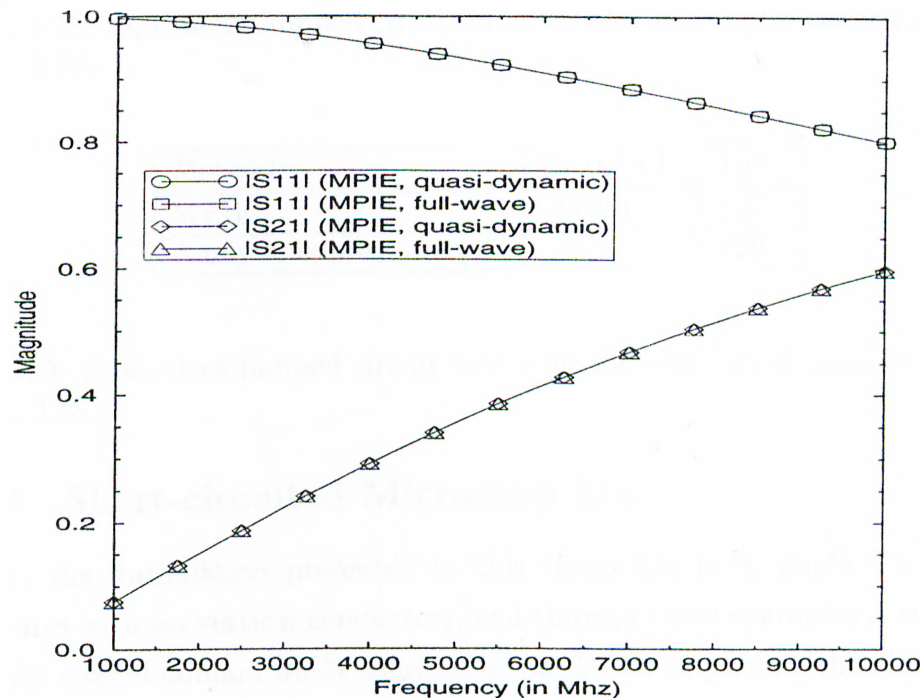


Figure 3.31: Magnitudes of  $S_{11}$  and  $S_{21}$  of the MIC capacitor shown in Fig. 3.28.

The lumped circuit model parameters of the interdigital capacitor given in Fig. 3.32 can be also extracted using the same procedure as in the microstrip corner. The series resistance in the model accounts for the metalization losses and is assumed to be zero in the parameter extraction process. For comparison purposes, the element values of the lumped circuit model for the interdigital capacitor are calculated from semi-analytical expressions [49], and it is observed that the extracted and calculated circuit element values for the capacitance  $C_2$  are very close to each other, see Table 3.3.



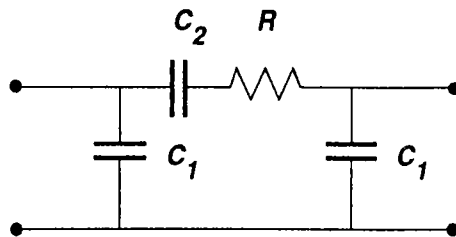


Figure 3.32: Equivalent lumped circuit model of the interdigital capacitor shown in Fig. 3.28.

Method	$C_1$ (pF)	$C_2$ (pF)
MPIE	0.0381	0.127
Analytic expressions [49]	N/A	0.120

Table 3.3: Equivalent lumped circuit values for the interdigital capacitor shown in Fig. 3.28.

### 3.3.9 Short-circuited Microstrip Line

So far, the formulation presented in this thesis has been applied to planar structures with no vertical conductors, and through these examples it is verified that the spatial-domain MoM solution of the MPIE employing the closed-form Green's functions gives accurate results for such structures. The next step is to apply the algorithm to planar structures with vertical metalizations.

In this example, a simple microstrip line short-circuited with a shorting pin, Fig. 3.33, is considered, where the shorting pin is modeled as a narrow rectangular strip placed between the microstrip line and the ground plane. Note that the same model is also used in the *em* simulation for the purpose of comparison. However, it should be stated that a more realistic shorting-pin can be modeled by placing the vertical strips in a form of rectangular cylinder both in *em* and in this approach. The dielectric constant of the substrate is chosen to be 4.0, and two different values of the substrate thickness are used in the analysis, 8 and 80 mils. The microstrip line is excited with a current source from the left end,

and is left open-circuited at the right end. To simulate the unity current-source excitation in  $em$ , the values of the voltage source and the input impedance are selected equal and very large with respect to the characteristic impedance of the line, which is the Norton equivalent of the current source with unity amplitude. The current distribution on the microstrip line is obtained and given in Figs. 3.34, and 3.35 along with the results obtained from the  $em$  software, denoted by Sonnet in the figures.

As can be seen from the figures, the results agree very well for a thin substrate case but, as the substrate thickness increases the result of  $em$  starts to deviate because  $em$  version 3.0 assumes constant current distributions on the vertical connections [31]. Note that we have employed three shorting pins for the thick substrate case to demonstrate the use of the formulation for multiple vertical metalizations, Fig. 3.35.

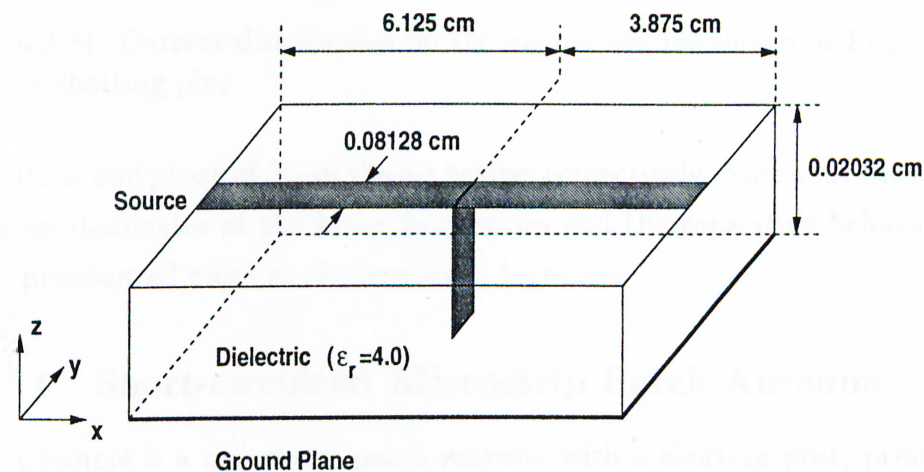


Figure 3.33: Geometry of a short-circuited microstrip line.

### 3.3.10 Air Bridge

Air-bridges are commonly used in MICs to carry signal paths over other signal paths, as in the case of a series connected spiral inductor. In this example, an air-bridge, which is shown in Fig. 3.36, is analyzed. Figures 3.37 and 3.38 show the

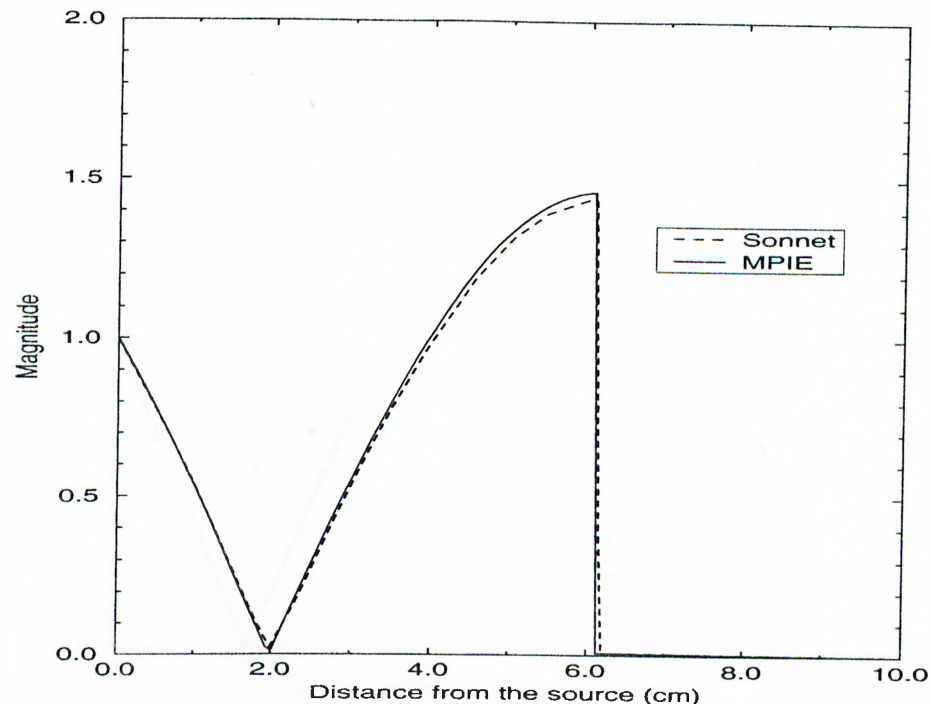


Figure 3.34: Current distribution on the microstrip line shown in Fig. 3.33 with a single shorting pin.

magnitude and phase of  $S_{11}$  of the air bridge, respectively. Note that the inductive behavior dominates at the lower frequencies and the capacitive behavior starts to be pronounced more as the frequency increases.

### 3.3.11 Short-circuited Microstrip Patch Antenna

Next example is a microstrip patch antenna with a shorting post, printed on a substrate with the thickness of 0.152 cm. and with the relative permittivity of 2.43, as shown in Fig. 3.39. Placing shorting posts in a microstrip patch antenna shifts the resonant frequency of the antenna without effecting the radiation pattern significantly [48, 64, 65]. Therefore, it can be employed in the design of a dual-frequency microstrip antenna. Moreover, if these shorting posts are made of PIN or varactor diodes, a frequency-agile antenna is obtained by electrically activating the diodes. In this example, the amount of frequency shift in the resonant frequency of a patch antenna is assessed, and demonstrated for several

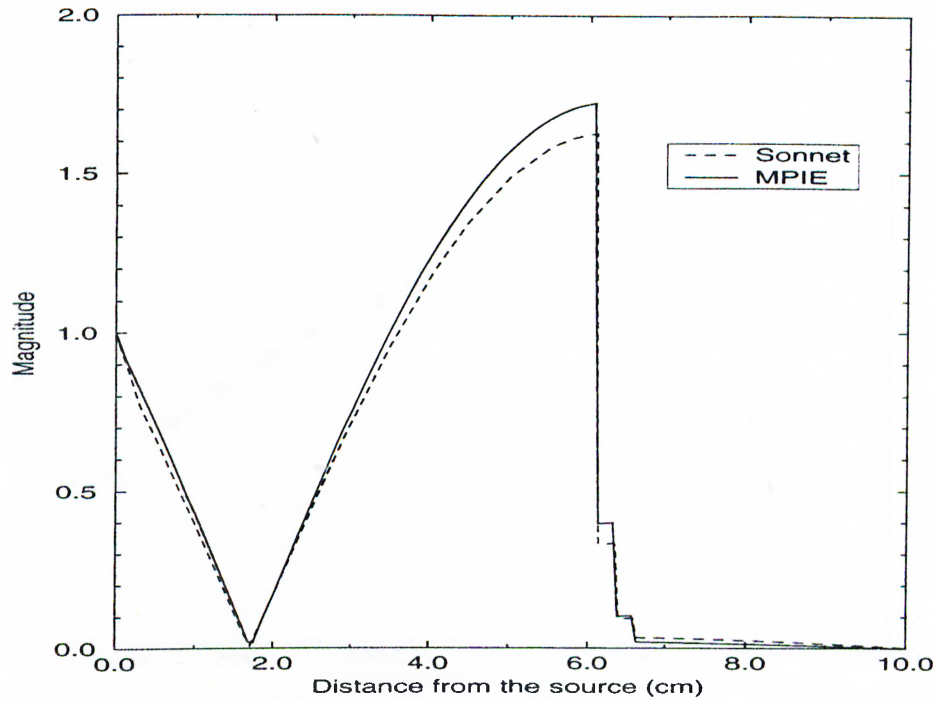


Figure 3.35: Current distribution on the microstrip line shown in shown in Fig. 3.33 with three shorting pins.

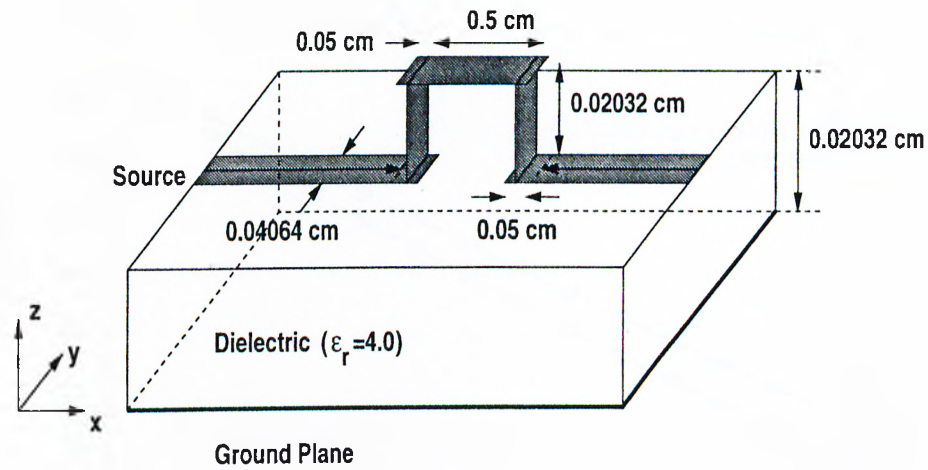
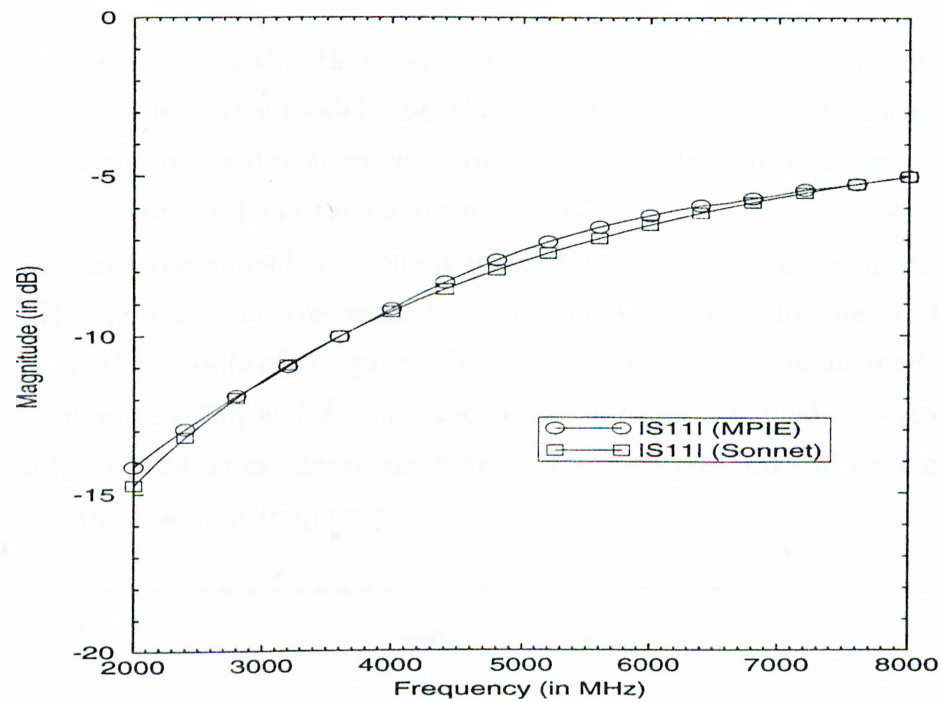
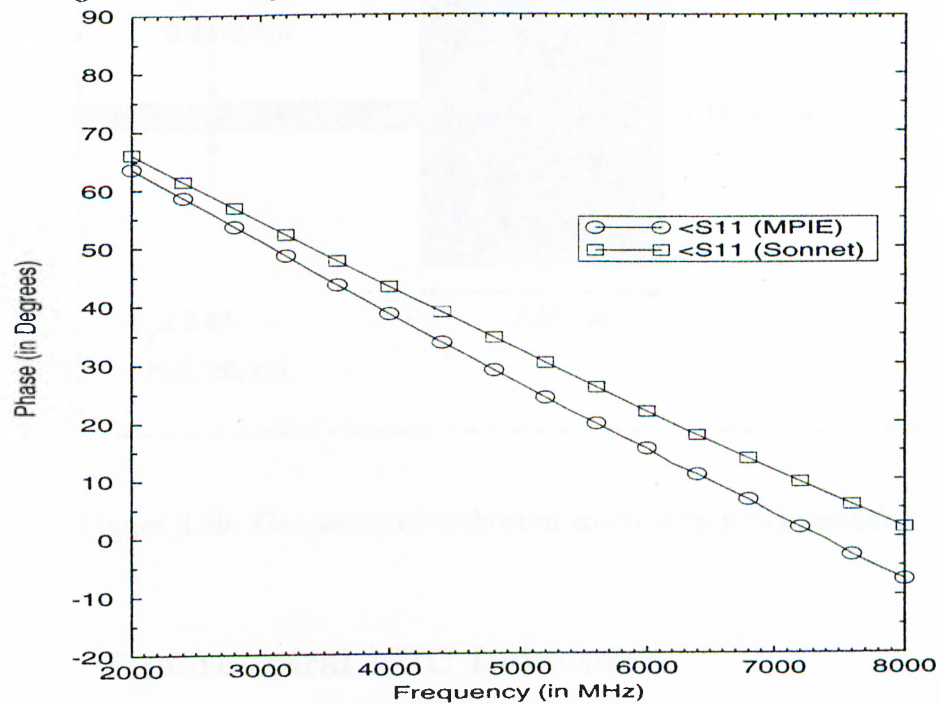


Figure 3.36: Geometry of an air bridge.

positions of the shorting post in Fig. 3.40, where the normalized position of the shorting post is defined as  $x_n = (x - 3.81)/3.81$ . The results obtained by the

Figure 3.37: Magnitude of  $S_{11}$  of the air bridge shown in Fig. 3.36.Figure 3.38: Phase of  $S_{11}$  of the air bridge shown in Fig. 3.36.

method presented in this thesis are compared to those measured and to those obtained by the cavity model, and the agreement is quite well considering the different types of feeding structures, microstrip-line feed for our case and probe feed for experimental and the cavity model [65].

Note that the unloaded resonant frequency of the antenna is approximately 1237 MHz, and it also corresponds to the resonant frequency for the shorting post located at the middle of the patch. This is because the dominant modes in this patch antenna,  $TM_{01}$  and  $TM_{10}$ , have almost zero electric field in z-direction at the middle of the patch, hence shorting post at this position will have negligible effect on the resonant frequency.

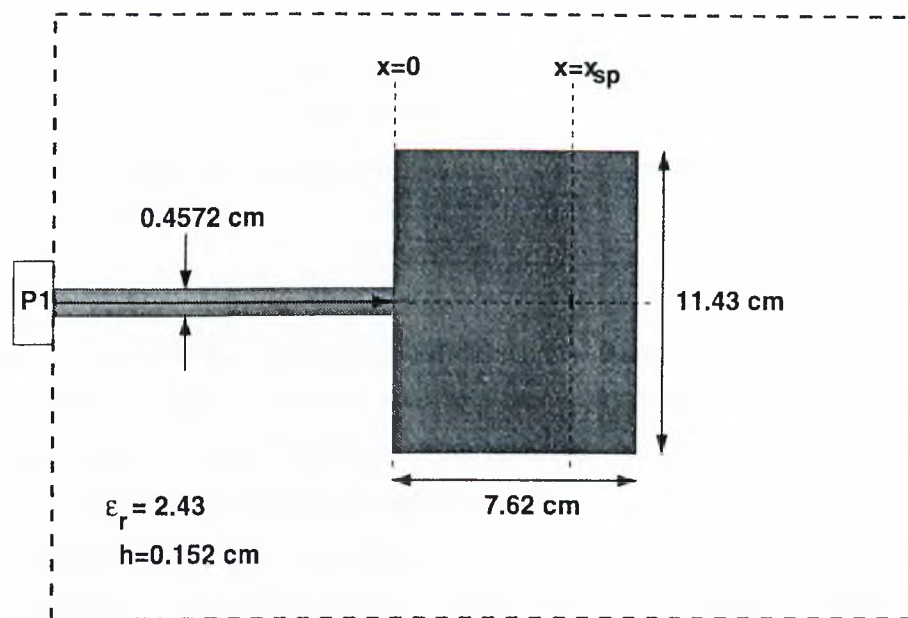


Figure 3.39: Geometry of a shorted microstrip patch antenna.

### 3.3.12 Square-spiral MIC Inductor

Finally, a square-spiral MIC inductor terminated in a short circuit, shown in Fig. 3.41, printed on a substrate with a thickness of  $100 \mu\text{M}$  and with the dielectric constant of 12.9, is analyzed. The magnitude and the phase of the input



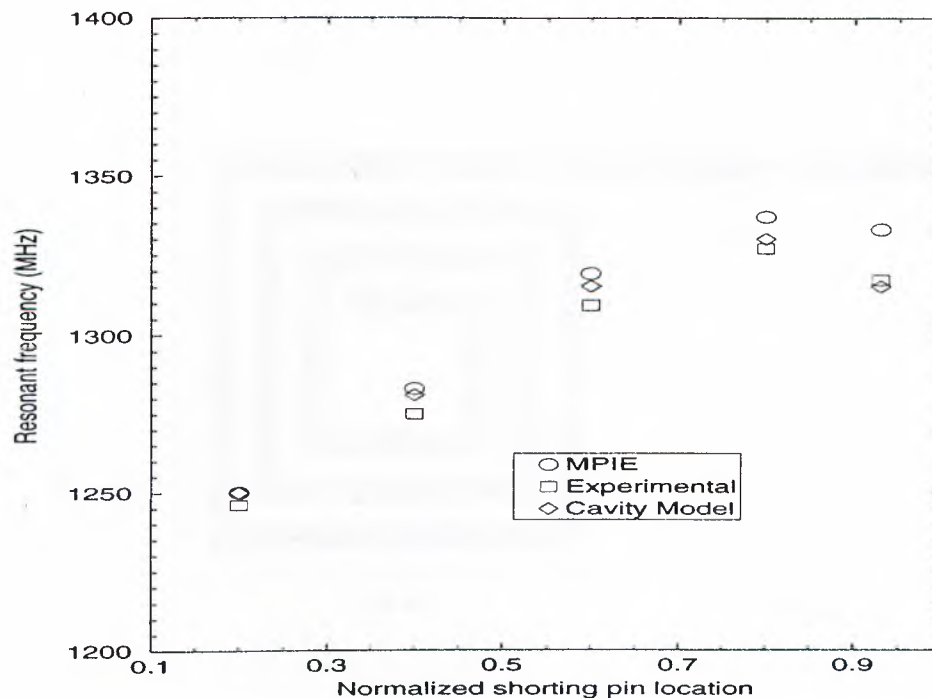


Figure 3.40: Resonant frequency of the patch antenna, shown in Fig. 3.39, vs. shorting pin location.

impedance, seen from the reference plane, are calculated and the magnitude is plotted in Fig. 3.42 as a function of frequency, the phase is equal to  $90^\circ$  throughout the frequency range. It is observed that the magnitude of the input impedance deviates from the ideal behavior of an inductor, as the frequency is increased, because of the self-resonance of the structure.

It should be noted that the model we have employed for the vertical metalizations, namely planar strip, is not the most accurate one. One can instead use circular cylindrical or square cylindrical via models within this formulation. But, since the main goal of this thesis is to demonstrate the use of the closed-form Green's functions in conjunction with the MoM for geometries with vertical metalizations, the simplest model is employed to convey the ideas clearly.

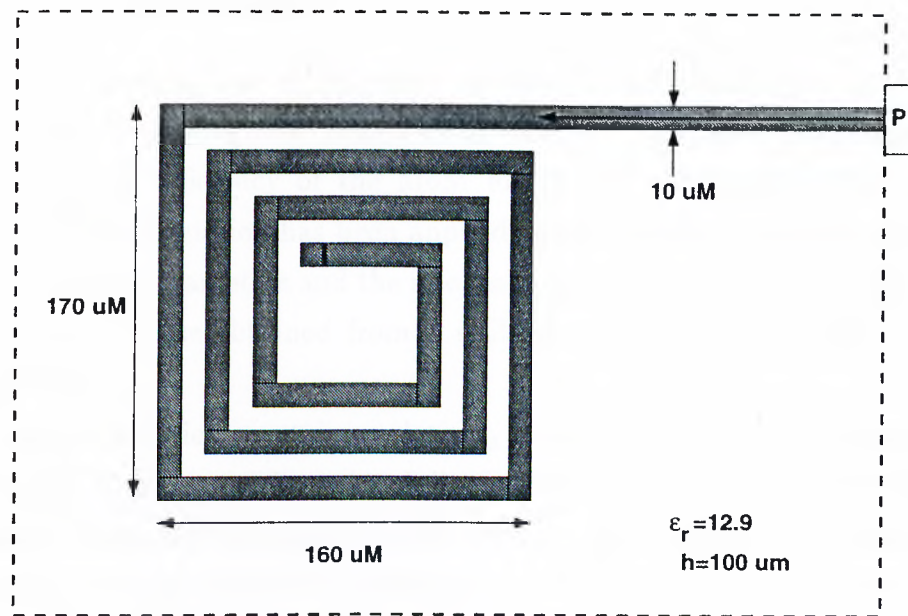


Figure 3.41: Geometry of a MIC square-spiral inductor.

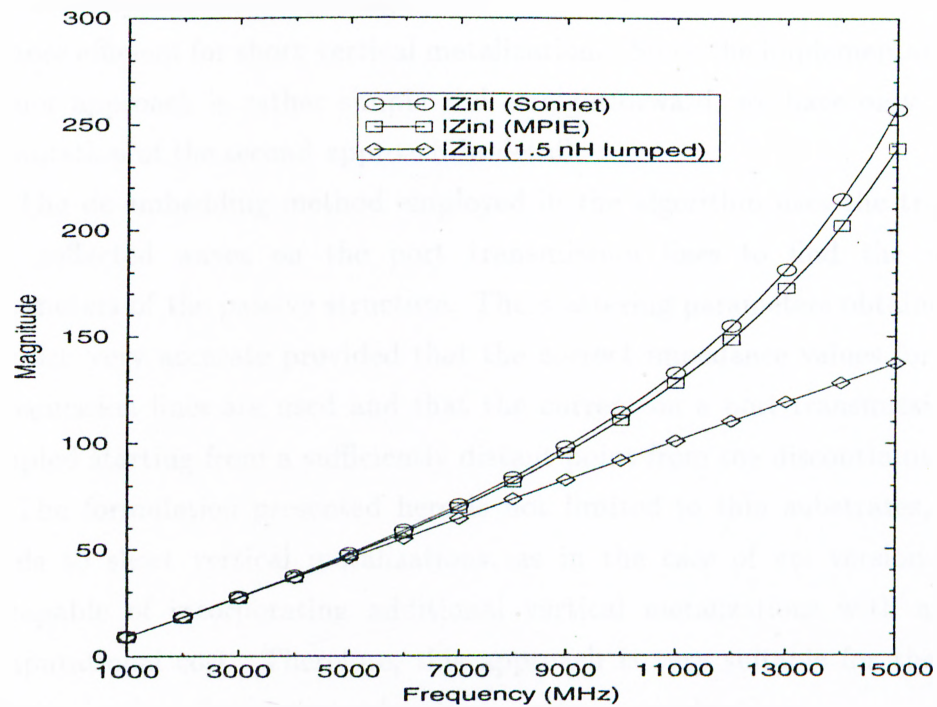


Figure 3.42: Magnitude of the input impedance of the MIC inductor shown in Fig. 3.41.



### 3.4 Conclusions

In this chapter, it was shown that the spatial domain analysis of the printed structures employing the closed-form Green's functions has improved the computational efficiency of the MoM for the planar geometries in multilayer media. The formulation has been applied to some realistic geometries, for which the scattering parameters and the relevant circuit parameters were extracted and compared to those obtained from a well-known commercial software, *em* from SONNET.

The formulation contains relatively less abstraction and gives accurate results for both microstrip and stripline structures with horizontal metalizations. However, there have been some difficulties in the use of these closed-form Green's functions for the analysis of geometries with vertical metalizations. In this chapter, these difficulties have been discussed and their remedies have been proposed. It is observed that one of these techniques is more efficient for long vertical metalizations requiring several basis functions, and the other approach is more efficient for short vertical metalizations. Since the implementation of the former approach is rather simple and straightforward, we have only given the formulation of the second approach in detail.

The de-embedding method employed in the algorithm uses the transmitted and reflected waves on the port transmission lines to find the scattering parameters of the passive structure. The scattering parameters obtained in this way are very accurate provided that the correct impedance values for the port transmission lines are used and that the current on a port transmission line is sampled starting from a sufficiently distant point from the discontinuity.

The formulation presented here is not limited to thin substrates, in other words to short vertical metalizations, as in the case of *em* version 3.0, and is capable of incorporating additional vertical metalizations with almost no computational cost. Therefore, this approach is very suitable for the purpose of optimization of a geometry involving vertical metalizations.

## Chapter 4

# Methods for Improving the Analysis Time

Development of a computationally efficient and rigorous technique has been the main focus of researchers in computational electromagnetics for a long time. In Chapter 3, we have proposed a technique based on the spatial-domain MoM in conjunction with the closed-form Green's functions, and have tested for its accuracy and robustness, but not for its computational efficiency. In this chapter, the computational efficiency of the technique is assessed from the CPU time analysis and some improvements in this context are proposed and tested.

The computational efficiency of a numerical technique can be assessed either by the complexity analysis of the technique or by the CPU time consumed by the technique for a given number of unknowns. Since the general technique is quite complex and consists of three main algorithms, namely the computation of the closed-form Green's functions, evaluation of the MoM matrix entries and the solution of the linear systems of equations, it is difficult and may not be useful to find the computational complexity of the whole technique. Instead, the CPU time consumed by each algorithm of the technique is assessed independently. On the other hand, the main disadvantage of this approach is that the CPU times also heavily depend on the programming style and compilers, whereas, the computational complexity approach gives the cost of an algorithm independent

from the platform being used.

Among these three algorithms, the evaluation of the MoM matrix entries is the one that consumes most of the CPU time of the technique for moderate size geometries (spanning a few wavelengths). However, for large geometries requiring large number of unknowns, the solution time of the linear system of equations dominates the total analysis time. It should be noted that the computation of the closed-form Green's functions does not contribute significantly to the total solution time unless vertical or multilayer metalizations are used. To give an idea, the CPU times for some printed geometries analyzed in Chapter 3 are given in Table 4.1. Note that all the geometries referred to in the table have been analyzed with uniform segmentation, which gives rise to block symmetric MoM impedance matrices. Therefore, the matrix fill-time has been reduced significantly by exploiting the symmetry in the matrix. It is observed from Table 4.1 that although the number of unknowns in the analysis of the interdigital MIC capacitor is less than that of the band-pass filter, the matrix fill-time of the capacitor is greater than the matrix fill-time of the filter. This is due to the fact that the dimensions of the MIC capacitor are relatively small as compared to the guided wavelength and therefore the accelerated evaluation of the reaction integrals, which will be explained in detail in the next sections, cannot be employed for the same approximation parameters. Another point that is worth mentioning is the number of exponentials used to approximate the spatial-domain Green's functions. Depending on the geometry and frequency, one can reduce the matrix fill-time by using less number of exponentials while preserving the accuracy in the results. Finally, the benchmarks shown in Table 4.1 do not show the ultimate limits of the algorithm, the CPU times can be reduced further by optimizing the code.

Since the matrix fill-time is the major contributor to the total CPU time consumed by the analysis in most cases, special care has been taken for filling up the impedance matrix, which is mainly the calculation of the reaction integrals. These integrals can be evaluated efficiently by following the steps given below:

- A look-up table is prepared to store the indices of similar inner-products

Geometry	# of unknowns	Analysis frequency (MHz)	Green's function evaluation time	Matrix fill-time	Solution time
Patch antenna (Fig. 3.6)	454	2300	6	8	34
Multi-layer band-pass filter (Fig. 3.25)	862	4000	18	44	315
Band-pass filter (Fig. 3.19)	1638	2550	6	94	2122
Interdigital MIC capacitor (Fig. 3.28)	576	1000	6	262	80

Table 4.1: CPU times in terms of seconds consumed in the analysis of some typical geometries on a SUN SPARC 20 workstation.

and every new inner-product term is searched from the table to prevent re-calculation.

- The result of an inner-product is set to zero automatically if the distance between the source and observation points is greater than the predetermined value  $\rho_{max}$ . The value of  $\rho_{max}$  is uniquely defined for every Green's function.
- The method for the approximation of the Green's function is dynamically changed according to the distance between the source and observation points.

The last two items are explained in Section 4.1 in detail. In addition to the efficient evaluation of the MoM matrix entries, the total CPU time required for the characterization of a circuit over a frequency band can be further reduced by using frequency interpolation, which is explained in Section 4.2.

## 4.1 Evaluation of the MoM Matrix Entries

Despite the time-saving realized from the analytical evaluation of the reaction integrals, the need for further reducing the matrix fill-time is not obviated for many problems. With this background in mind, the objective of this section is to present a hybrid technique for the evaluation of the MoM reaction integrals in a numerically-efficient manner, which further reduces the CPU time needed for their computation.

Efficient evaluation of the MoM matrix entries, given in Eqs. (3.9)-(3.17), is an important issue that deserves further study, because it is the principal contributor to the total CPU time for small and moderate-size geometries. The MoM matrix entries can be calculated analytically without any numerical integration for piecewise continuous basis and testing functions via the rigorous approach described in [17, 66], provided the closed form Green's functions are used for the formulation. In this method, each of the exponentials in Eq. (2.63) is replaced by its Taylor series approximation as follows:

$$G^{A,q} \cong \sum_{n=1}^N a_n \sum_{m=0}^M c_m \frac{(r_n - r_c)^m}{r_n} \quad (4.1)$$

where  $c_m$ 's are the Taylor series coefficients and  $r_c$  is the center of expansion for the exponential term  $e^{-jk_z r_n}$ . Alternatively, one could replace the entire Green's function in Eq. (2.63) with a suitable approximation that would enable the reaction integrals to be evaluated analytically. For instance, one may use the polynomial approximation for the Green's function as

$$G^{A,q} \cong \sum_{l=-1}^L b_l \cdot \rho^l \quad (4.2)$$

where  $b_l$ 's are the complex coefficients obtained from a least-squares fitting scheme. It is obvious that the analytical integration of the reaction integrals is considerably simpler for the Green's functions expressed in Eq. (4.2), than for those expressed in Eq. (4.1). This is because the analytical evaluation of the inner-product integrals using the former representation requires extensive complex arithmetic operations, as well as multiple evaluations of complex logarithms and

trigonometric functions. However, the caveat in the polynomial-fitting approach is that approximating the Green's function over the entire range is very difficult, if not impossible, with a relatively small  $L$ , because of the singular behavior of the Green's functions as  $\rho \rightarrow 0$ . One approach to resolving this dilemma is to utilize both of the above representations, but in complementary regions, thereby taking the advantage of the salient features of both. This can be done by using Eq. (4.1) to represent the Green's function for small  $\rho$ , where it exhibits a singular behavior, and then switch over to Eq. (4.2) as  $\rho$  becomes larger.

To summarize, the direct application of the rigorous method places an unnecessary computational burden when  $\rho$ , the distance between the source and observation points, is greater than a predetermined value  $\rho_{ls} = \sqrt{\frac{10^s}{k_0}}$ , where  $s$  is a constant. To circumvent this problem, one can use a hybrid approach, whose algorithm is given as a flowchart in Fig. 4.1, which uses a judicious combination of the two methods to increase the computational speed with which the MoM matrix entries are generated. At this point, it is worthwhile to describe the strategy for employing the hybrid technique. To use a small  $L$  in Eq. (4.2), the polynomial-fitting algorithm should be performed over a small range of  $\rho$ , which requires the least-squares fitting with  $N_{ls}$  sampling points to be repeated for each of the inner-product operations. Consequently, to accelerate the fitting process, the Green's function is sampled between  $\rho_{ls}$  and  $\rho_{max}$ , and the sampled values are stored in a look-up table before starting to fill-up the MoM matrix. These tabulated values can be subsequently interpolated to perform the least-squares fitting relatively fast for each inner-product operation. Here, one can use linear or quadratic interpolation scheme to find required values for the least-squares approximation process, from the previously sampled values of the Green's function.

#### 4.1.1 Numerical Examples

As a first example, the microstrip patch antenna, shown in Fig. 3.6, is analyzed to demonstrate the efficiency and accuracy of the hybrid method. The effects of the choice of  $\rho_{ls}$  on the matrix fill-time and on the accuracy of the results

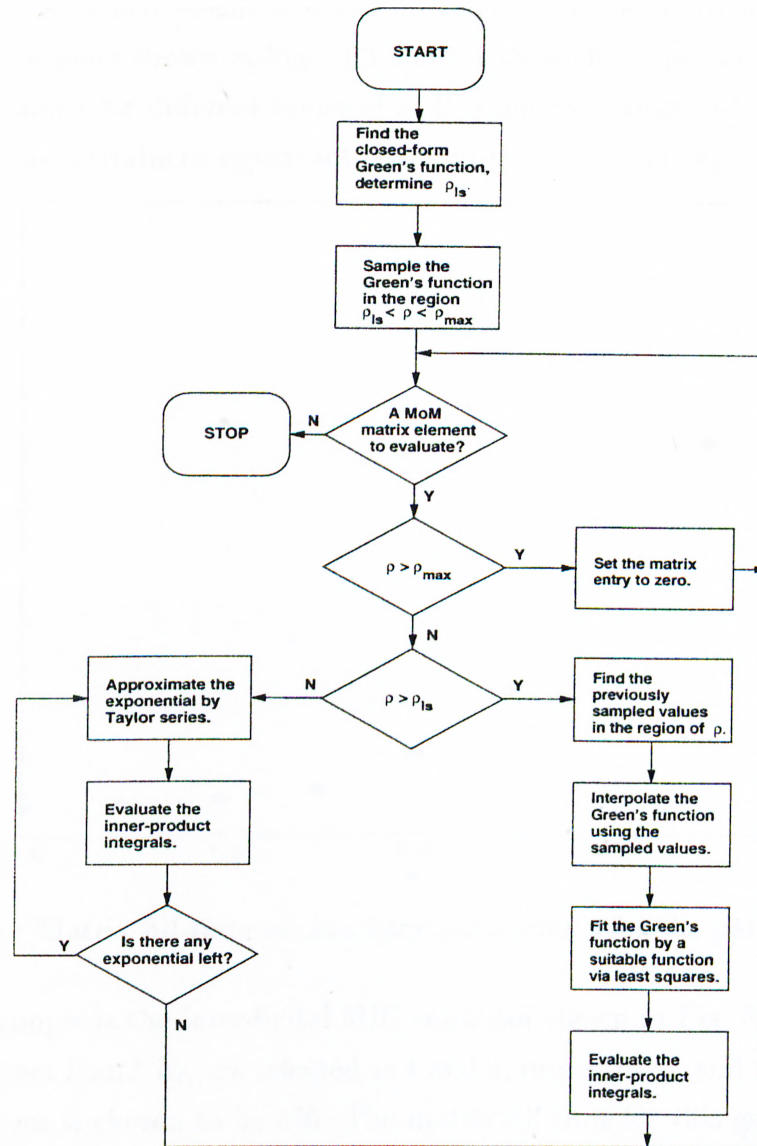


Figure 4.1: Flow-chart of the hybrid method for evaluating the MoM matrix entries.

are investigated for the parameters  $L$  and  $N_{ls}$ , selected as 4 and 9, respectively. The number of basis functions for the patch antenna is chosen to be 537, and the CPU times are obtained for different values of the auxiliary parameter  $s$ , Fig. 4.2. Note that the rigorous method, which is used here as the reference, corresponds

to  $s = \rho_{ls} = \infty$  which means that the polynomial fitting is not used at all (see Fig. 4.1). The plots shown in Figs. 4.3 and 4.4 show the impedance of the patch antenna obtained for different values of  $s$ . It is observed that, reducing  $\rho_{ls}$  below a certain value introduces significant errors in the results as expected.

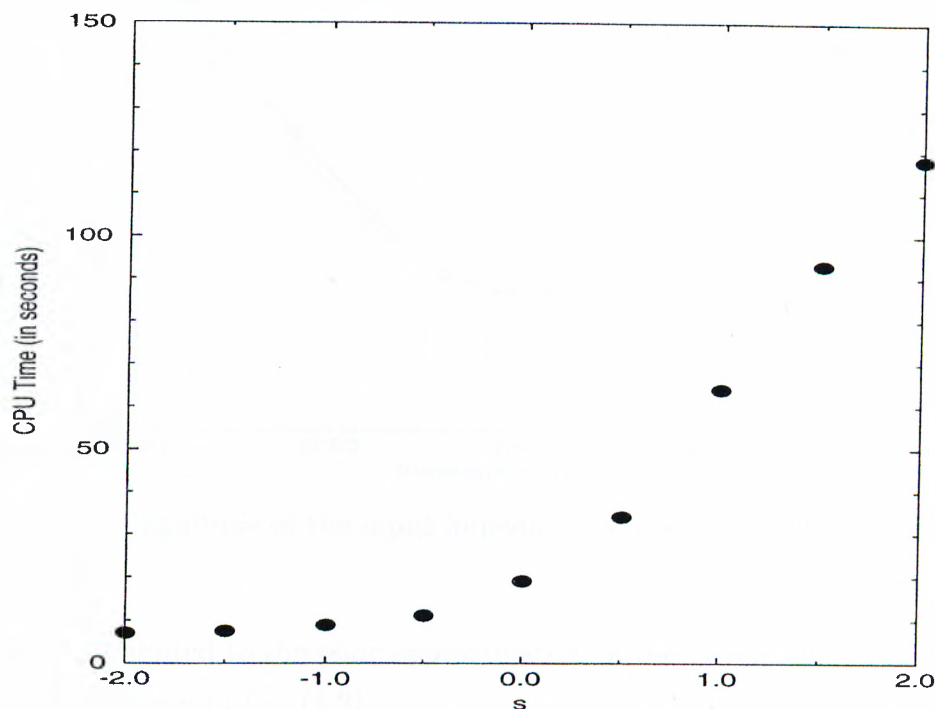


Figure 4.2: Matrix fill-time vs. auxiliary parameter  $s$  for the patch antenna.

Next example is the interdigital MIC capacitor shown in Fig. 3.28, for which the parameters  $L$  and  $N_{ls}$  are selected as 4 and 9, respectively, and the number of basis functions is chosen to be 576. The matrix fill-time for this geometry could also be reduced by changing the  $\rho_{ls}$  parameter as shown in Fig. 4.5. Since the capacitor is analyzed over a relatively wide frequency band as compared to the patch antenna, the mean CPU times are used instead of a single CPU time at the center frequency. This is because the matrix fill-time depends on the frequency:  $\rho_{ls}$  for a fixed  $s$  and the number of exponentials in the Green's function are different for different frequencies. The scattering parameters for different values of  $s$  are given in Figs. 4.6 and 4.7. Note that although the matrix fill-time is considerably reduced at  $s = -4.5$ , there are some artifacts on the results which



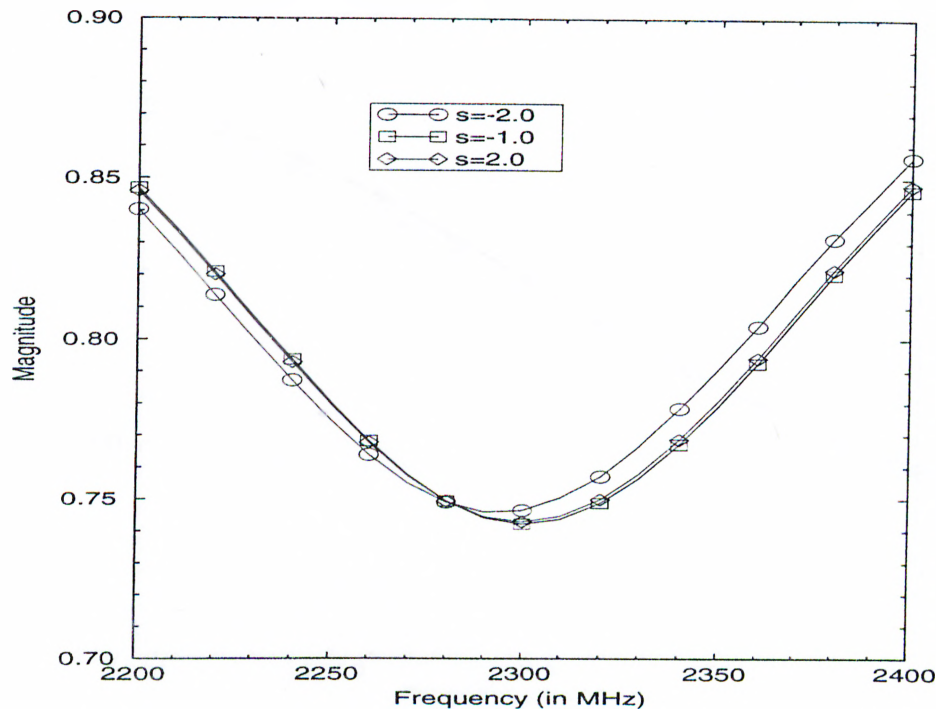


Figure 4.3: Magnitude of the input impedance of the patch antenna for different values of  $s$ .

could be attributed to the poor approximation of the Green's functions with the polynomials given in Eq. (4.2).

At this point a natural question arises: Is it possible to improve the results at  $s = -4.5$  by increasing the sampling points in the least-squares approximation, without increasing the computation time significantly? In order to answer this question, the number of sampling points,  $N_{ls}$ , is increased from 9 to 12, and the scattering parameters are calculated again for  $s = -4.5$  giving the results in Fig. 4.8. While there is a noticeable improvement in the results for  $f < 7500$  MHz, above this frequency point, there is still a slight deviation from the correct values. The reason for this behavior is that as the frequency increases, the Green's functions start to decay rapidly which increases the error in the least-squares approximation with the given order and the number of sampling points.

It should be re-emphasized here that the choice of  $s$  defines the distance  $\rho_{ls}$ , below which the Taylor series approximation Eq. (4.1) is employed and above which the polynomial approximation Eq. (4.2) over the domain of each

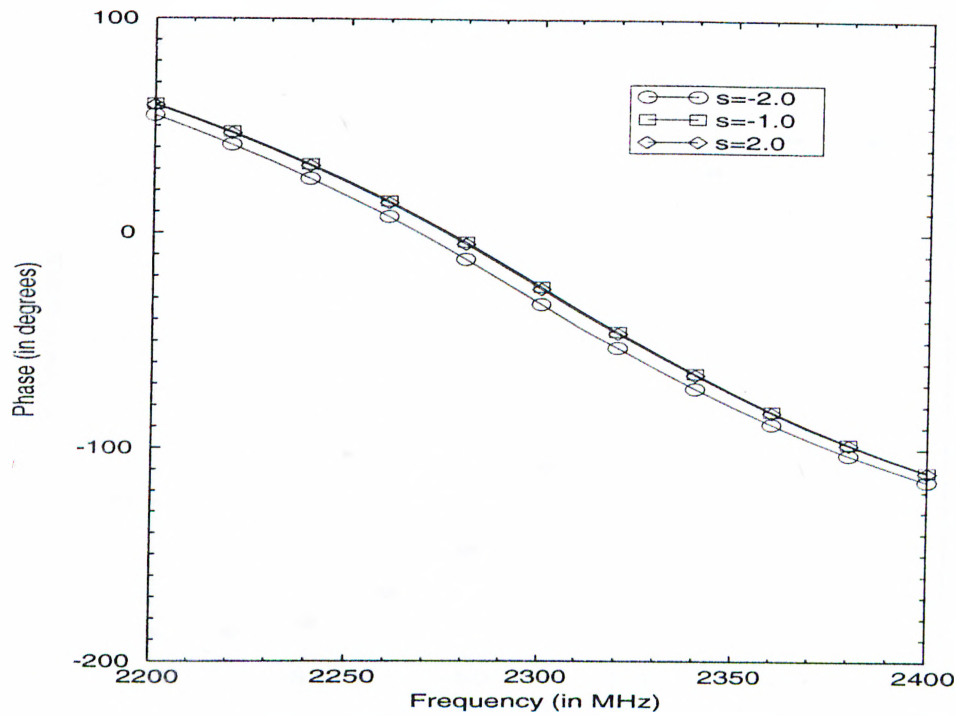


Figure 4.4: Phase of input impedance of the patch antenna for different values of  $s$ .

inner-product term is used. For distances greater than  $\rho_{ls}$  and less than  $\rho_{max}$ , the Green's function to be approximated was sampled and these values were stored in a look-up table. However, the sampled values of the Green's function over the domain of an inner-product term may not be sufficient to find the unknown coefficients of the polynomial approximation in the least-squares sense. To remedy this, instead of evaluating the Green's functions at additional intermediate points, a linear or quadratic interpolation is employed, using the previously calculated values of the Green's functions from the look-up table. So far, in the examples given in Figs.4.6 and 4.7, we have employed linear interpolation with 9 interpolation points, for which the results have shown some artifacts for  $s = -4.5$ . Although increasing the interpolation points from 9 to 12 in the least-squares linear interpolation has improved the results to a degree, they are still not acceptable, Fig. 4.8. But, switching to the quadratic interpolation from the linear interpolation gives a significant improvement even for smaller values of  $s$ , as shown in Fig. 4.9 for  $s = -6$ . Note that the

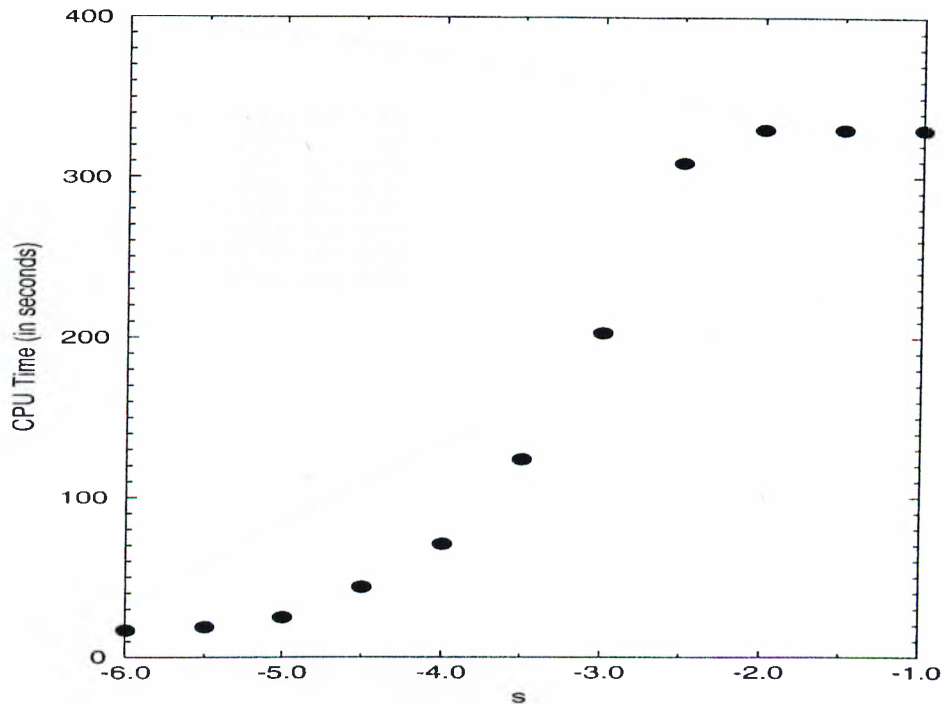


Figure 4.5: Mean matrix fill-time vs. auxiliary parameter  $s$  for the interdigital capacitor.

additional computational cost of increasing the sampling points to 12 and using the quadratic interpolation, is minor, while the CPU time gain is approximately 20 fold for this geometry.

It should also be stated that the CPU times given in Fig. 4.5 have been obtained without using the quasi-static approach which has been demonstrated in Section 3.3.8. If one uses the quasi-static approach (i.e. less number of exponentials in the unused portion of the Green's functions), then the mean matrix fill-times would be reduced further. However, note that the quasi-static approach only effects the inner-product evaluation time in the region of Eq. (4.1), it has no effect on the polynomial fitting scheme.

We conclude that the proposed hybrid method can reduce the matrix fill-time significantly, without sacrificing the accuracy, with an appropriate choice of  $\rho_{ls}$ ,  $N_{ls}$  and the interpolation scheme. In addition, we find that the proper choice of  $\rho_{ls}$  and  $N_{ls}$  depends on the Green's function, as well as on the cell size used for discretization, and that the choice of  $\rho_{max}$  should be based on the magnitude

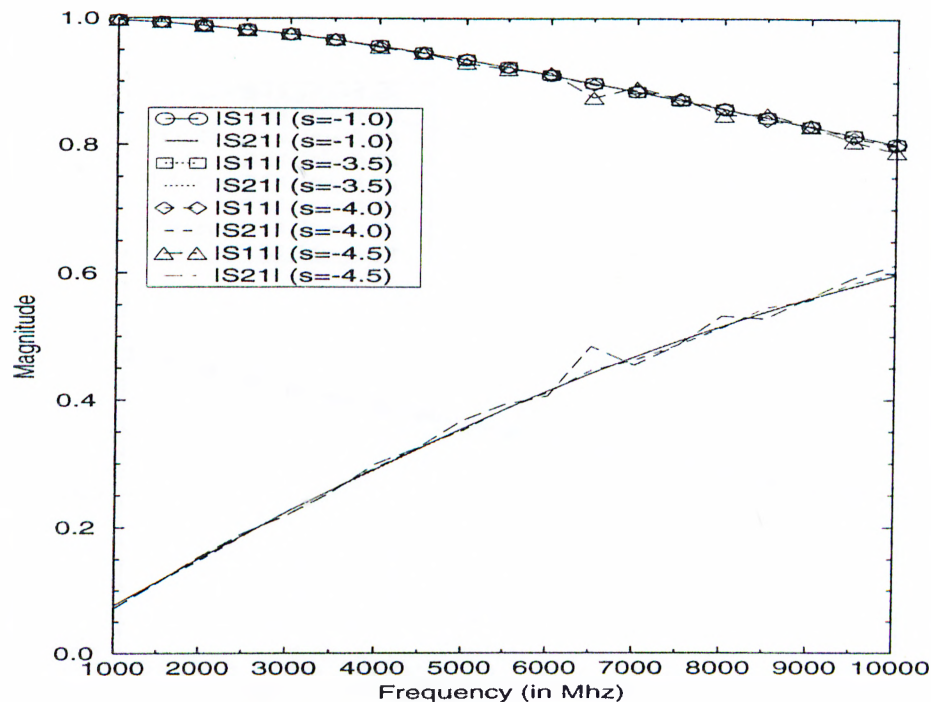


Figure 4.6: Magnitudes of  $S_{11}$  and  $S_{21}$  of the interdigital capacitor for different values of  $s$ .

of the Green's function at  $\rho_{max}$ . In order to obtain satisfactory results, one should use the quadratic interpolation scheme in the polynomial approximation step, which is employed to find additional sample points for the least-squares fitting. By considering these remarks, one can devise an adaptive algorithm to find the optimum value for  $s$ . Table 4.2 shows the CPU times obtained from the simulation software which uses an adaptive algorithm to find the optimum value for  $s$ . Since the values given in Table 4.1 are found for  $s = -1.0$ , which is an optimized value for the patch antenna only, using an adaptive algorithm also improves the CPU times for other geometries and frees the user from trying to find the optimum value of  $s$  in each application.

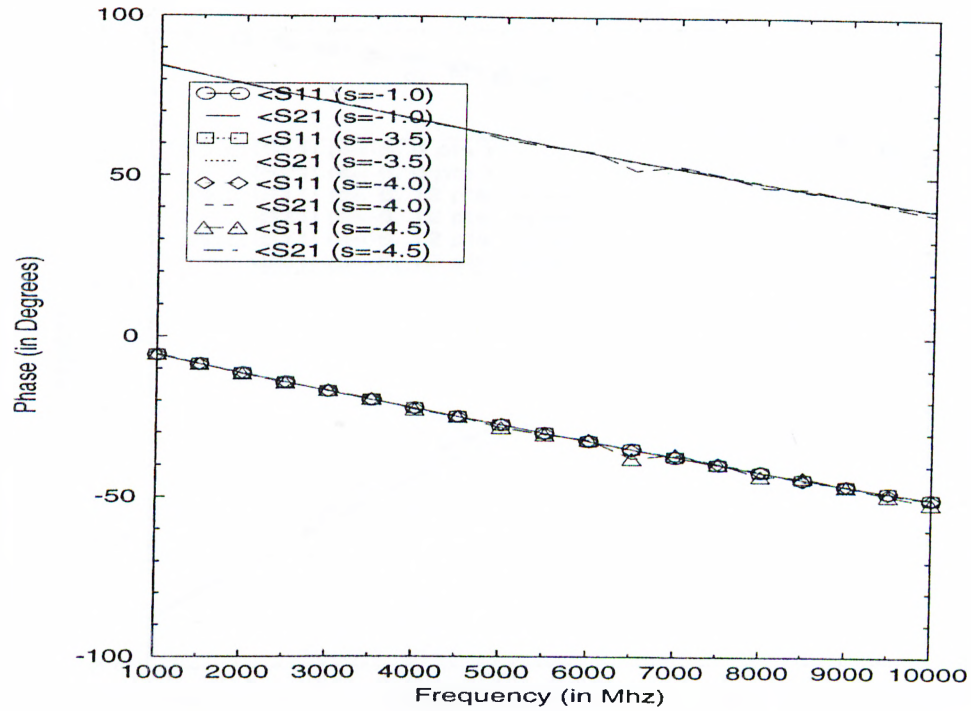


Figure 4.7: Phases of  $S_{11}$  and  $S_{21}$  of the interdigital capacitor for different values of  $s$ .

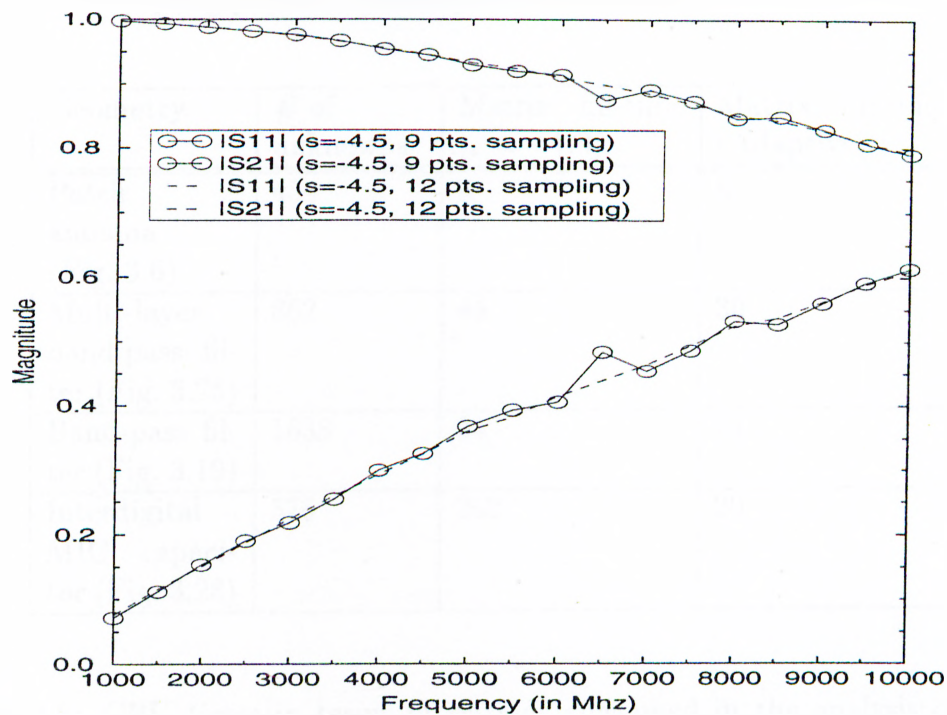


Figure 4.8: Magnitudes of  $S_{11}$  and  $S_{21}$  of the interdigital capacitor for different number of sampling points.



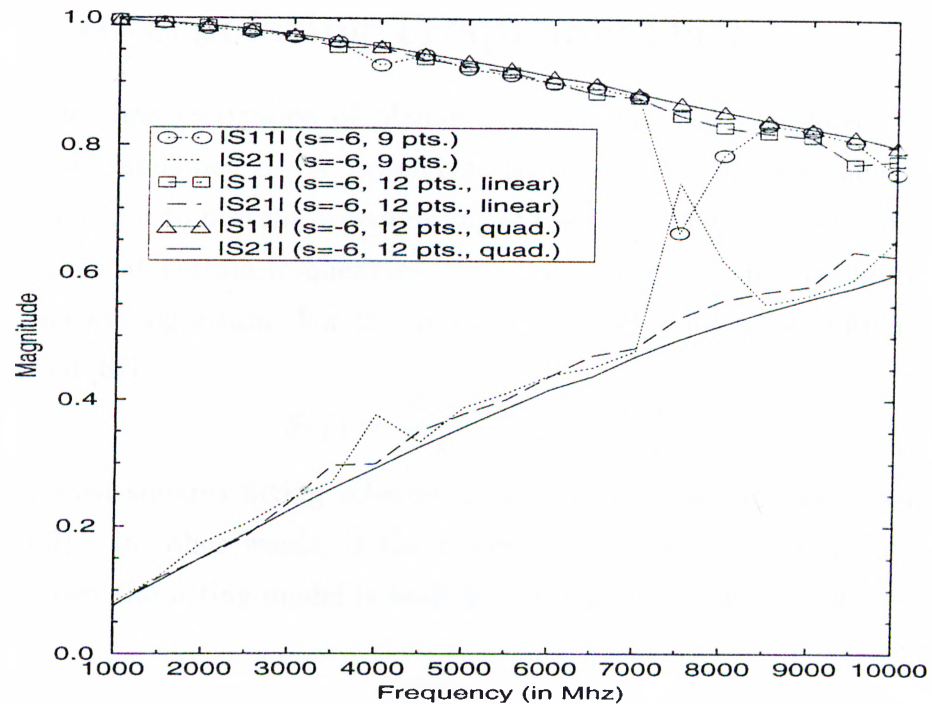


Figure 4.9: Magnitudes of  $S_{11}$  and  $S_{21}$  of the interdigital capacitor for different number of sampling points and interpolation scheme.

Geometry	# of unknowns	Matrix fill-time ( $s = -1.0$ )	Matrix fill-time (Adaptive)
Patch antenna (Fig. 3.6)	454	8	8
Multi-layer band-pass filter (Fig. 3.25)	862	44	30
Band-pass filter (Fig. 3.19)	1638	94	54
Interdigital MIC capacitor (Fig. 3.28)	576	262	20

Table 4.2: CPU times in terms of seconds consumed in the analysis of some typical geometries with adaptive  $s$  parameter selection on a SUN SPARC 20 workstation.

## 4.2 Interpolating Frequency Data

Since the characterization of planar circuits is usually performed over a given frequency band, one needs to analyze the circuit for many frequencies in this band. In order to prevent oversampling of the frequencies in the band, the circuit is analyzed at certain frequencies, then the overall response is obtained via an interpolation algorithm. For this purpose, the following rational fitting model is employed [67]:

$$S(f) = \frac{N_0 + N_1f + \cdots + N_nf^n}{1 + D_1f + \cdots + D_df^d} \quad (4.3)$$

and, a least-squares fitting scheme is used to find the unknown coefficients in Eq. (4.3). In other words, if the circuit is analyzed at  $L$  different frequency points then the fitting model is built by solving the following system:

$$\begin{bmatrix} S'(f_1)f_1 & S'(f_1)f_1^2 & \cdots & S'(f_1)f_1^d & -1 & -f_1 & \cdots & -f_1^n \\ S'(f_2)f_2 & S'(f_2)f_2^2 & \cdots & S'(f_2)f_2^d & -1 & -f_2 & \cdots & -f_2^n \\ \vdots & \vdots & \vdots & \vdots & \vdots & \vdots & \vdots & \vdots \\ S'(f_L)f_L & S'(f_L)f_L^2 & \cdots & S'(f_L)f_L^d & -1 & -f_L & \cdots & -f_L^n \end{bmatrix} \begin{bmatrix} D_1 \\ D_2 \\ \vdots \\ D_d \\ N_0 \\ N_1 \\ \vdots \\ N_n \end{bmatrix} = \begin{bmatrix} -S'(f_1) \\ -S'(f_2) \\ \vdots \\ -S'(f_L) \end{bmatrix} \quad (4.4)$$

where  $S'(f)$  represents the exact circuit response at frequency  $f$  obtained from the simulation. After having found the unknown coefficients, they can be substituted into Eq. (4.3) to find the circuit response at any frequency in the band of approximation. Note that a different  $S(f)$  with different coefficients are used for each S-parameter.

In order to model the whole frequency response with minimum error and with a minimum number of sampling frequencies at which the analysis is performed, the frequency sample points should be selected adaptively. The frequency sample points, which are going to be used in the least-squares fitting process, can be selected according to the flow-chart shown in Fig. 4.10. Moreover, the orders of

the polynomials in the numerator and denominator should not be selected too large to avoid spurious oscillations in the frequency response of the circuit.

Another technique, which can be used in frequency interpolation, is the Hilbert transform approach. It is well known that Hilbert transform relates the real and imaginary parts of the transfer function of a causal system, which then can be used to interpolate the frequency domain response of passive microwave printed circuits [68].

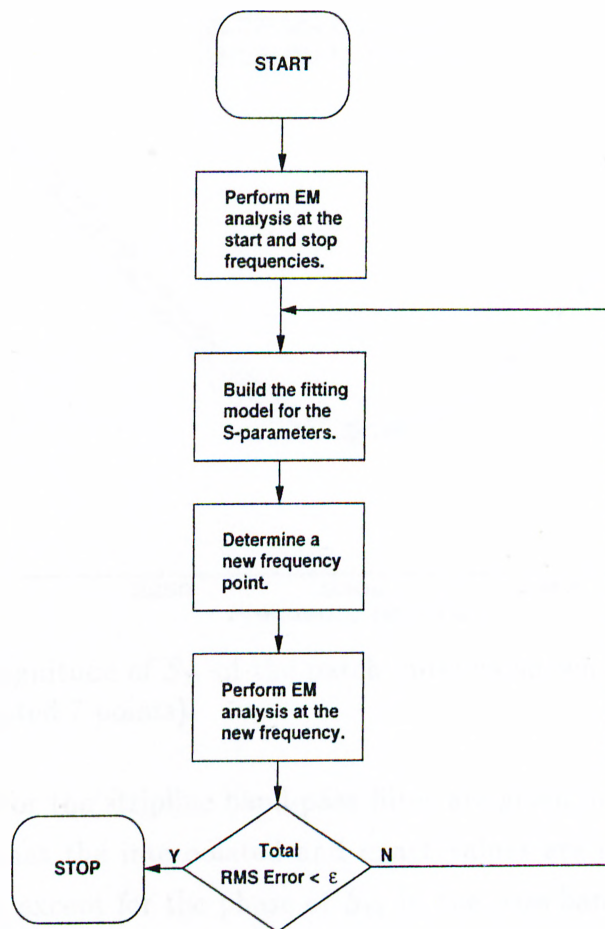


Figure 4.10: Flow-chart of the frequency interpolation.



### 4.2.1 Numerical Examples

To demonstrate the frequency interpolation algorithm, the microstrip patch antenna given in Fig. 3.6, and the stripline band-pass filter given in Fig. 3.25 are analyzed. Since the frequency response of the patch antenna is relatively smooth, small number of frequency points was sufficient to interpolate the response, as shown in Figs. 4.11 and 4.12.

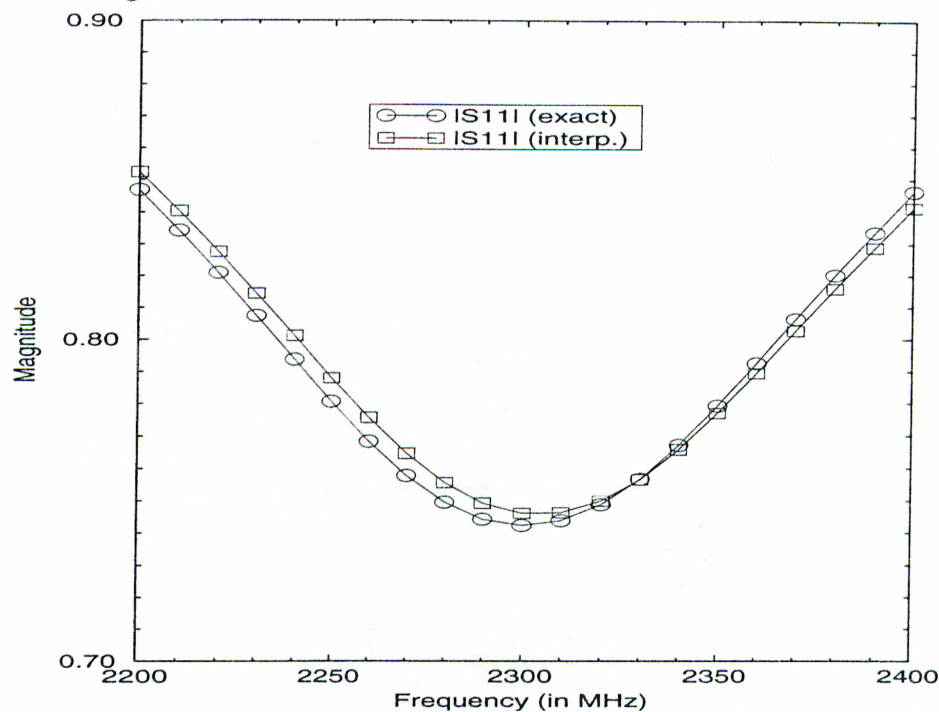


Figure 4.11: Magnitude of  $S_{11}$  of the patch antenna shown in Fig. 3.6 (exact:21 points, interpolated:7 points).

The results for the stripline band-pass filter are given in Figs. 4.13 and 4.14. It is observed that the interpolated and exact values are in a good agreement with each other except for the phase of  $S_{11}$  in the pass-band. It should also be noted that the interpolation process correctly estimates the magnitude dip for  $S_{11}$  in the pass-band. Therefore, the CPU time for the analysis of the circuit over a band of frequency can be reduced significantly about 2-3 folds by using the frequency interpolation, and the accuracy of the results can be improved by increasing the number of sampling points,  $L$ .

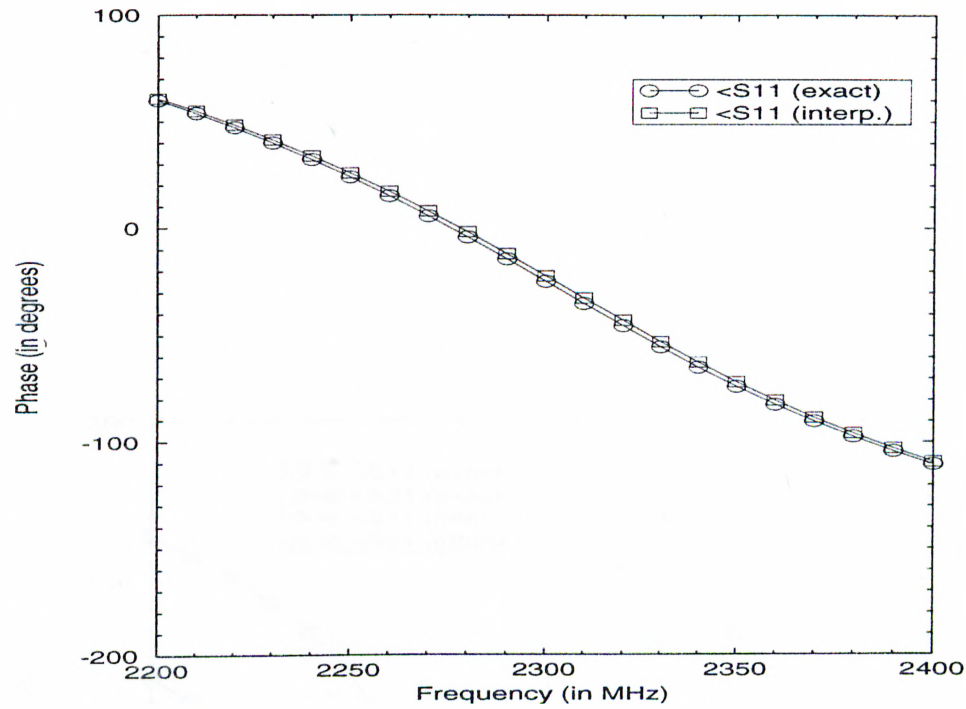


Figure 4.12: Phase of  $S_{11}$  of the patch antenna shown in Fig. 3.6 (exact:21 points, interpolated:7 points).

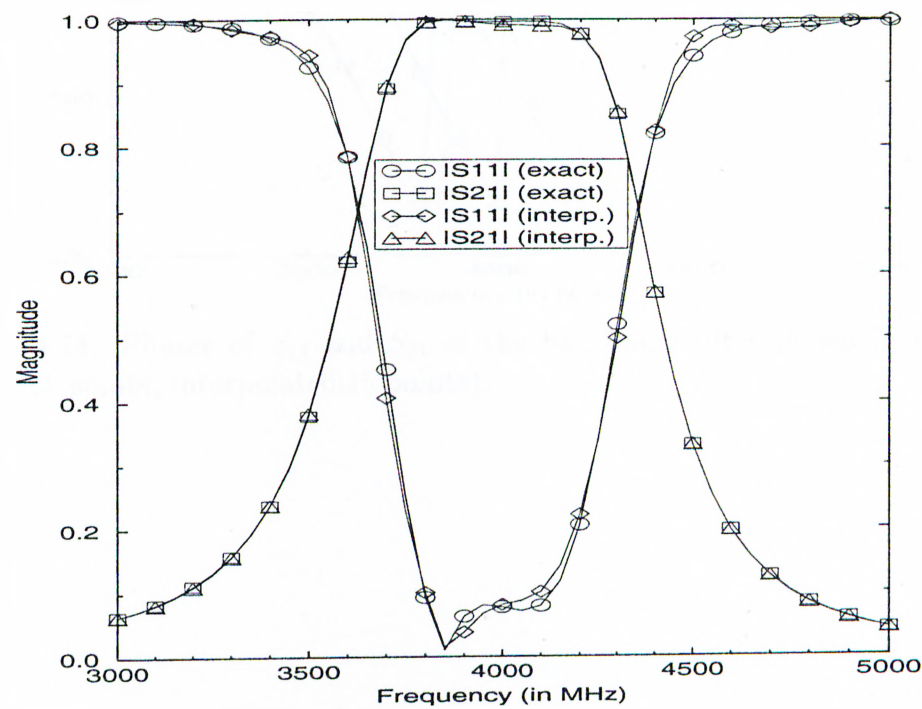


Figure 4.13: Magnitudes of  $S_{11}$  and  $S_{21}$  of the band-pass filter shown in Fig. 3.25 (exact:41 points, interpolated:15 points).

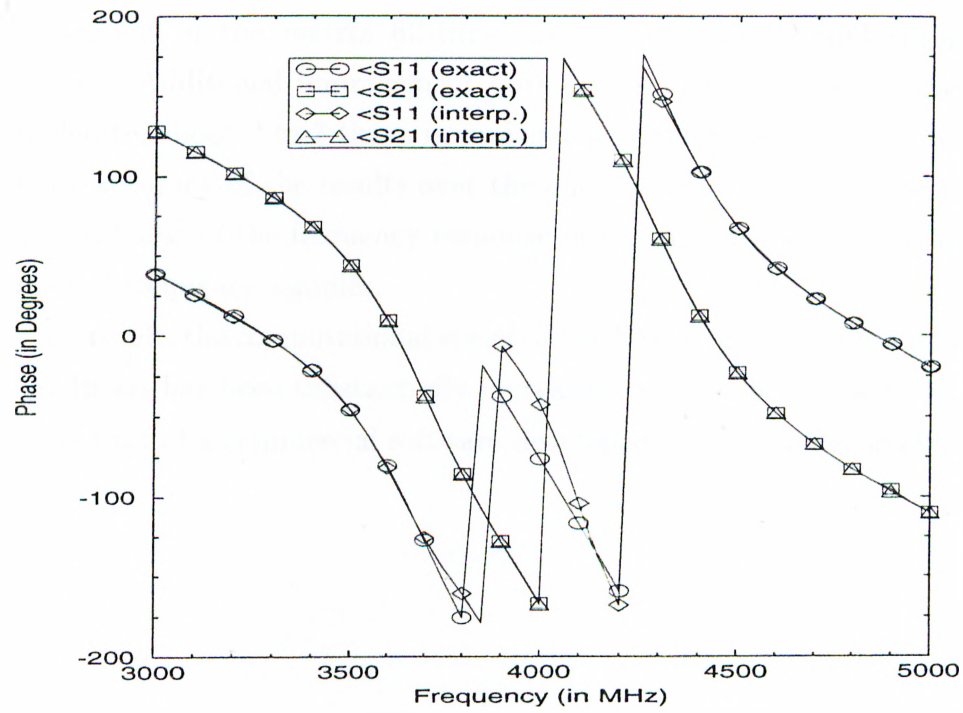


Figure 4.14: Phases of  $S_{11}$  and  $S_{21}$  of the band-pass filter shown in Fig. 3.25 (exact:41 points, interpolated:15 points).

### 4.3 Conclusions

In this chapter, two different methods were introduced to reduce the total analysis time requirement in the MoM. The first method, which is for the evaluation of the reaction integrals, greatly improves the matrix fill-time, while the second one uses the frequency interpolation algorithm to improve the total characterization time over a band of frequency.

By using the former approach, one can easily achieve 10 to 20 times improvement in the matrix fill-time, as it was demonstrated through some examples. Additional improvement obtained from the frequency interpolation is moderate, about 2 to 3 times improvement in the total characterization time, and the accuracy of the results over the entire frequency band is dependent on the smoothness of the frequency response of the circuit under study and on the number of frequency samples.

As a result, the computational speed of the EM simulation program developed in this thesis has been substantially increased, and has been made on the same order as that of a commercial software developed for shielded geometries.

## Chapter 5

# Optimization

So far, the numerical technique presented in this thesis has been discussed from the analysis point of view, but in designing printed circuits, optimization plays an important role as well. For example, in order to improve the impedance bandwidth of a proximity-coupled microstrip antenna, one can add small tuning stub on the feeding line [58] which may result in an iterative procedure to find the best stub position and length.

There is a great deal of interest in the optimization algorithms that can be efficiently used with a full-wave EM simulation method in the design of printed circuits. The simulation models used in the optimization process can be classified as [69, 70]: *i.*) simplified continuous models, *ii.*) detailed continuous models, *iii.*) discrete coarse models, and *iv.*) discrete fine models. where the continuous and the discrete models are based on the circuit theory and EM field theory, respectively. Although the full-wave EM field theory models are more accurate than the continuous models, they run significantly slower. To overcome this difficulty, and to make the full-wave methods suitable for optimization algorithms, various approaches have been proposed. The direct way of doing optimization with a full-wave simulator requires a base generator which generates the input data file necessary for the EM simulation program by using the output of the optimizer. Another approach is called the Space Mapping Technique (SM) [69, 71], for which a mapping scheme between the coarse and fine discrete models

is established. In this approach, the optimization can be performed for a large number of coarse analysis and the results are improved, via a mapping technique, by performing a small number of fine analysis.

It can be concluded that in all these approaches using discrete methods, the simulation time consumed by the full-wave simulator is the key issue.

## 5.1 Genetic Algorithms

Gradient methods and random search methods are the two commonly used optimization algorithms which are employed in the optimization of microwave circuits. Gradient methods use the gradients of the cost function and converge to the minimum of the given functional very fast if the initial point is very close to the minimum, whereas, they have the disadvantage of converging to a local minimum. The random search methods, on the other hand, do not require the gradients but they are relatively slow. The two relatively new optimization methods, which can handle a large number of parameters, are the simulated annealing and the genetic algorithms [72–75]. The simulated annealing simulates the annealing process of metals, while the genetic algorithms simulate the evolutionary process of the living creatures. Since both of them try to simulate a natural phenomenon, they have the tendency of being slow, but give satisfactory results.

In this section, a genetic algorithm is used to demonstrate the optimization procedure with the formulation presented in this thesis. In a genetic algorithm, the parameters which are going to be optimized are encoded into binary sequences which are called as genes. Then, as in the natural process, the genes are crossed, eliminated, and mutated according to a predetermined algorithm until a convergence is reached. The flow-chart of a typical genetic algorithm is shown in Fig. 5.1.

The genetic algorithms are efficiently employed when one directly deals with the parameters which can be represented by single binary digits. An example of this situation occurs when it is desirable to obtain circular polarization from a rectangular patch antenna by adding or removing small rectangular metalization

cells from the antenna where each cell is represented by a binary digit [76].

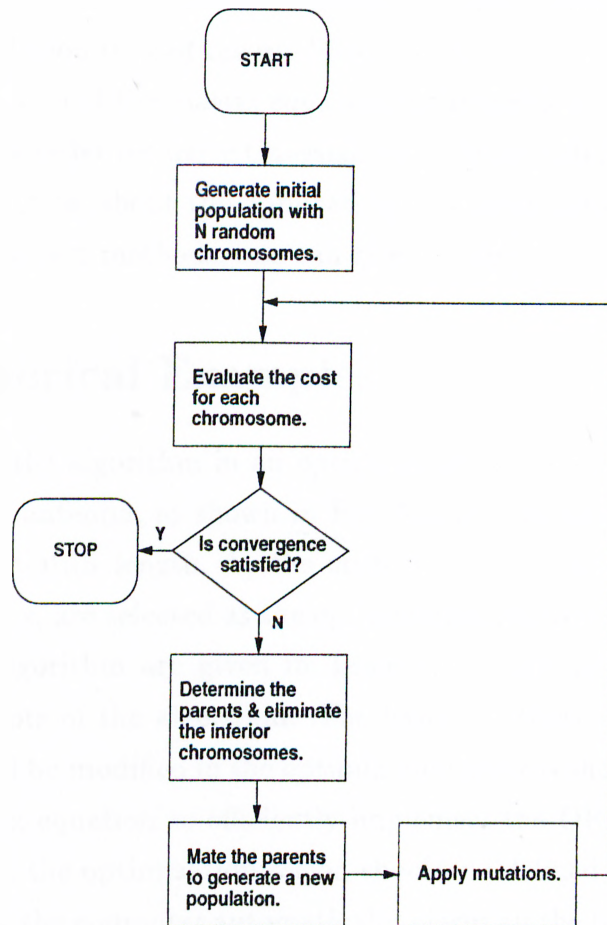


Figure 5.1: Flowchart of a typical genetic algorithm used in the optimization process.

An optimization algorithm, in general, requires the simulation program to analyze the modified geometry at each iteration. If the simulation program needs to analyze the modified geometry from scratch, the optimization algorithm would be computationally expensive even though the simulation program is efficient. Therefore, to assess the numerical efficiency of a simulation technique it is necessary to consider the suitability of the technique for optimization. The technique that we have presented here is very suitable because the effects of newly added or removed metallic regions are handled very fast by adding an additional

row-column pair to or removing a row-column pair from the original matrix, respectively. In addition to the efficient filling of the MoM matrix of the modified geometry, the solution time of the modified matrix equation can also be improved by using the solution of the matrix equation in the previous iteration through the method called the order recursive Gaussian elimination (ORGE) approach [77,78]. For more information about the application of various optimization algorithms, including the gradient methods, one can refer to [76].

## 5.2 Numerical Examples

To demonstrate the algorithm in an optimization problem, a proximity-coupled microstrip patch antenna, as shown in Fig. 5.2, is optimized for the impedance bandwidth. The stub length,  $h$ , the stub position,  $l$ , and the length of the coupling section,  $s$ , are selected as the optimization parameters. The parameters of the genetic algorithm are given in Table 5.1, which also summarizes some important concepts of the algorithm. The basis functions corresponding to the places that would be modified in the optimization process should be placed to the end of the matrix equation to efficiently implement the ORGE. Hence, prior to the optimization, the optimization region should be defined and be given to the computer so that the computer automatically places all the basis functions which fall inside this region to the end of the matrix equation, thus making the system suitable for ORGE. Note that this approach also reduces the matrix fill time by enabling the use of the previously calculated reaction integrals corresponding to the unmodified region.

The input reflection coefficient of the patch antenna, before and after optimization, can be seen in Fig. 5.3. The optimized values of the parameters are  $h=0.48$  cm,  $l=0.25$  cm, and  $s=0.25$  cm. Note that one can obtain a better matching by increasing the number of stub tuners at the feeding line, at the expense of increased spurious radiation.

It would also be instructive to demonstrate the time gained by implementing the ORGE. The CPU times for filling the matrix and for solving the matrix



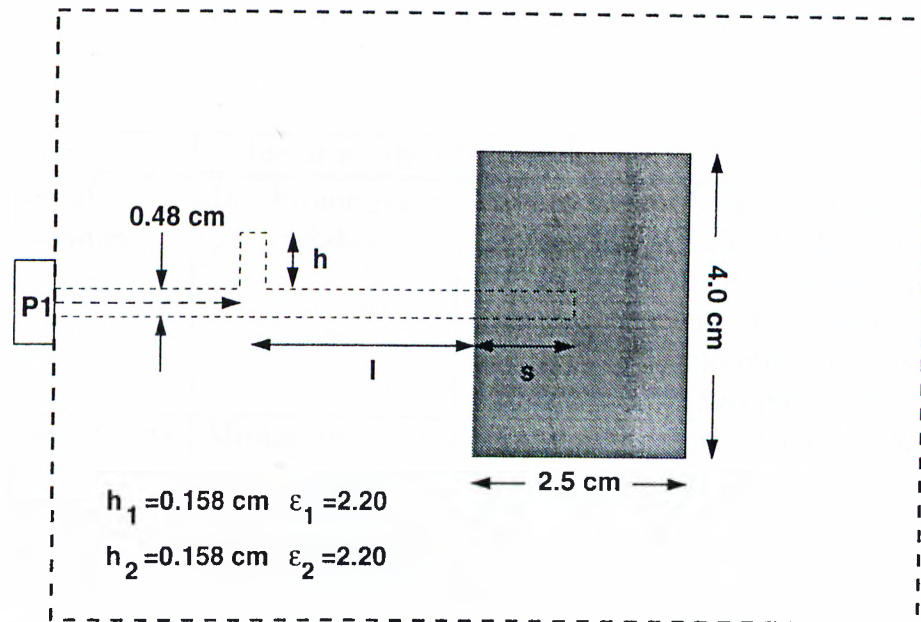


Figure 5.2: Geometry of the the proximity coupled microstrip antenna with tuning stub.

equation are shown in Figs. 5.4 and 5.5, respectively, during the optimization for each analysis. Note that if one analyzes the circuit from scratch at each iteration, the CPU times would be on the order of the levels shown at the top of the plots, which correspond to the CPU times for the analysis of the whole geometry with a tuning stub. So, eliminating the recalculation of the interactions of the basis functions which fall outside the optimization region, and implementing the ORGE, result in considerable improvement in the total analysis time. Another point which should be stressed is that after the first iteration, the Green's functions evaluation time reduces significantly because the generated Green's functions are saved in to the disk of the computer and are retrieved in the following iterations. Note that the optimization parameters do not contain the electrical and physical parameters of the layers. so the Green's functions can be used repeatedly.

The ultimate time efficiency for evaluating the reaction integrals in optimization process is achieved by precalculating all the matrix terms in the optimization

Parameter	Value or method	Remarks
Number of chromosomes	16 chromosomes per variable.	The number of chromosomes should be selected sufficiently high to span the optimization domain as much as possible. On the other hand, as the number of chromosomes increases, the simulation time also increases.
Number of bits in the chromosomes	Minimum 4, maximum 8.	As the number of bit increases, quantization error decreases giving a chance to find a better minimum.
Encoding	Gray encoding.	In Gray encoding, small changes in binary numbers also result small changes in continuous variables after decoding. Another method could be binary encoding.
Parent selection	Chromosomes are sorted according to cost function value.	This method sorts the chromosomes according to their cost function values and selects the first half of the list as parents. Another method could be "roulette-wheel selection" which introduces some randomness in parent selection.
Crossover	Two-point crossover.	In two-point crossover, the bit patterns of the parents are swapped in the kids between the two randomly selected points. Another method could be "one-point crossover".
Mutation rate	% 1.0	While producing a new generation during the optimization, bit patterns of one percent of the whole chromosomes are randomly changed.

Table 5.1: Parameters of the genetic algorithm used in the optimization.

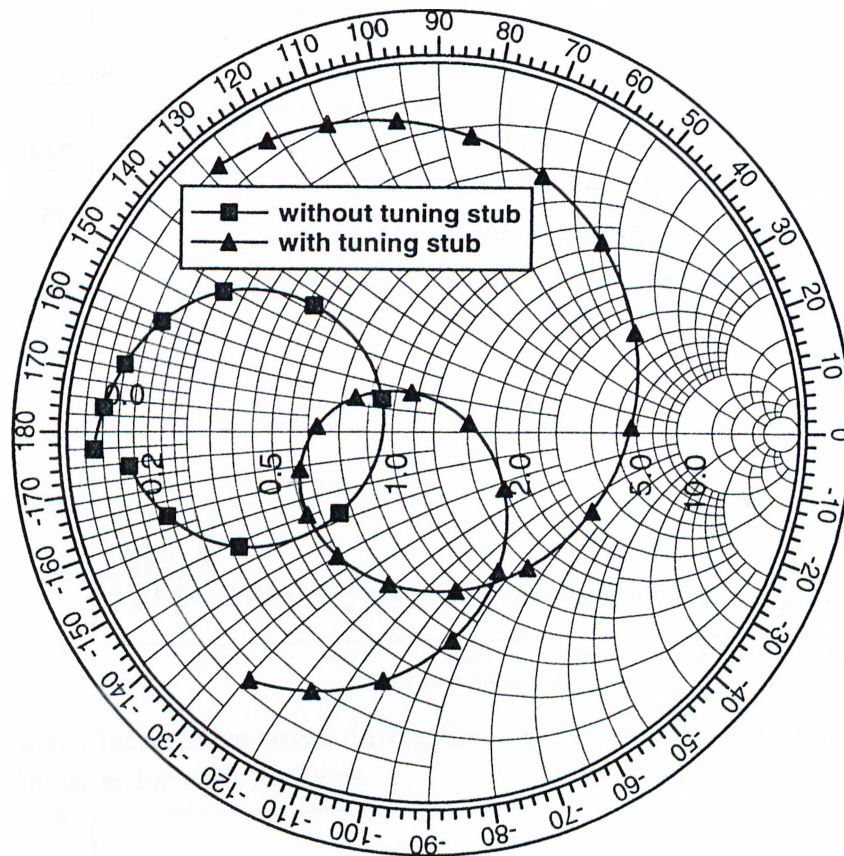


Figure 5.3:  $\Gamma_{in}$  of the the proximity coupled microstrip antenna shown in Fig. 5.2 before and after optimization.

region and storing into a table. Then, by simply selecting the necessary terms for each geometry from the table, the impedance matrix is filled. However, note that the advantage of this method is fully utilized in uniform segmentation only.

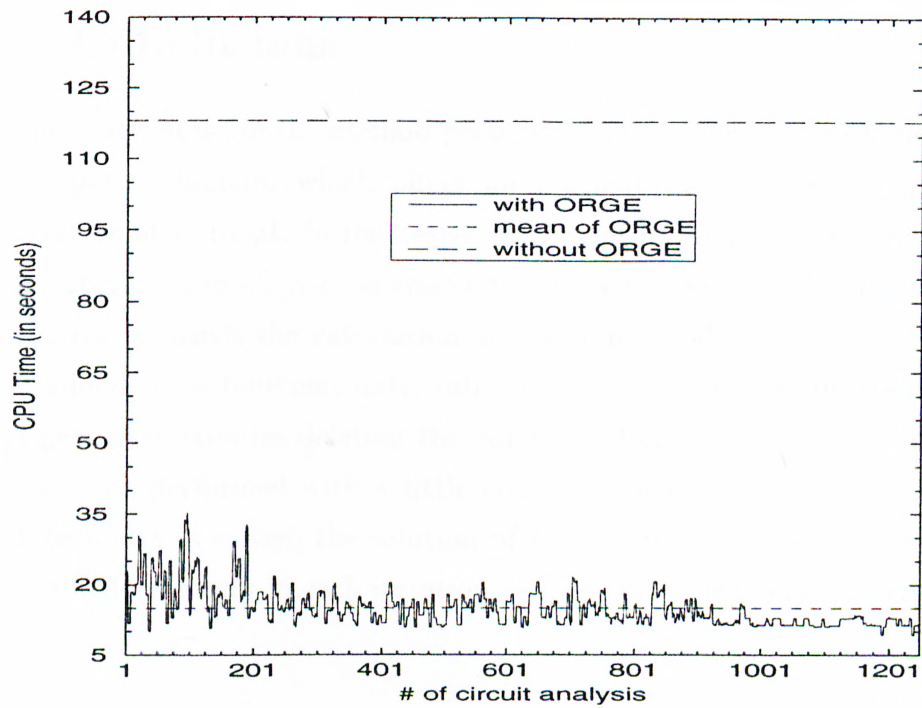


Figure 5.4: Matrix solve times during the optimization process on a SUN SPARC 20 workstation for each analysis.

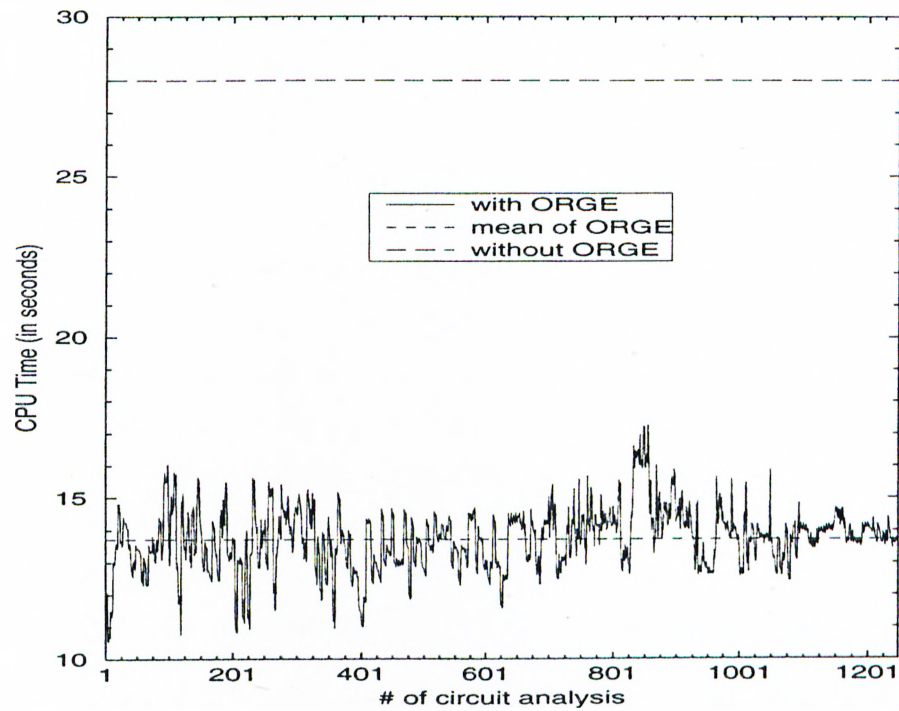


Figure 5.5: Matrix fill times during the optimization process on a SUN SPARC 20 workstation for each analysis.

### 5.3 Conclusions

The main advantage of the method presented in this thesis is its implementation in the spatial domain, which offers an efficient way in the design and the optimization of a circuit. In the design or the optimization process, one needs to add or subtract a small piece of conductor in each iteration. Addition of a small metallic region needs the calculation of the inner-product terms corresponding to the added basis functions only, subtracting a piece of metalization from the initial geometry requires deleting the corresponding rows and columns, both of which can be performed with a little computational cost. Moreover, once the initial geometry is solved, the solution of the matrix equation corresponding to the modified geometry in each iteration can be performed very efficiently.

# Chapter 6

## Conclusions

In this thesis, a novel full-wave CAD algorithm for the analysis of printed geometries was presented. The application of the method has been demonstrated on some realistic microwave circuits containing both horizontal and vertical conductors. The results were also verified with the results of a commercially available electromagnetic analysis software, *em* from SONNET Software Inc.

The method is formulated in the spatial-domain and uses the closed-form Green's functions for planarly layered media. The use of the spatial-domain closed-form Green's functions eliminates the numerical integration encountered in the evaluation of the reaction integrals, thus making the algorithm suitable to CAD applications. Vertical metalizations have been rigorously implemented and two approaches have been given to incorporate them with horizontal metalizations. In addition, a hybrid approach to fill the MoM matrices has been introduced in this thesis and a significant saving in the computation time has been achieved. With all these developments presented in this thesis, the spatial-domain MoM becomes the fastest method for the analysis of the printed structures in a general multilayer medium.

The salient features of the algorithm can be summarized as follows:

- Formulation is in the spatial-domain and uses the closed-form Green's functions which eliminates the numerical evaluation of the Sommerfeld integral.

- Circuits can contain both horizontal and vertical conductors, and there is no limitation on the lengths of the vertical connections.
- There is no limitation on the number of layers and thicknesses of layers.
- The reaction integrals are evaluated analytically with changing the approximation scheme of the Green's functions in a dynamic manner.
- Circuit are not placed in a conducting box. Therefore, radiating structures can be analyzed rigorously.
- It is possible to place horizontal ground planes to analyze stripline structures.
- N-port S-parameters of the circuits can be calculated at the given reference planes with removing the port discontinuities, and the lumped circuit models can be extracted.

# Appendix A

## Explicit Forms of the Green's Functions

As discussed in Chapter 3, some of the spectral-domain Green's functions need be cast into a specific form, where  $z$  and  $z'$  dependences are factored out. The only Green's function that does not require this factorization is  $\tilde{G}_{xx}^A$ , because it is always evaluated at constant  $z$ - and  $z'$ -planes. Therefore, the components of the spectral-domain Green's functions, except  $\tilde{G}_{xx}^A$ , are cast into suitable forms for the MPIE formulation presented here, and are given in this appendix for convenience. For a detailed derivation of the spectral-domain Green's functions, one can refer to Dural and Aksun [19].

### A.1 The Green's function $\tilde{G}_z^q$

Substituting (2.51) and (2.52) into (2.42), the following expression is obtained;

$$\begin{aligned} \tilde{G}_z^q = & \frac{1}{2jk_{z_i}\epsilon_i} \left\{ e^{-jk_{z_i}|z-z'|} + \tilde{R}_{TM}^{i,i-1} M_i^{TM} \left[ -e^{-jk_{z_i}(z+z')} + \tilde{R}_{TM}^{i,i+1} e^{-jk_{z_i}(z-z'+2d_i)} \right] \right. \\ & \left. + \tilde{R}_{TM}^{i,i+1} M_i^{TM} \left[ -e^{-jk_{z_i}(2d_i-z-z')} + \tilde{R}_{TM}^{i,i-1} e^{-jk_{z_i}(z'-z+2d_i)} \right] \right\} \quad (\text{A.1}) \end{aligned}$$

Then, re-arranging the terms results in

$$\tilde{G}_z^q = \frac{1}{2jk_{z_i}\epsilon_i} \left\{ e^{-jk_{z_i}|z-z'|} - \tilde{R}_{TM}^{i,i+1} M_i^{TM} e^{-jk_{z_i}(2d_i-z'-z)} - e^{-jk_{z_i}(z'+z)} \tilde{R}_{TM}^{i,i-1} M_i^{TM} \right.$$



$$+ \check{R}_{TM}^{i,i+1} \check{R}_{TM}^{i,i-1} M_i^{TM} e^{-jk_{z_i}(2d_i+z'-z)} + \check{R}_{TM}^{i,i-1} \check{R}_{TM}^{i,i+1} M_i^{TM} e^{-jk_{z_i}(2d_i+z-z')}} \} \quad (\text{A.2})$$

## A.2 The Green's function $\check{G}_{zz}^A$

Substituting (2.49) and (2.50) into (2.41), the following expression is obtained;

$$\begin{aligned} \check{G}_{zz}^A &= \frac{\mu_i}{2jk_{z_i}} \left\{ e^{-jk_{z_i}|z-z'|} + \check{R}_{TM}^{i,i-1} M_i^{TM} \left[ e^{-jk_{z_i}(z+z')} + \check{R}_{TM}^{i,i+1} e^{-jk_{z_i}(z-z'+2d_i)} \right] \right. \\ &\quad \left. + \check{R}_{TM}^{i,i+1} M_i^{TM} \left[ e^{-jk_{z_i}(2d_i-z-z')} + \check{R}_{TM}^{i,i-1} e^{-jk_{z_i}(z'-z+2d_i)} \right] \right\} \quad (\text{A.3}) \end{aligned}$$

Then, re-arranging the terms results in

$$\begin{aligned} \check{G}_{zz}^A &= \frac{\mu_i}{2jk_{z_i}} \left\{ e^{-jk_{z_i}|z-z'|} + \check{R}_{TM}^{i,i+1} M_i^{TM} e^{-jk_{z_i}(2d_i-z'-z)} + e^{-jk_{z_i}(z'+z)} \check{R}_{TM}^{i,i-1} M_i^{TM} \right. \\ &\quad \left. + \check{R}_{TM}^{i,i+1} \check{R}_{TM}^{i,i-1} M_i^{TM} e^{-jk_{z_i}(2d_i+z'-z)} + \check{R}_{TM}^{i,i-1} \check{R}_{TM}^{i,i+1} M_i^{TM} e^{-jk_{z_i}(2d_i+z-z')} \right\} \quad (\text{A.4}) \end{aligned}$$

## A.3 The Green's function $\check{G}_{zx}^A$

Substituting (2.45), (2.46), (2.47) and (2.48) into (2.36), the following expression is obtained;

$$\begin{aligned} \check{G}_{zx}^A &= -\frac{\mu_i}{2jk_{z_i}} \left\{ \frac{k_x k_{z_i}}{k_\rho^2} \left( \check{R}_{TE}^{i,i+1} M_i^{TE} \left[ e^{-jk_{z_i}(2d_i-z'-z)} + \check{R}_{TE}^{i,i-1} e^{-jk_{z_i}(2d_i+z'-z)} \right] \right. \right. \\ &\quad \left. \left. + \check{R}_{TM}^{i,i+1} M_i^{TM} \left[ e^{-jk_{z_i}(2d_i-z'-z)} - \check{R}_{TM}^{i,i-1} e^{-jk_{z_i}(2d_i+z'-z)} \right] \right) \right. \\ &\quad \left. + \frac{k_x k_{z_i}}{k_\rho^2} \left( \check{R}_{TM}^{i,i-1} M_i^{TM} \left[ -e^{-jk_{z_i}(z+z')} + \check{R}_{TM}^{i,i+1} e^{-jk_{z_i}(2d_i+z-z')} \right] \right. \right. \\ &\quad \left. \left. - \check{R}_{TE}^{i,i-1} M_i^{TE} \left[ e^{-jk_{z_i}(z+z')} + \check{R}_{TE}^{i,i+1} e^{-jk_{z_i}(2d_i+z-z')} \right] \right) \right\}. \quad (\text{A.5}) \end{aligned}$$

Then, re-arranging the terms results in

$$\begin{aligned} \check{G}_{zx}^A &= -jk_x \frac{\mu_i}{2jk_{z_i}} \frac{-jk_{z_i}}{k_\rho^2} \left\{ e^{-jk_{z_i}(2d_i-z'-z)} \left( \check{R}_{TE}^{i,i+1} M_i^{TE} + \check{R}_{TM}^{i,i+1} M_i^{TM} \right) \right. \\ &\quad \left. + e^{-jk_{z_i}(2d_i+z'-z)} \left( \check{R}_{TE}^{i,i+1} \check{R}_{TE}^{i,i-1} M_i^{TE} - \check{R}_{TM}^{i,i+1} \check{R}_{TM}^{i,i-1} M_i^{TM} \right) \right. \\ &\quad \left. + e^{-jk_{z_i}(2d_i+z-z')} \left( \check{R}_{TM}^{i,i-1} \check{R}_{TM}^{i,i+1} M_i^{TM} - \check{R}_{TE}^{i,i-1} \check{R}_{TE}^{i,i+1} M_i^{TE} \right) \right. \\ &\quad \left. + e^{-jk_{z_i}(z'+z)} \left( -\check{R}_{TE}^{i,i-1} M_i^{TE} - \check{R}_{TM}^{i,i-1} M_i^{TM} \right) \right\} \quad (\text{A.6}) \end{aligned}$$

## A.4 The Green's function $\tilde{G}_x^q$

Substituting (2.45), (2.46), (2.47) and (2.48) into (2.37), the following expression is obtained;

$$\begin{aligned}
 \tilde{G}_x^q &= \frac{1}{2j\epsilon_i k_{z_i}} \left\{ e^{-jk_{z_i}|z-z'|} \right. \\
 &+ \frac{k_{z_i}^2}{k_\rho^2} \tilde{R}_{TM}^{i,i+1} M_i^{TM} \left[ e^{-jk_{z_i}(2d_i-z'-z)} - \tilde{R}_{TM}^{i,i-1} e^{-jk_{z_i}(2d_i+z'-z)} \right] \\
 &+ \frac{k_i^2}{k_\rho^2} \tilde{R}_{TE}^{i,i+1} M_i^{TE} \left[ e^{-jk_{z_i}(2d_i-z'-z)} + \tilde{R}_{TE}^{i,i-1} e^{-jk_{z_i}(2d_i+z'-z)} \right] \\
 &+ \frac{k_i^2}{k_\rho^2} \tilde{R}_{TE}^{i,i-1} M_i^{TE} \left[ e^{-jk_{z_i}(z+z')} + \tilde{R}_{TE}^{i,i+1} e^{-jk_{z_i}(2d_i+z-z')} \right] \\
 &\left. - \frac{k_{z_i}^2}{k_\rho^2} \tilde{R}_{TM}^{i,i-1} M_i^{TM} \left[ -e^{-jk_{z_i}(z+z')} + \tilde{R}_{TM}^{i,i+1} e^{-jk_{z_i}(2d_i+z-z')} \right] \right\} \quad (\text{A.7})
 \end{aligned}$$

Then, re-arranging the terms results in

$$\begin{aligned}
 \tilde{G}_x^q &= \frac{1}{2j\epsilon_i k_{z_i}} \left\{ e^{-jk_{z_i}|z-z'|} \right. \\
 &+ e^{-jk_{z_i}(2d_i-z'-z)} \left( \frac{k_{z_i}^2}{k_\rho^2} \tilde{R}_{TM}^{i,i+1} M_i^{TM} + \frac{k_i^2}{k_\rho^2} \tilde{R}_{TE}^{i,i+1} M_i^{TE} \right) \\
 &+ e^{-jk_{z_i}(2d_i+z'-z)} \left( -\frac{k_{z_i}^2}{k_\rho^2} \tilde{R}_{TM}^{i,i+1} \tilde{R}_{TM}^{i,i-1} M_i^{TM} + \frac{k_i^2}{k_\rho^2} \tilde{R}_{TE}^{i,i+1} \tilde{R}_{TE}^{i,i-1} M_i^{TE} \right) \\
 &+ e^{-jk_{z_i}(2d_i+z-z')} \left( -\frac{k_{z_i}^2}{k_\rho^2} \tilde{R}_{TM}^{i,i+1} \tilde{R}_{TM}^{i,i-1} M_i^{TM} + \frac{k_i^2}{k_\rho^2} \tilde{R}_{TE}^{i,i-1} \tilde{R}_{TE}^{i,i+1} M_i^{TE} \right) \\
 &\left. + e^{-jk_{z_i}(z'+z)} \left( \frac{k_{z_i}^2}{k_\rho^2} \tilde{R}_{TM}^{i,i-1} M_i^{TM} + \frac{k_i^2}{k_\rho^2} \tilde{R}_{TE}^{i,i-1} M_i^{TE} \right) \right\} \quad (\text{A.8})
 \end{aligned}$$

# Appendix B

## Evaluation of the Inner Products

In Chapter 3, the evaluation of the inner-products corresponding to the vertical metalizations is demonstrated on a typical inner-product term. In this appendix, the evaluations of the other inner-products containing integration operations on  $z$  and  $z'$  variables are given.

### B.1 Evaluation of $\left\langle \frac{\partial}{\partial z} T_{zm}, G_x^q * \frac{\partial J_{xn}}{\partial x} \right\rangle$

This term contains integration and derivation with respect to  $z$ , and the inner product is written as follows

$$\begin{aligned} \left\langle \frac{\partial}{\partial z} T_{zm}, G_x^q * \frac{\partial J_{xn}}{\partial x} \right\rangle &= \iint dz dy \frac{\partial}{\partial z} T_{zm}(y, z) \\ &\cdot \iint dx' dy' G_x^q(x - x', y - y', z) \frac{\partial}{\partial x'} J_{xn}(x', y') \end{aligned} \quad (\text{B.1})$$

At first, the spatial-domain Green's function in (B.1) is replaced with the spectral-domain Green's function by using (2.57) and then the integration with respect to  $z$  is considered:

$$\begin{aligned} F_x^q &\stackrel{\text{def}}{=} \int dz \frac{\partial}{\partial z} T_{zm}(z) \frac{1}{4\pi} \int_{SIP} dk_\rho k_\rho H_0^{(2)}(k_\rho \rho) \check{G}_x^q(k_\rho) \\ &= \frac{1}{4\pi} \int_{SIP} dk_\rho k_\rho H_0^{(2)}(k_\rho \rho) \int dz \frac{\partial}{\partial z} T_{zm}(z) \check{G}_x^q(k_\rho) \end{aligned} \quad (\text{B.2})$$

where  $\tilde{G}_x^q$  is given in (A.8). After evaluating the  $z$  integral, the inner-product (B.1) reduces to

$$\left\langle \frac{\partial}{\partial z} T_{zm}, G_x^q * \frac{\partial J_{zn}}{\partial x} \right\rangle = \int dy T_{zm}(y) \iint dx' dy' F_x^q \frac{\partial}{\partial x'} J_{zn}(x', y') \quad (\text{B.3})$$

by making the substitutions  $x - x' = u$  and  $y - y' = v$ , the following expression is obtained

$$\left\langle \frac{\partial}{\partial z} T_{zm}, G_x^q * \frac{\partial J_{zn}}{\partial x} \right\rangle = \iint du dv F_x^q \int dy T_{zm}(y) \frac{\partial}{\partial x'} J_{zn}(x - u, y - v) \quad (\text{B.4})$$

where  $x = x_i$ .

## B.2 Evaluation of $\left\langle \frac{\partial}{\partial x} T_{xm}, G_z^q * \frac{\partial J_{zn}}{\partial z} \right\rangle$

This term contains integration and derivation with respect to  $z$ , and the inner product is written as follows

$$\begin{aligned} \left\langle \frac{\partial}{\partial x} T_{xm}, G_z^q * \frac{\partial J_{zn}}{\partial z} \right\rangle &= \iint dx dy \frac{\partial}{\partial x} T_{xm}(x, y) \\ &\cdot \iint dz' dy' G_z^q(x - x', y - y', z') \frac{\partial}{\partial z'} J_{zn}(y', z') \end{aligned} \quad (\text{B.5})$$

At first, the spatial-domain Green's function in (B.5) is replaced with the spectral-domain Green's function by using (2.57) and then the integration with respect to  $z$  is considered:

$$\begin{aligned} F_z^{q_1} &\stackrel{\text{def}}{=} \int dz' \frac{\partial}{\partial z'} J_{zn}(z') \frac{1}{4\pi} \int_{SIP} dk_\rho k_\rho H_0^{(2)}(k_\rho \rho) \tilde{C}_z^q(k_\rho) \\ &= \frac{1}{4\pi} \int_{SIP} dk_\rho k_\rho H_0^{(2)}(k_\rho \rho) \int dz' \frac{\partial}{\partial z'} J_{zn}(z') \tilde{C}_z^q(k_\rho) \end{aligned} \quad (\text{B.6})$$

where  $\tilde{C}_z^q$  is given in (A.1). After evaluating the  $z'$  integral, the inner-product (B.5) reduces to

$$\left\langle \frac{\partial}{\partial x} T_{xm}, G_z^q * \frac{\partial J_{zn}}{\partial z} \right\rangle = \iint dx dy \frac{\partial}{\partial x} T_{xm}(x, y) \int dy' F_z^{q_1} J_{zn}(y') \quad (\text{B.7})$$

by making the substitutions  $x - x' = u$  and  $y - y' = v$ , the following expression is obtained

$$\left\langle \frac{\partial}{\partial x} T_{xm}, G_z^q * \frac{\partial J_{zn}}{\partial z} \right\rangle = - \iint du dv F_z^{q1} \int dy \frac{\partial}{\partial x} T_{xm}(x' + u, y) J_{zn}(y - v) \quad (\text{B.8})$$

where  $x' = x_i$ .

### B.3 Evaluation of $\left\langle \frac{\partial}{\partial z} T_{zm}, G_z^q * \frac{\partial J_{zn}}{\partial z} \right\rangle$

This term contains integration and derivation with respect to  $z$  and  $z'$ , and the inner product is written as follows

$$\begin{aligned} \left\langle \frac{\partial}{\partial z} T_{zm}, G_z^q * \frac{\partial J_{zn}}{\partial z} \right\rangle &= \iint dz dy \frac{\partial}{\partial z} T_{zm}(y, z) \\ &\cdot \iint dz' dy' G_z^q(x - x', y - y', z, z') \frac{\partial}{\partial z'} J_{zn}(y', z') \end{aligned} \quad (\text{B.9})$$

At first, the spatial-domain Green's function in (B.9) is replaced with the spectral-domain Green's function by using (2.57) and then the integrations with respect to  $z$  and  $z'$  are considered:

$$\begin{aligned} F_z^{q2} &\stackrel{\text{def}}{=} \iint dz dz' \frac{\partial}{\partial z} T_{zm}(z) \frac{1}{4\pi} \int_{SIP} dk_\rho k_\rho H_0^{(2)}(k_\rho \rho) \tilde{G}_z^q(k_\rho) \frac{\partial}{\partial z'} J_{zn}(z') \\ &= \frac{1}{4\pi} \int_{SIP} dk_\rho k_\rho H_0^{(2)}(k_\rho \rho) \iint dz dz' \frac{\partial}{\partial z} T_{zm}(z) \frac{\partial}{\partial z'} J_{zn}(z') \tilde{G}_z^q(k_\rho) \end{aligned} \quad (\text{B.10})$$

where  $\tilde{G}_z^q$  is given in (A.1). After evaluating the  $z$  and  $z'$  integrals, the inner-product (B.9) reduces to

$$\left\langle \frac{\partial}{\partial z} T_{zm}, G_z^q * \frac{\partial J_{zn}}{\partial z} \right\rangle = \int dy T_{zm}(y) \int dy' F_z^{q2} J_{zn}(y') \quad (\text{B.11})$$

by making the substitution  $y - y' = v$ , the following expression is obtained

$$\left\langle \frac{\partial}{\partial z} T_{zm}, G_z^q * \frac{\partial J_{zn}}{\partial z} \right\rangle = - \int dv F_z^{q2} \int dy T_{zm}(y) J_{zn}(y - v) \quad (\text{B.12})$$

where  $x = x' = x_i$ .

## B.4 Evaluation of $\langle T_{zm}, G_{zz}^A * J_{zn} \rangle$

This term contains integration with respect to  $z$  and  $z'$ , and the inner product is written as follows

$$\begin{aligned} \langle T_{zm}, G_{zz}^A * J_{zn} \rangle &= \iint dz dy T_{zm}(y, z) \\ &\cdot \iint dz' dy' G_{zz}^A(x - x', y - y', z, z') J_{zn}(y', z') \end{aligned} \quad (\text{B.13})$$

At first, the spatial-domain Green's function in (B.13) is replaced with the spectral-domain Green's function by using (2.57) and then the integrations with respect to  $z$  and  $z'$  are considered:

$$\begin{aligned} F_{zz}^A &\stackrel{\text{def}}{=} \iint dz dz' T_{zm}(z) \frac{1}{4\pi} \int_{SIP} dk_\rho k_\rho H_0^{(2)}(k_\rho \rho) \check{G}_{zz}^A(k_\rho) J_{zn}(z') \\ &= \frac{1}{4\pi} \int_{SIP} dk_\rho k_\rho H_0^{(2)}(k_\rho \rho) \iint dz dz' T_{zm}(z) J_{zn}(z') \check{G}_{zz}^A(k_\rho) \end{aligned} \quad (\text{B.14})$$

where  $\check{G}_{zz}^A$  is given in (A.3). After evaluating the  $z$  and  $z'$  integrals, the inner-product (B.13) reduces to

$$\langle T_{zm}, G_{zz}^A * J_{zn} \rangle = \int dy T_{zm}(y) \int dy' J_{zn}(x', y') F_{zz}^A \quad (\text{B.15})$$

by making the substitution  $y - y' = v$ , the following expression is obtained

$$\langle T_{zm}, G_{zz}^A * J_{zn} \rangle = - \int dv F_{zz}^A \int dy T_{zm}(y) J_{zn}(y - v) \quad (\text{B.16})$$

where  $x = x' = x_i$ .

## B.5 Evaluation of the other terms

Evaluation of  $\langle \frac{\partial}{\partial z} T_{zm}, G_x^q * \frac{\partial J_{xsp}}{\partial x} \rangle$ ,  $\langle T_{zm}, G_{zx}^A * J_{xsp} \rangle$ ,  $\langle T_{zm}, G_{zx}^A * J_{x0} \rangle$ , and  $\langle \frac{\partial}{\partial z} T_{zm}, G_x^q * \frac{\partial J_{x0}}{\partial x} \rangle$  are similar with the ones discussed above, the only difference is the basis functions used. Therefore, they will not be shown here.

# Appendix C

## Generalized Pencil of Function Algorithm

As mentioned in Chapter 2, the generalized pencil of function algorithm is used to approximate the spectral domain Green's functions with complex exponentials. Since the application of the algorithm is an important step in approximating the Green's functions, it is given in this appendix for convenience.

It is well known that the Prony method and its variants can be used to extract the poles [79, 80] of an EM system. The pencil of function (POF) method [23] is an alternative method to the Prony method to find the system poles. In POF, the poles are found from the solution of a generalized eigenvalue problem, whereas the Prony method contains a two-step process where the first step involves the solution of a matrix equation and the second step involves finding the roots of a polynomial. The generalized pencil of function method is a generalization to the POF method and it is used to estimate the poles of an EM system from its transient response [22]. Compared to the Prony method, the GPOF method is more robust and less noise sensitive.

Now consider an EM transient signal which can be approximated as follows

$$y_k = \sum_{i=1}^M b_i \cdot e^{s_i \delta t k} \quad k = 0, 1, \dots, N-1 \quad (\text{C.1})$$

where  $b_i$  are the complex residues,  $s_i$  are the complex poles, and  $\delta t$  is the sampling

interval. In order to find the poles, one can use the following algorithm [22]:

1. Construct the following matrices,

$$Y_1 = [\mathbf{y}_0, \mathbf{y}_1, \dots, \mathbf{y}_{L-1}] \quad (\text{C.2})$$

$$Y_2 = [\mathbf{y}_1, \mathbf{y}_2, \dots, \mathbf{y}_L] \quad (\text{C.3})$$

where

$$\mathbf{y}_i = [y_i, y_{i+1}, \dots, y_{i+N-L-1}]^T \quad (\text{C.4})$$

and  $L$  is the pencil parameter, and its optimal choice is around  $L = N/2$  [22].

2. Find a  $Z$  matrix as follows,

$$VD^{-1}U^H = \text{SVD}(Y_1) \quad (\text{C.5})$$

$$V \leftarrow [V]_{M \times M}$$

$$U \leftarrow [U]_{M \times M}$$

$$D \leftarrow [D]_{M \times M}$$

$$Z = D^{-1}U^H Y_2 V \quad (\text{C.6})$$

where  $\text{SVD}(\cdot)$  and superscript  $H$  denote the singular value decomposition process and the complex conjugate transpose of a matrix, respectively. The number of exponentials,  $M$ , is selected according to the significant singular values of the matrix  $Y_1$ .

3. The poles of the system are obtained as

$$s_i = \frac{\log z_i}{\delta t} \quad i = 1, 2, \dots, M \quad (\text{C.7})$$

where  $z_i$ 's are the eigenvalues of the  $Z$  matrix evaluated in step 2.



4. The residues are found from the least-squares solution of the following system

$$\begin{bmatrix} 1 & 1 & 1 \\ z_1 & z_2 & z_M \\ \vdots & \vdots & \vdots \\ z_1^{N-1} & z_2^{N-1} & \dots & z_M^{N-1} \end{bmatrix} \begin{bmatrix} b_1 \\ b_2 \\ \vdots \\ b_M \end{bmatrix} = \begin{bmatrix} y_0 \\ y_1 \\ \vdots \\ y_{N-1} \end{bmatrix} \quad (\text{C.8})$$

For the sake of completeness, the following MATLAB function, which implements the GPOF algorithm, is also given here.

APPENDIX C. GENERALIZED PENCIL OF FUNCTION ALGORITHM 105

```
%
% This MATLAB script file approximates a given
% function with complex exponentials by using
% the Generalized Pencil of Function (GPOF)
% method in the following form:
%
%  $f(t)=B(1)*\exp(e(1)*Dt*t) + B(2)*\exp(e(2)*Dt*t) + \dots + B(M)*\exp(e(M)*Dt*t)$ 
%
% Input arguments:
%
% f: Samples of the function which is going
%     to be approximated.
% N: Number of sample points which is going
%     to be used in the approximation.
% M: Number of the exponentials.
%
% Output arguments:
%
% e:      Array containing the complex poles.
% B:      Array containing the complex residues.
% fapprx: Samples of the approximated function.
% error:  Error in the approximation.
% apprxtime: CPU time consumed in the approximation process.
%
function [e,B,fapprx,error,apprxtime]=gpof(f, N, M)
%
%
%
G=f(1:N);
L=N/2;
%
```

APPENDIX C. GENERALIZED PENCIL OF FUNCTION ALGORITHM 106

```
start=cputime;
%
% Construct the information vectors.
%
for i=1:L
Y1(:,i)=G(i:i+N-L-1);
end;
%
for i=1:L
Y2(:,i)=G(i+1:i+N-L);
end;
%
% Apply singular value decomposition to Y1.
%
[U,D,V]=svd(Y1);
DD=diag(diag(D(:,1:M)));
UU=U(:,1:M);
VV=V(:,1:M);
%
% Find the complex poles.
%
Z=inv(DD)*UU'*Y2*VV;
z=eig(Z);
e=log(z);
%
%
%
for i=1:N
for k=1:M
ZZ(i, k)=z(k)^(i-1);
end;
end;
```

APPENDIX C. GENERALIZED PENCIL OF FUNCTION ALGORITHM 107

```
end;
%
% Find the complex residues.
%
B=ZZ\G;
%
% Find the total CPU time.
%
approxtime=cputime-start;
%
% Find the error in the approximation.
%
for k=1:N
fapprox(k,1)=0.0;
for i=1:M
fapprox(k,1)=fapprox(k)+B(i)*exp(e(i)*(k-1));
end;
end;
%
error=norm(G-fapprox);
```

# Appendix D

## Method of Moments

The basic idea of representing a linear operator equation with a linear matrix equation is relatively old. It was first developed by a Russian mechanical engineer, Galerkin, around 1915, before it had a rigorous mathematical basis. Later, Rumsey [81] applied the variational methods to electromagnetics which are called as “reaction concept”. Method of Moments (MoM) is a general procedure which is used in solving linear equations [5,6], and in this appendix, the MoM is briefly described.

Consider a deterministic linear system in the following form:

$$\mathcal{L}f = g \quad (\text{D.1})$$

where  $\mathcal{L}$  is a linear operator, and  $g$  is a known function. Here, the aim is to find an approximation to  $f$  when the exact or closed-form solution of Eq. (D.1) is not possible. For this purpose,  $f$  is expanded in a series of linearly independent functions  $f_1, f_2, \dots, f_N$  as

$$f = \sum_{n=1}^N \alpha_n f_n \quad (\text{D.2})$$

where  $\alpha_n$ 's are the constants which are going to be determined. The functions  $f_n$  are selected such that analytical or robust numerical evaluation of  $\mathcal{L}f_n$  is possible. By substituting (D.2) into (D.1), the following expression is obtained

$$\sum_{n=1}^N \alpha_n \mathcal{L}f_n = g \quad (\text{D.3})$$

In order to find the unknown coefficients uniquely, it is necessary to have  $N$  linearly independent equations. To achieve this, a suitable inner product  $\langle f, g \rangle$  is defined and a series of linearly independent testing functions  $w_1, w_2, \dots, w_N$  are used to have an expression in the following form

$$\sum_{n=1}^N \alpha_n \langle w_m, \mathcal{L}f_n \rangle = g \quad m = 1, 2, 3, \dots, N \quad (\text{D.4})$$

Now, there are  $N$  equations with  $N$  unknowns, hence the unknown coefficients can be found uniquely. This set of equations can be written also in matrix form as follows

$$\begin{bmatrix} \langle w_1, \mathcal{L}f_1 \rangle & \langle w_1, \mathcal{L}f_2 \rangle & \cdots \\ \langle w_2, \mathcal{L}f_1 \rangle & \langle w_2, \mathcal{L}f_2 \rangle & \cdots \\ \vdots & \vdots & \ddots \end{bmatrix} \begin{bmatrix} \alpha_1 \\ \alpha_2 \\ \vdots \\ \alpha_N \end{bmatrix} = \begin{bmatrix} \langle w_1, g \rangle \\ \langle w_2, g \rangle \\ \vdots \\ \langle w_N, g \rangle \end{bmatrix} \quad (\text{D.5})$$

One of the main tasks in solving a linear equation through MoM, is the proper selection of basis and testing functions. The selected basis functions should approximate the function  $f$  as close as possible and constitute a linearly independent set. The testing functions should also constitute a linearly independent set.

## D.1 Variational Interpretation

In this section, the link between the MoM and variational methods is going to be explained. In a variational method, a functional which has a stationary point at the exact solution of a physical problem is first derived. Then by using trial functions, an approximate solution is obtained by minimizing or maximizing the functional. This method is called as Rayleigh-Ritz procedure.

It can be shown that the following expression is a variational expression for Eq. (D.1):

$$I = \langle f^*, \mathcal{L}f \rangle - \langle f^*, g \rangle - \langle g^*, f \rangle \quad (\text{D.6})$$

where  $\mathcal{L}$  is a self-adjoint operator which implies that

$$\langle f_2^*, \mathcal{L}f_1 \rangle = \langle f_1^*, \mathcal{L}f_2 \rangle^* \quad (\text{D.7})$$

The meaning of the variational expression is that when a function  $f$  with an error  $\delta f$  is introduced into Eq. (D.6), a better estimate of  $I$  with an higher error rate of  $(\delta f)^2$  is obtained. In order to show that Eq. (D.6) is really a variational expression, we let

$$f = f_e + \delta f \quad (\text{D.8})$$

and substitute Eq. (D.8) into Eq. (D.6). Then by equating the first order terms

$$\delta I = \langle f_e^*, \mathcal{L}\delta f \rangle + \langle \delta f^*, \mathcal{L}f_e \rangle - \langle \delta f^*, g \rangle - \langle g^*, \delta f \rangle \quad (\text{D.9})$$

Now, it can be shown that by using the self-adjoint property of the linear operator, right-hand side of Eq. (D.9) equals to zero. Therefore,  $\delta I$  or the first variation of  $I$  around the exact solution  $f_e$  is zero implying a stationary behavior. After showing that Eq. (D.6) is an variational expression for Eq. (D.1), the remaining procedure is to use this property to find an approximate solution for  $f$ . For this purpose, the function  $f$  is expressed by using trial functions as follows which is again given here for convenience.

$$f = \sum_{n=1}^N a_n f_n \quad (\text{D.10})$$

Here, if  $f_n$  is from a complete set, then there exist  $a_n$  values which gives an increasingly good approximation as  $N \rightarrow \infty$ . Then by substituting (D.10) into (D.6) the following expression is obtained.

$$I = \sum_{n=1}^N \sum_{m=1}^N a_m^* a_n \langle f_m^*, \mathcal{L}f_n \rangle - \sum_{n=1}^N a_n \langle f_n^*, g \rangle - \sum_{n=1}^N a_n \langle g^*, f_n \rangle \quad (\text{D.11})$$

$$= \mathbf{a}^T \cdot \mathbf{L} \cdot \mathbf{a} - 2\text{Re} [\mathbf{a}^T \cdot \mathbf{g}] \quad (\text{D.12})$$

where

$$[\mathbf{L}]_{mn} = \langle f_m^*, \mathcal{L}f_n \rangle \quad (\text{D.13})$$

$$[\mathbf{g}]_n = \langle f_n^*, g \rangle \quad (\text{D.14})$$

In order to obtain the optimal value of  $\mathbf{a}$ , we let  $\mathbf{a} = \mathbf{a}_0 + \delta\mathbf{a}$  and find  $\delta I$

$$\delta I = \delta\mathbf{a}^T \cdot \mathbf{L} \cdot \mathbf{a}_0 + \delta\mathbf{a}_0^T \cdot \mathbf{L} \cdot \delta\mathbf{a} - 2\text{Re} [\delta\mathbf{a}^T \cdot \mathbf{g}] = 0 \quad (\text{D.15})$$

Note that, in Eq. (D.15),  $\delta I$  is assigned to zero since we know that the optimal value of  $\mathbf{a}$  makes  $I$  stationary. To satisfy Eq. (D.15), one requires

$$\text{Re} [\delta\mathbf{a}^T \cdot \mathbf{L} \cdot \mathbf{a}_0] = \text{Re} [\delta\mathbf{a}^T \cdot \mathbf{g}] \quad (\text{D.16})$$

which results the following expression

$$\mathbf{L} \cdot \mathbf{a}_0 = \mathbf{g} \quad (\text{D.17})$$

Note that the above system is the same with system given in (D.5). Therefore, in the method of moments, choosing  $w_n = f_n$  is equivalent to the Rayleigh-Ritz variational method and it is called as the Galerkin's method.



# Appendix E

## Series Acceleration Methods Used in EM

Numerical techniques used in the solution of electromagnetic problems require, in general, either evaluating oscillatory integrals over infinite domain or calculating the sums of infinite complex series. For example, the method of moments (MoM) in the spectral domain for two-dimensional geometry requires double-infinite integration of complex highly oscillatory functions; the MoM in the spatial domain employs the spatial domain Green's functions, which are defined as the Hankel transform of the spectral domain Green's function; in the analysis of a periodic structure one needs to employ a periodic Green's function which has double infinite summations; or, in the analysis of a microstrip patch antenna via cavity model, the input impedance or field distribution are written in terms of an infinite sum of modes in the cavity.

If the summations and integrals given in the examples above are evaluated by "brute force" as they appear in the problems, the corresponding methods could be computationally very inefficient, rendering these problems impractical. To overcome this computational burden, special acceleration techniques, also called transformation techniques, for both integrals and summations have been proposed and successfully employed. Since these techniques have been studied for specific problems and compared to only a few other techniques,

the potentials of these techniques with their advantages and disadvantages have not been examined entirely for electromagnetic problems. Hence the contributions of this appendix are in *i.*) providing the complete set of acceleration techniques used in the electromagnetic problems, *ii.*) comparatively studying the acceleration techniques for integrals and series, and *iii.*) introducing a new acceleration technique for integrals involving Bessel functions and sinusoidal functions. The transformations given and compared in this appendix are the Euler transformation [82], Shanks' Transformation [83, 84], Wynn's  $\varepsilon$  algorithm, the method of averages [85], the Chebyshev-Toeplitz algorithm [86, 87], the  $\Theta$  algorithm [88, 89], the Poisson transformation [90], Ewald's transformation [91], Kummer's transformation, and the method of exponentials.

## E.1 The Transformation Methods

The principle of a series acceleration method is to transform a slowly convergent sequence, by using a linear or nonlinear mapping, to a new, faster converging sequence. Since there is not any universal algorithm which could work for every type of sequence, one should try different algorithms to obtain the optimum result for the problem under investigation. Hence the acceleration methods used can be divided into two main groups: general methods and specific methods. A general transformation method can be applied to any sequence which can be obtained from an infinite series or an infinite oscillatory integral. Examples of such methods are the Euler transformation, Shanks' transformation, Wynn's  $\varepsilon$  algorithm, the Chebyshev-Toeplitz algorithm, and the  $\Theta$ -algorithm. On the other hand, specific methods are derived by analytically working on the kernel of a series or of an integral. Therefore they can be applied only on their own types, but they usually work better than the general methods. The Method of averages, the Method of exponentials, the Poisson transformation, Ewald's transformation, and Kummer's transformation are the examples. Since the partial sums of an infinite series are used in most of the transformation methods, it would be instructive to define

them for an infinite series as follows:

$$\sum_{i=0}^{\infty} a_i = a_0 + a_1 + a_2 + a_3 + \dots \quad (\text{E.1})$$

$$A_n = a_0 + a_1 + a_2 + \dots + a_n \quad n = 0, 1, 2, \dots \quad (\text{E.2})$$

where  $A_n$  denotes the partial sum of (E.1) for  $n$  terms.

### E.1.1 Euler's Transformation

Euler's transformation can only be used for an alternating series and the equation for the transformation can be given as [82]

$$\sum_{k=0}^{\infty} (-1)^k f_k = \frac{1}{2} \left( f_0 - \frac{1}{2} \Delta f_0 + \frac{1}{4} \Delta^2 f_0 + \dots + (-1)^r 2^{-r} \Delta^r f_0 \right) \quad (\text{E.3})$$

where

$$\begin{aligned} \Delta^r f_k &= f_{k+r} - \binom{r}{1} f_{k+r-1} + \binom{r}{2} f_{k+r-2} \\ &\quad - \dots + (-1)^{r-1} \binom{r}{1} f_{k+1} + (-1)^r f_k \end{aligned} \quad (\text{E.4})$$

The convergence of Euler's transformation can be improved by adding some of the initial terms directly before the transformation. Note that increasing the number of previously added terms could improve the convergence.

### E.1.2 Shanks' Transformation

The idea behind Shanks' transformation is that the partial sums of a sequence can be treated as a mathematical transient, and it gives an approximation to the base of the transient which is the result of the infinite summation. The  $k$ th order

Shanks' transformation,  $e_k$ , is defined in the following form [83]:

$$B_{k,n} = e_k(A_n) = \begin{vmatrix} A_{n-k} & \cdots & A_{n-1} & A_n \\ \Delta A_{n-k} & \cdots & \Delta A_{n-1} & \Delta A_n \\ \Delta A_{n-k+1} & \cdots & \Delta A_n & \Delta A_{n+1} \\ \vdots & & \vdots & \vdots \\ \Delta A_{n-1} & \cdots & \cdots & \Delta A_{n+k-1} \\ \hline 1 & \cdots & 1 & 1 \\ \Delta A_{n-k} & \cdots & \Delta A_{n-1} & \Delta A_n \\ \Delta A_{n-k+1} & \cdots & \Delta A_n & \Delta A_{n+1} \\ \vdots & & \vdots & \vdots \\ \Delta A_{n-1} & \cdots & \cdots & \Delta A_{n+k-1} \end{vmatrix} \quad (\text{E.5})$$

where  $A_n$ 's are defined in (E.2) and  $\Delta A_n = A_{n+1} - A_n$ . For a special case,  $k = 1$ , (E.5) becomes

$$B_{1,n} = \frac{\begin{vmatrix} A_{n-1} & A_n \\ \Delta A_{n-1} & \Delta A_n \\ \hline 1 & 1 \\ \Delta A_{n-1} & \Delta A_n \end{vmatrix}}{\begin{vmatrix} 1 & 1 \\ \Delta A_{n-1} & \Delta A_n \end{vmatrix}} = \frac{A_{n+1}A_{n-1} - A_n^2}{A_{n+1} + A_{n-1} - 2A_n} \quad n = 1, 2, \dots \quad (\text{E.6})$$

and it is known as Aitken's  $\delta^2$  process [92]. The iterated Shanks' transformation performs the Shanks' transformation repeatedly until another transformation becomes impossible and is given as [83]

$$\begin{aligned} B_{k,n} &= e_k(A_n), & n &\geq k \\ C_{k,n} &= e_k(B_{k,n}), & n &\geq 2k \\ D_{k,n} &= e_k(C_{k,n}), & n &\geq 3k \\ &\vdots & & \end{aligned} \quad (\text{E.7})$$

Shanks' transformation (E.5) is usually applied by increasing the order  $k$  continuously until a predefined convergence criterion is satisfied. The evaluation of the determinant in (E.5) is time consuming for higher orders, and it can be

avoided by using the following transformation, called Wynn's  $\varepsilon$  algorithm [88]:

$$e_k(A) = \varepsilon_{2k}^{(n)} \quad (\text{E.8})$$

where

$$\begin{aligned} \varepsilon_{k+1}^{(n)} &= \varepsilon_{k-1}^{(n+1)} + \frac{1}{\varepsilon_k^{(n+1)} - \varepsilon_k^{(n)}} \quad n, k = 0, 1, \dots \\ \varepsilon_{-1}^{(n)} &= 0 \quad \varepsilon_0^{(n)} = A_n \quad n = 0, 1, 2, \dots \end{aligned}$$

where  $n$  and  $k$  are the indices for the terms and the order of the transformation, respectively, and only the even order transformations are used; the odd order ones are intermediate values. The importance of Wynn's  $\varepsilon$  algorithm stems from the fact that the evaluation of the determinant is reduced to a simple iterative equation. On the other hand, the  $\varepsilon$  algorithm given in (E.8), which is called "normal" form, has a disadvantage in that it may suffer from cancelation errors due to the computers arithmetic in the case of  $\varepsilon_k^{(n+1)} \cong \varepsilon_k^{(n)}$ . The cancelation errors occur because there is a subtraction process in the denominator of (E.8), and they can be avoided to some extent by using the progressive or particular rules of the algorithm [93].

### E.1.3 Method of Averages

This technique is especially suitable in evaluating the integrals which have a special form of [85]

$$I = \int_a^\infty f(\lambda) \cos(\lambda\rho) d\lambda \quad (\text{E.9})$$

where the function  $f(\lambda)$  is assumed to have the asymptotic form

$$\lim_{\lambda \rightarrow \infty} f(\lambda) = C\lambda^\alpha \quad (\text{E.10})$$

In addition, the partial integrals are defined as

$$I_m^1 = \int_a^{\lambda_m} f(\lambda) \cos(\lambda\rho) d\lambda \quad m = 1, 2, \dots, M \quad (\text{E.11})$$

where  $\lambda_m$ 's are the successive zeros of the oscillatory function  $\cos(\lambda\rho)$ . Then the transformation is given by

$$I_m^{l+1} = \frac{w_m^l I_m^l + w_{m+1}^l I_{m+1}^l}{w_m^l + w_{m+1}^l} \quad \begin{array}{l} l = 1, 2, \dots, M-1 \\ m = 1, 2, \dots, M-l \end{array} \quad (\text{E.12})$$

where

$$w_m^l = \left( \frac{\lambda_1}{\lambda_m} \right)^{\alpha+1-l} \quad (\text{E.13})$$

The value  $I_1^M$  is an approximation to the integral. This method can also be used in the integration of suitable Bessel functions whose asymptotic forms can be expressed as sinusoidal functions.

#### E.1.4 The $\Theta$ Algorithm

The  $\Theta$  Algorithm has been derived from the Wynn's  $\varepsilon$  Algorithm, and it can be expressed as [88, 89]

$$\begin{aligned} \Theta_{2k+2}^{(n)} &= \Theta_{2k}^{(n+1)} + \frac{[\Theta_{2k}^{(n+2)} - \Theta_{2k}^{(n+1)}][\Theta_{2k+1}^{(n+2)} - \Theta_{2k+1}^{(n+1)}]}{[\Theta_{2k+1}^{(n+2)} - 2\Theta_{2k+1}^{(n+1)} + \Theta_{2k+1}^{(n)}]} \\ \Theta_{2k+1}^{(n)} &= \Theta_{2k-1}^{(n+1)} + \frac{1}{\Theta_{2k}^{(n+1)} - \Theta_{2k}^{(n)}} \quad n, k = 0, 1, \dots \\ \Theta_{-1}^{(n)} &= 0 \quad \Theta_0^{(n)} = A_n \quad n = 0, 1, \dots \end{aligned} \quad (\text{E.14})$$

where  $A_n$ 's are the partial sums as defined in (E.2).

#### E.1.5 The Chebyshev-Toeplitz Algorithm

The Chebyshev-Toeplitz algorithm requires, first, one to transfer the partial sums to an intermediate series,  $t^{(n)}$ 's [86]:

$$\begin{aligned} t_{k+1}^{(n)} &= \varepsilon_k t_k^{(n)} + 2\varepsilon_k t_k^{(n+1)} - t_{k-1}^{(n)} \quad n, k = 0, 1, \dots \\ t_{-1}^{(n)} &= 0 \quad t_0^{(n)} = A_n \end{aligned} \quad (\text{E.15})$$

Then the final transformed series is obtained through

$$T_k^{(n)} = \frac{t_k^{(n)}}{\sigma_k} \quad n, k = 0, 1, 2, \dots \quad (\text{E.16})$$

where

$$\begin{aligned}\sigma_{k+1} &= 6\sigma_k - \sigma_{k-1} & k = 1, 2, 3, \dots \\ \sigma_0 &= 1 & \sigma_1 = 3\end{aligned}\quad (\text{E.17})$$

and

$$\begin{aligned}\varepsilon_k &= 1 & , & & k = 0 \\ \varepsilon_k &= 2 & , & & k > 0\end{aligned}$$

### E.1.6 The Poisson Transformation

The main idea behind the Poisson transformation is the reciprocal spreading property of the Fourier transformation; that is, if a function has a narrower support in one domain, it would have a wider support in the other domain. The Poisson transformation can be expressed as [90]

$$\sum_{n=-\infty}^{\infty} f(t + nT) = \frac{1}{T} \sum_{n=-\infty}^{\infty} e^{jn\omega_0 t} F(n\omega_0) \quad \omega_0 = \frac{2\pi}{T} \quad (\text{E.18})$$

and can be applied to double series [94]. Here, the transformation of the following doubly infinite series, which appears as the Green's function of two-dimensional periodic structure [95], is given as an example:

$$G_p = \frac{1}{4\pi} \sum_{m,n=-\infty}^{\infty} e^{-j\vec{k}_0 \cdot \vec{\rho}_{mn}} \frac{e^{jk_0 R_{mn}}}{R_{mn}} \quad (\text{E.19})$$

where

$$\vec{k}_0 = k_x \hat{x} + k_y \hat{y} + k_z \hat{z} \quad (\text{E.20})$$

$$\vec{\rho}_{mn} = mD_x \vec{x} + (mD_x \tan \Omega + nD_y) \vec{y} \quad (\text{E.21})$$

$$R_{mn} = \sqrt{|\vec{\rho} - \vec{\rho}' - \vec{\rho}_{mn}|^2 + |z - z'|^2} \quad (\text{E.22})$$

The Poisson transformation of (E.19) can be found by following the method described by [94] as

$$G_p = \sum_{m,n=-\infty}^{\infty} \frac{e^{-jk_p^{mn} \cdot (\vec{\rho} - \vec{\rho}') - jk_z^{mn} |z - z'|}}{2jk_z^{mn} D_x D_y} \quad (\text{E.23})$$

where

$$\vec{k}_\rho^{mn} = k_x^m \hat{x} + k_y^n \hat{y} \quad (\text{E.24})$$

$$k_x^m = \frac{2\pi m}{D_x} - \frac{2\pi n}{D_y \cot(\Omega)} + k_x \quad (\text{E.25})$$

$$k_y^n = \frac{2\pi n}{D_y} + k_y \quad (\text{E.26})$$

$$\begin{aligned} k_z^{mn} &= \sqrt{k_0^2 - k_\rho^{mn2}} \quad , \quad k_0^2 > k_\rho^{mn2} \\ k_z^{mn} &= -j\sqrt{k_\rho^{mn2} - k_0^2} \quad , \quad k_0^2 < k_\rho^{mn2} \end{aligned}$$

and  $D_x$  and  $D_y$  are the periodicity, and  $\Omega$  is the slant angle of the structure. Although (E.23) converges very fast for  $|z - z'| \gg 0$ , it converges rather slowly when  $|z - z'| \approx 0$ , as “on-plane” case. To achieve faster convergence in this case, other transformation methods are applied [95, 96]. and given in the next two sections.

### E.1.7 Ewald’s Transformation

This is a very powerful transformation method utilizing the complementary error function [91, 95] and expressing the series given in (E.19) as a summation of two different doubly infinite series:

$$G_p = G_1 + G_2$$

where  $G_1$  and  $G_2$  are given by

$$G_1 = \frac{1}{8\pi} \sum_{m,n=-\infty}^{\infty} \frac{e^{-j\vec{k}_0 \cdot \vec{\rho}_{mn}}}{R_{mn}} \sum_{\pm} e^{\pm jk_0 R_{mn}} \operatorname{erfc} \left( R_{mn} E \pm \frac{jk_0}{2E} \right) \quad (\text{E.27})$$

$$G_2 = \frac{1}{4jD_x D_y} \sum_{m,n=-\infty}^{\infty} \frac{e^{j\vec{k}_\rho^{mn} \cdot (\vec{\rho} - \vec{\rho}')} }{k_z^{mn}} \sum_{\pm} e^{\pm j|z-z'|k_z^{mn}} \operatorname{erfc} \left( j \frac{k_z^{mn}}{2E} \pm |z - z'| E \right) \quad (\text{E.28})$$

and  $E$  is a constant which has to be selected to allow an approximately equal convergence rate for  $G_1$  and  $G_2$ . Note that the complementary error function



in  $G_1$  and  $G_2$  makes these series converge rapidly, which is a consequence of the fact that the complementary error function behaves asymptotically like  $\exp(-z^2/z\sqrt{\pi})$  as  $z \rightarrow \infty$  for  $|\arg z| < 3\pi/4$ . To compute the complementary error function efficiently, one can use the algorithm given by [97].

### E.1.8 Kummer's Transformation

Kummer's transformation makes use of the fact that the rate of convergence of a series is governed by the asymptotic form of that series. Assume that  $f_a(n)$  is asymptotic to a function  $f(n)$ ; then Kummer's transformation gives [94, 98]

$$\begin{aligned} \sum_{n=-\infty}^{\infty} f(n) &= \sum_{n=-\infty}^{\infty} [f(n) - f_a(n)] + \sum_{n=-\infty}^{\infty} f_a(n) \\ &= G_1 + G_2 \end{aligned} \quad (\text{E.29})$$

Usually,  $f_a(n)$  is chosen in such a way that the last series in (E.29) has a known closed-form expression. However, one can also use the Poisson transformation over the last series if the closed-form expression is not known. Note that the first series in (E.29) converges rapidly since the asymptotic form is subtracted out. As an example, if Kummer's transformation is applied to the doubly infinite series given in (E.19),  $G_1$  and  $G_2$  are found in the following form:

$$G_1 = \frac{1}{4\pi} \sum_{m,n=-\infty}^{\infty} e^{-jk_0 \vec{\rho}_{mn}} \left[ \frac{e^{-jk_0 R_{mn}}}{R_{mn}} - \frac{e^{-jk_0 R'_{mn}}}{R'_{mn}} \right] \quad (\text{E.30})$$

$$G_2 = \sum_{m,n=-\infty}^{\infty} \frac{e^{-jk_z^{mn} \cdot (\vec{\rho} - \vec{\rho}')}}{2jk_z^{mn} D_x D_y} e^{-jk_z^{mn} (|z - z'| + E)} \quad (\text{E.31})$$

where

$$R'_{mn} = \sqrt{|\vec{\rho} - \vec{\rho}' - \vec{\rho}_{mn}| + (|z - z'| + E)^2} \quad (\text{E.32})$$

and the constant  $E$  is chosen as in the Ewald's transformation. Equation (E.31) can be thought of as the Poisson transformation for the off-plane case. It is also possible to perform additional acceleration on the first series by applying other transformation methods such as Wynn's  $\varepsilon$  algorithm [98].

### E.1.9 Method of Exponentials

This method is primarily used in evaluating the integrals which have the following form [15, 25]:

$$I = \int_a^\infty x^n \left\{ \begin{array}{l} H_0^{(2)}(\lambda x) \\ J_0(\lambda x) \\ \sin(\lambda x) \\ \cos(\lambda x) \end{array} \right\} F(x) dx \quad (\text{E.33})$$

where  $F(x)$  approximated with complex exponentials by using the generalized pencil of function method [22] or Prony's method [21]. Once the function  $F(x)$  is approximated by exponentials, the resultant integral will have the following form that can be evaluated analytically:

$$I = \sum_{i=0}^N \alpha_i \int_a^\infty x^n \left\{ \begin{array}{l} H_0^{(2)}(\lambda x) \\ J_0(\lambda x) \\ \sin(\lambda x) \\ \cos(\lambda x) \end{array} \right\} e^{-\beta_i x} dx \quad (\text{E.34})$$

The integrals involving Bessel and sinusoidal functions arise in a variety of problems in electromagnetics such as the spatial and spectral domain analysis of planarly stratified media via MoM. Although the numerical integration is possible utilizing an appropriate acceleration technique discussed above, the end result will be independent of  $\lambda$ , implying that for each  $\lambda$  one needs to reintegrate (E.33). This results in relatively large computation time when compared to the analytical evaluation in the method of exponentials for which the parameter  $\lambda$  appears explicitly in the resulting expression. As an example, consider the following integral [25]

$$G = \frac{1}{4\pi} \int_{-\infty}^{\infty} H_0^{(2)}(k_\rho \rho) \tilde{G}(k_\rho) k_\rho dk_\rho \quad (\text{E.35})$$

where  $G$  and  $\tilde{G}$  are the Green's functions in the spatial and spectral domain, respectively, and  $H_0^{(2)}$  is the Hankel function of second kind. The above integral cannot be evaluated analytically directly for the spectral domain Green's functions that are obtained easily for planarly stratified media. Therefore one can

take the integral analytically approximating the spectral domain Green's function by complex exponentials. Then the resultant integral can be evaluated using the Sommerfeld identity

$$\frac{e^{-jkr}}{r} = -\frac{j}{2} \int_{-\infty}^{\infty} H_0^{(2)}(k_\rho \rho) \frac{e^{-jk_z|z|}}{k_z} k_\rho dk_\rho \quad (\text{E.36})$$

## E.2 Results and Discussion

In this section, some numerical examples are given and the transformations used here are summarized in Table E.1. For all kinds of transformations, relative error is defined as

$$\zeta_r = \left| \frac{\tilde{S} - S}{S} \right| \quad (\text{E.37})$$

where  $S$  and  $\tilde{S}$  are the results obtained from direct summation calculated up to sufficient precision and transformation method, respectively. In addition, a convergence criterion is also used to terminate the iterative transformations and is defined as

$$\text{convergence} = \left| \frac{A_M^k - A_N^{k-1}}{A_N^k} \right| \quad (\text{E.38})$$

where  $A_n^k$  represents the  $k$ th level of any iterated transformation, and  $A_N$  and  $A_M$  are the last terms of the two consecutive iterations. The summation process is stopped when the convergence is less than a predefined number,  $\zeta_c$ . Note that the convergence checking must be performed several times to ensure proper convergence.

### E.2.1 Integration Involving Bessel Functions

Acceleration of an integral involving a Bessel function is considered here as an example for the application of the acceleration techniques discussed above. In the application of the series transformation methods to the integral (E.39), one has to convert the integral into a sequence, which can be achieved by integrating each cycle of (E.39) separately and assigning them to the terms of the series.

$$\int_0^{\infty} x J_1(x) dx = 1 \quad (\text{E.39})$$

Abbreviation	Transformation	Brief Explanation
Euler	Euler transformation	(E.3) and (E.4) are used
Shanks 1	$k$ th-order Shanks' transformation	The last term (depends on $N$ ) of the sequence obtained from (E.5)
Shanks 2	$k$ th-order iterated Shanks' transformation	The first term of the last possible sequence (depends on $N$ ) obtained from (E.7)
Wynn	Wynn's $\varepsilon$ algorithm	Implemented by using (E.8)
Averages	Method of averages	Implemented by using (E.12) and (E.13)
Theta	$\Theta$ algorithm	Implemented by using (E.14)
CT	Chebyshev-Toeplitz algorithm	Implemented by using (E.15) and (E.16)
Poisson	Poisson transformation	(E.23) is used
Ewald	Ewald's transformation	(E.27) and (E.28) are used
Kummer	Kummer transformation	(E.30) and (E.31) are used
Exponentials	method of exponentials	(E.33) and (E.34) are used.

Table E.1: Summary of the transformations used in the examples

For the purpose of comparison, the results, relative error versus number of terms, obtained from different acceleration methods are given in Figs. E.1 and E.2, and it is observed that the method of averages works better than the other techniques. However, the method of averages requires the asymptotic behavior of the integrand to determine the optimum weights; if the  $\alpha$  in (E.13) is chosen improperly, its convergence could be worse.

The next example is the calculation of the spatial domain Green's functions for the vector and the scalar potentials for a planarly layered medium whose parameters are  $\epsilon_r = 4.0$  and  $t = 0.02032$  cm (thickness of the substrate). For this problem the method of averages, found to be the best method for the previous example, is compared to the method of exponentials and the results, the magnitude of the Green's functions versus distance and the CPU time measured on a SUN SPARC-5G versus the number of evaluation points  $\rho$ , are given in Figs. E.3 and E.4, respectively. Since the Green's functions are usually used to

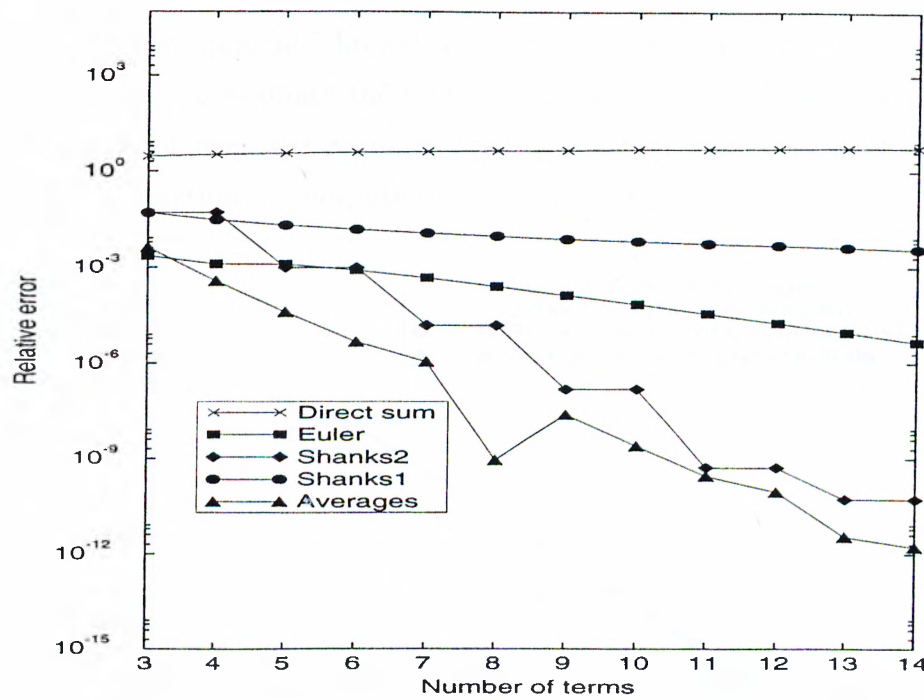


Figure E.1: Relative errors for the integral given in Eq. (E.39)

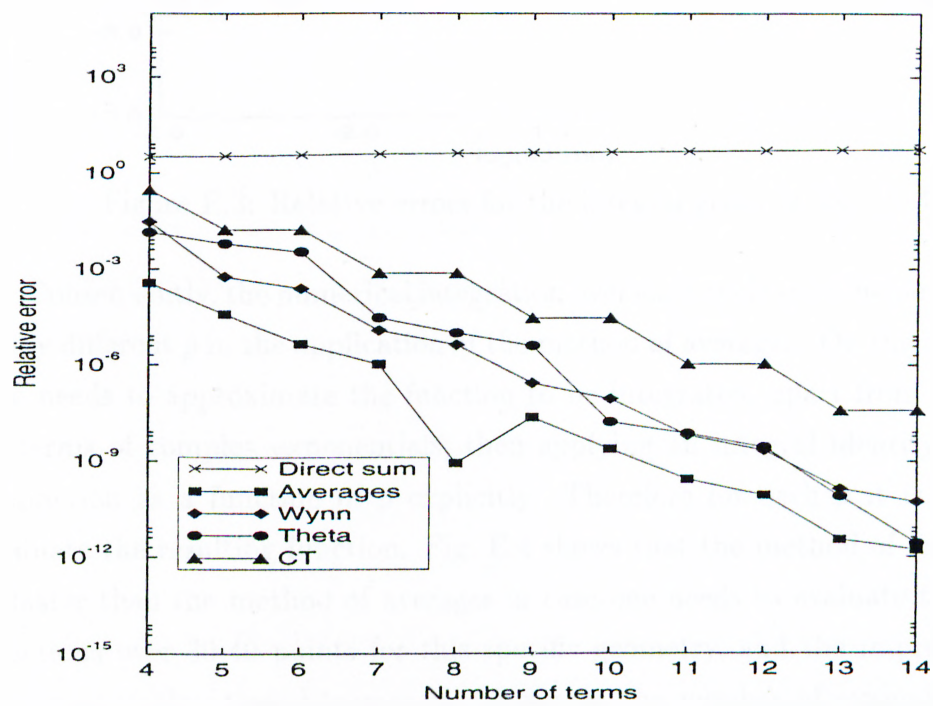


Figure E.2: Relative errors for the integral given in Eq. (E.39)

find the field components through a convolution integral for a current distribution, it is necessary to evaluate the Green's functions for hundreds of  $\rho$ 's. Moreover, the method of averages requires numerical integration over each cycle of the oscillatory function to compute the partial sums.

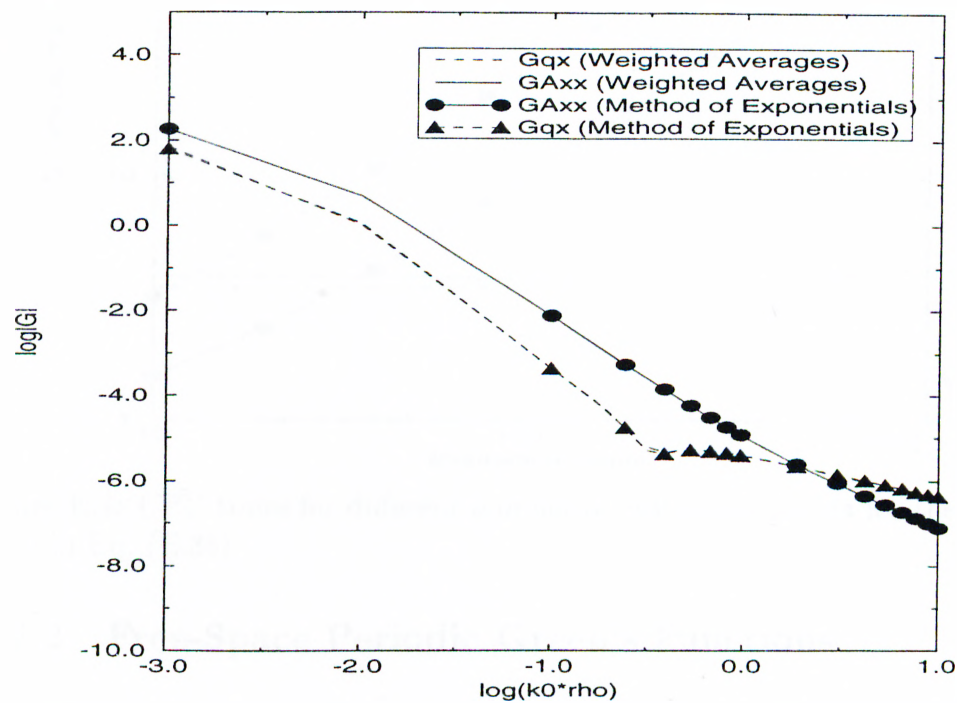


Figure E.3: Relative errors for the integral given in Eq. (E.35)

Consequently, the numerical integration over each cycle must be performed for every different  $\rho$  in the application of the method of averages. On the other hand, one needs to approximate the function to be integrated, apart from the kernel, in terms of complex exponentials; then applying an integral identity results in a function as a function of  $\rho$  explicitly. Therefore for each  $\rho$  it is enough to evaluate the resulting function. Fig. E.4 shows that the method of exponentials is faster than the method of averages in case one needs to evaluate the Green's functions over 30-40 points for this specific geometry, and the improvement in the computation time becomes significant as the number of evaluation points increases.



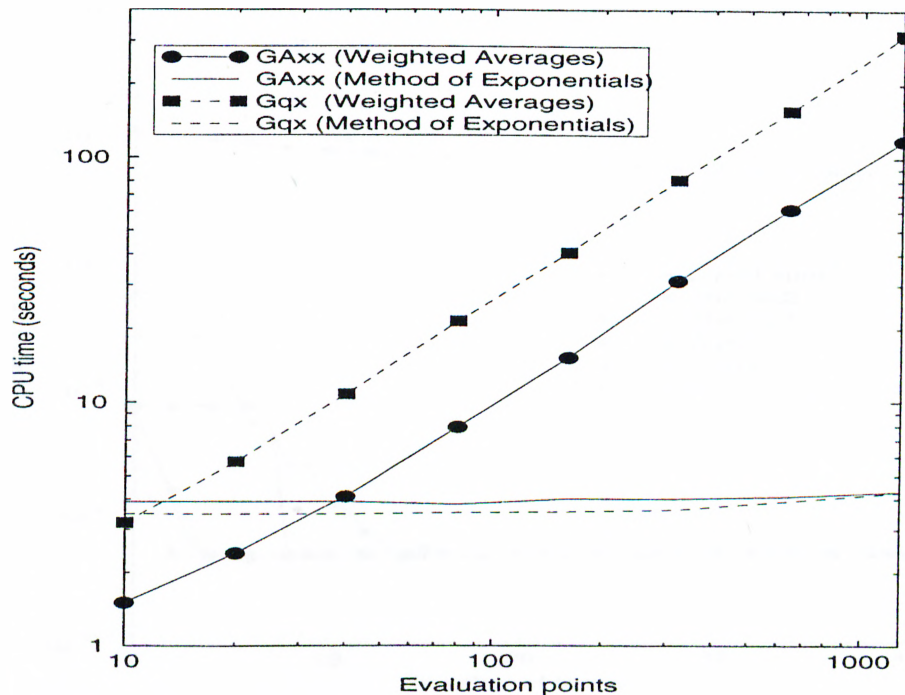


Figure E.4: CPU times for different number of evaluation points for the integral given in Eq. (E.35)

## E.2.2 Free-Space Periodic Green's Functions

In this section, acceleration of the infinite summations that appear in the free-space Greens' functions is demonstrated. Assuming a one-dimensional case first, the Green's function for a one-dimensional periodic array of point sources located  $d$  units apart in the  $z$  direction can be written as [85.98]

$$G = \frac{1}{4\pi} \sum_{m=-\infty}^{\infty} \frac{e^{-jkR_m}}{R_m} \quad (\text{E.40})$$

where

$$R_m = \left[ (x - x')^2 + (y - y')^2 + (z - md)^2 \right]^{1/2} \quad (\text{E.41})$$

The partial sums are obtained for  $x = y = 0.1\lambda$ ,  $z = 0.3\lambda$ ,  $\lambda = 1.0$  m, and  $d = 0.6$  m. Fig. E.5 demonstrates the results, relative error versus number of terms, obtained via some transformation techniques described in section 2.

Another example is the Green's function for one-dimensional line sources

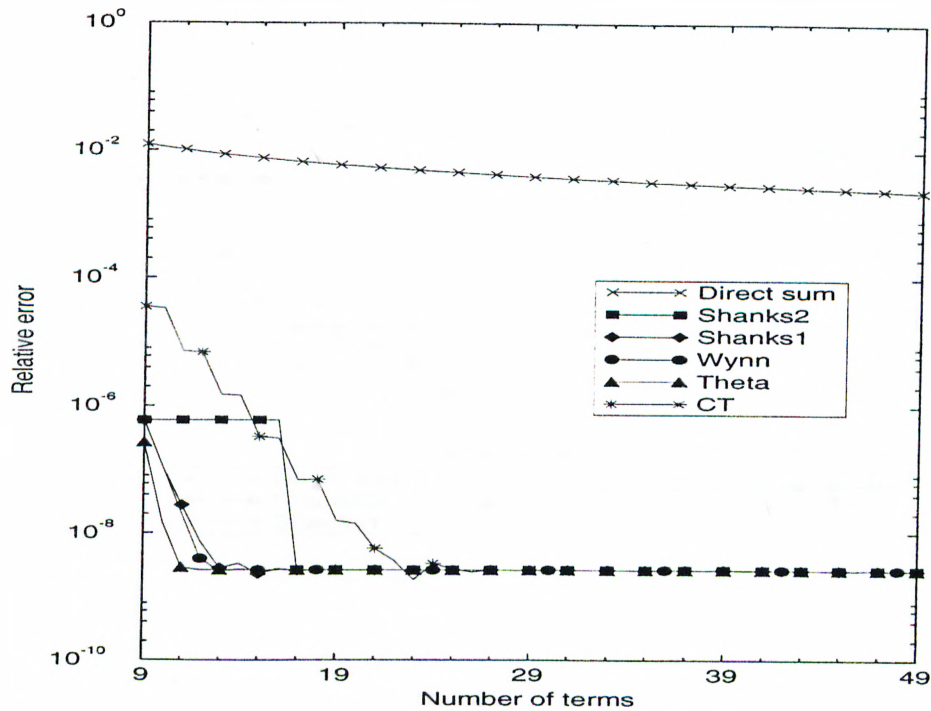


Figure E.5: Relative errors for the summation given in Eq. (E.40)

spaced  $d$  units apart along the  $x$  axis with the reference source located at  $(x', y')$

$$G = \sum_{m=-\infty}^{\infty} \frac{e^{-j(k_x + 2m\pi/d)(x-x')}}{j2dk_{ym}} e^{-jk_{ym}|y-y'|} \quad (\text{E.42})$$

where

$$\begin{aligned} k_{ym} &= \sqrt{k^2 - (k_x + 2m\pi/d)^2}, & k^2 > (k_x + 2m\pi/d)^2 \\ k_{ym} &= \frac{1}{j} \sqrt{(k_x + 2m\pi/d)^2 - k^2}, & k^2 < (k_x + 2m\pi/d)^2 \\ k_x &= k \sin(\Theta) \cos(\Phi) \end{aligned}$$

and the chosen parameters involved in the series are:  $d = 0.5\lambda$ ,  $x = 0.1\lambda$ ,  $\lambda = 1$  m,  $x' = y' = y = z' = 0$ , and  $k_x = 0$ . The results are shown in Figs. E.6 and E.7, and it can be concluded that Wynn's  $\varepsilon$  algorithm and Shanks' transformation work better than the other algorithms.

Finally, the free-space periodic Green's function for the two-dimensional case will be investigated. The transformations are performed for a nearly on-plane case for the summation given in (E.19) in order to have reasonable convergence times



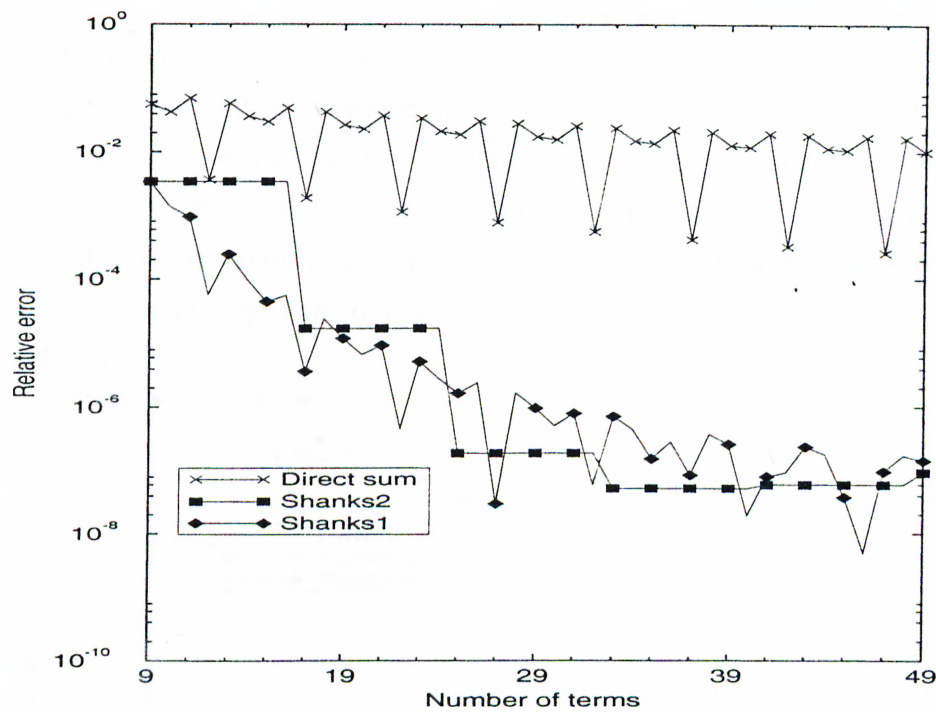


Figure E.6: Relative errors for the summation given in Eq. (E.42)

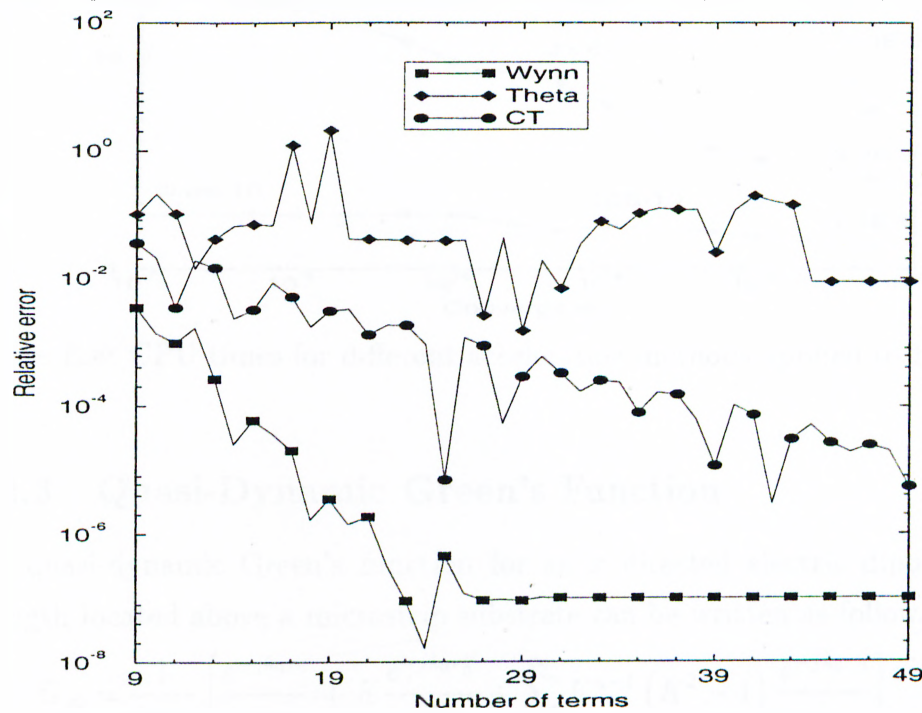


Figure E.7: Relative errors for the summation given in Eq. (E.42)

for the Kummer and Poisson transformations, which are further accelerated by the Wynn's  $\varepsilon$  algorithm. The results are given in Fig. E.8 for  $\lambda_0 = 1.0$  m,  $k_x = 3$ ,  $k_y = 2$ ,  $D_x = D_y = 0.7\lambda$ , and  $z = 0.004$ , and the numbers near the graphics show the relative errors at the corresponding convergence rate. As a final comment, as  $z \rightarrow 0$ , the time required for Ewald's transformation for the same convergence rate does not change considerably, whereas the other two methods slow down significantly.

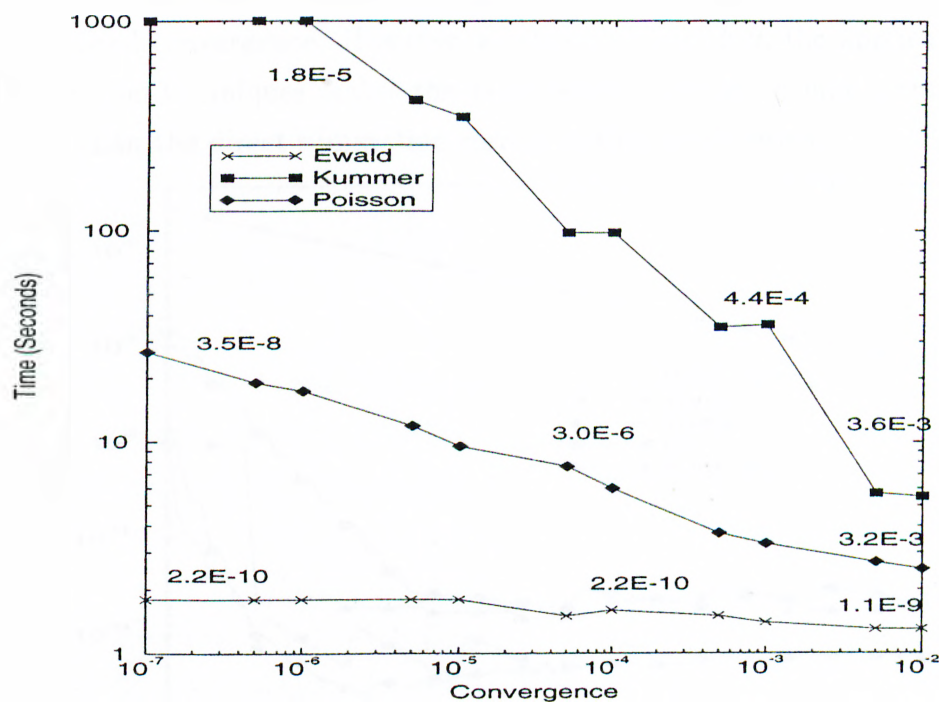


Figure E.8: CPU times for different acceleration methods applied to Eq. (E.19)

### E.2.3 Quasi-Dynamic Green's Function

The quasi-dynamic Green's function for an  $x$  directed electric dipole of unit strength located above a microstrip substrate can be written as follows [15]:

$$G_{q0} = \frac{1}{4\pi\varepsilon_0} \left[ \frac{e^{-jk_0 r_0}}{r_0} + K \frac{e^{-jk_0 r_0''}}{r_0''} + \sum_{n=1}^{\infty} K^{n-1} (K^2 - 1) \frac{e^{-jk_0 r_n}}{r_n} \right] \quad (\text{E.43})$$

where

$$r_0'' = \sqrt{\rho^2 + (z + z')^2}$$

$$r_n = \sqrt{\rho^2 + (z + z' + 2nh)^2}$$

and

$$K = \frac{1 - \varepsilon_r}{1 + \varepsilon_r}$$

For the evaluation of the summation in (E.43), the parameters chosen are:  $\rho = 3 \times 10^{-3}$  m,  $z = z' = 0$ ,  $h = 10^{-3}$ ,  $\varepsilon_r = 12.9$  and  $h/\lambda_0 = 0.05$ . As pointed out by [15], for this kind of geometry  $G_{q0}$  needs approximately 80 terms to ensure the desired convergence. However, as shown in Fig. E.9, the application of the acceleration techniques makes the same series converge in nine terms, which is better than the direct summation corresponding to 80 terms.

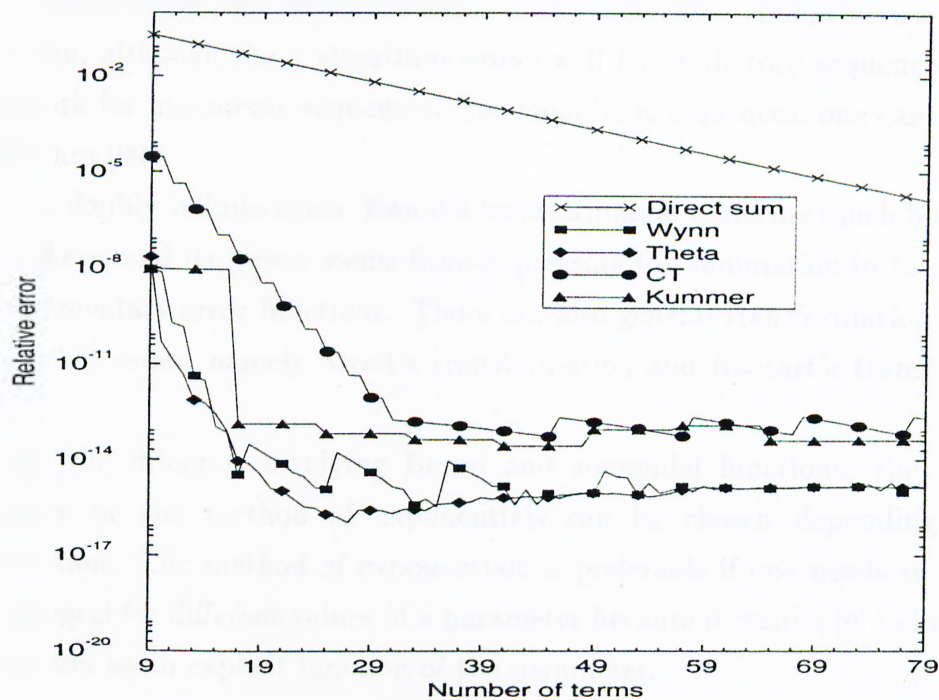


Figure E.9: Relative errors for the summation given in Eq. (E.43)

### E.3 Conclusion

Series transformation methods used in electromagnetic problems are studied and compared for some numerical examples in Electromagnetics. Among these

transformations, the Euler transformation can only be applied to alternating sequences; even then, other transformation methods may work better than the Euler transformation.

Wynn's  $\varepsilon$  algorithm seems to be working better when overall performance is considered and it is preferred over the direct application of higher-order Shanks' transformation because it eliminates the calculation of the determinants in Shanks' transformation. Although there is an exception (see Fig. E.7), the  $\Theta$  algorithm also gives good results in most cases.

On the other hand, the user must be aware of cancellation errors which might occur in the iterative transformations such as Wynn's  $\varepsilon$  algorithm. In the case of cancellation errors, the alternate forms of the algorithms should be used [93]. In addition, although the  $\varepsilon$  algorithm works well for oscillatory sequences, it does not work for monotonic sequences. For monotonic sequences, one can use the  $\rho$  algorithm [99].

For doubly infinite sums, Ewald's transformation performs much better than the others, and its power stems from expressing the summation in terms of the complementary error functions. There are also general transformation methods on double series, namely Streit's transformation and Haccart's transformation [93].

For the integrals involving Bessel and sinusoidal functions, the weighted averages or the method of exponentials can be chosen depending on the application. The method of exponentials is preferable if one needs to evaluate the integral for different values of a parameter because it results in a closed-form expression as an explicit function of the parameter.

# Bibliography

- [1] Robert M. Barrett, “Microwave printed circuits – the early years,” *IEEE Trans. on Microwave Theory Tech.*, vol. 32, pp. 983–990, Sep. 1984.
- [2] P. Silvester and P. Benedek, “Equivalent capacitance of microstrip open circuits,” *IEEE Trans. on Microwave Theory Tech.*, vol. MTT-20, pp. 511–516, Aug. 1972.
- [3] P. Benedek and P. Silvester, “Equivalent capacitance of microstrip gaps and steps,” *IEEE Trans. on Microwave Theory Tech.*, vol. MTT-20, pp. 729–733, Nov. 1972.
- [4] P. Silvester and P. Benedek, “Equivalent discontinuities capacitances for right-angle bends, t-junctions, and crossings,” *IEEE Trans. on Microwave Theory Tech.*, vol. MTT-21, pp. 341–346, May 1973.
- [5] Roger F. Harrington, “Matrix methods for field problems,” *IEEE Proceedings*, vol. 55, pp. 136–149, Feb. 1967.
- [6] R. F. Harrington. *Field Computations by Moment Methods*. New York: Macmillan, 1968.
- [7] J. Jin. *The Finite Element Method in Electromagnetics*. New York: John Wiley & Sons, Inc., 1993.
- [8] K. Kunz and R. Luebber. *The Finite Difference Time Domain Method for Electromagnetics*. Boca Raton, FL: CRC press. 1993.

- [9] Juan R. Mosig, "Arbitrarily shaped microstrip structures and their analysis with a mixed potential integral equation." *IEEE Trans. on Microwave Theory Tech.*, vol. MTT-36, pp. 314–323, Feb. 1988.
- [10] Ikmo Park, R. Mittra, and M. I. Aksun, "Numerically efficient analysis of planar microstrip configurations using closed-form green's functions," *IEEE Trans. on Microwave Theory Tech.*, vol. 43, pp. 394–400, Feb. 1995.
- [11] Krishna Naishadham and Todd W. Nuteson, "Efficient analysis of passive microstrip elements in mmics," *Int. J. MIMICAE*, vol. 4, pp. 219–229, July 1994.
- [12] Noyan Kinayman and M. I. Aksun, "Efficient and accurate em simulation technique for analysis and design of mmics," *Int J. MIMICAE*, accepted for publication.
- [13] A. Sommerfeld. *Partial Differential Equations in Physics*. Academic Press Inc., 1949.
- [14] J. R. Mosig and F. E. Gardiol, "Analytical and numerical techniques in the green's function treatment of microstrip antennas and scatterers." *IEE Proceedings*, vol. 130, pp. 175–182, Mar. 1983.
- [15] Y. L. Chow, J. J. Yang, D. G. Fang and G. E. Howard, "A closed-form spatial green's function for the thick microstrip substrate," *IEEE Trans. on Microwave Theory Tech.*, vol. 39, pp. 588–592, Mar. 1991.
- [16] M. I. Aksun and R. Mittra, "Spurious radiation from microstrip interconnects," *IEEE Trans. Electromagnetic Compat.*, vol. EMC-35, pp. 148–158, May 1993.
- [17] Lale Alatan, M. I. Aksun, Karthikeyan Mahadevan, and Tuncay Birand, "Analytical evaluation of the mom matrix elements," *IEEE Trans. on Microwave Theory Tech.*, vol. 44, pp. 519–525, Apr. 1996.

- [18] W. C. Chew. *Waves and Fields in Inhomogeneous Media*. Van Nostrand Reinhold, 1990.
- [19] G. Dural, and M. I. Aksun, "Closed-form green's functions for general sources and stratified media," *IEEE Trans. on Microwave Theory Tech.*, vol. 43, pp. 1545–1552, July 1995.
- [20] Noyan Kinayman and M. I. Aksun, "Comparative study of acceleration techniques for integrals and series in electromagnetic problems," *Radio Science*, vol. 30, pp. 1713–1722, Nov.-Dec. 1995.
- [21] S. L. Marple. *Digital Spectral Analysis with Applications*. Englewood Cliffs, NJ: Prentice-Hall, 1987.
- [22] Yingbo Hua and Tapan K. Sarkar, "Generalized pencil-of-function method for extracting poles of an em system from its transient response," *IEEE Trans. on Antennas and Propagation*, vol. AP-37, pp. 229–234, Feb. 1989.
- [23] V. K. Jain, T. K. Sarkar, and D. D. Weiner, "Rational modeling by pencil-of-function method," *IEEE Trans. on Acoust., Speech, Signal Processing*, vol. ASSP-31, pp. 564–573, June 1983.
- [24] M. I. Aksun and Raj Mittra, "Derivation of closed-form green's functions for a general microstrip geometry," *IEEE Trans. on Microwave Theory Tech.*, vol. 40, pp. 2055–2062, Nov. 1992.
- [25] M. I. Aksun, "A robust approach for the derivation of closed-form green's functions," *IEEE Trans. on Microwave Theory Tech.*, vol. 44, pp. 651–658, May 1996.
- [26] Miguel Marin, Sina Barkeshli and Prabhakar H. Pathak, "Efficient analysis of planar microstrip geometries using a closed-form asymptotic representation of the grounded dielectric slab green's function," *IEEE Trans. on Microwave Theory Tech.*, vol. MTT-37, pp. 669–679, Apr. 1989.

- [27] Miguel Marin, and Prabhakar H. Pathak, "An asymptotic closed-form representation for the grounded double-layer surface green's function." *IEEE Trans. on Antennas and Propagation*, vol. AP-40, pp. 1357-1366, Nov. 1992.
- [28] Krzysztof A. Michalski, "On the scalar potential of a point charge associated with a time-harmonic dipole in a layered medium," *IEEE Trans. on Antennas and Propagation*, vol. AP-35, pp. 1299-1301, Nov. 1987.
- [29] Krzysztof A. Michalski and Dalian Zheng. "Electromagnetic scattering and radiation by surfaces of arbitrary shape in layered media, part i: Theory," *IEEE Trans. on Antennas and Propagation*, vol. AP-38, pp. 335-344. Mar. 1990.
- [30] Noyan Kinayman and M. I. Aksun, "Efficient use of closed-form green's functions for the analysis of planar geometries with vertical connections," *IEEE Trans. on Microwave Theory Tech.*, vol. 45, pp. 593-603, May 1997.
- [31] Sonnet Software Inc. "Em user's manual.". 1995.
- [32] James C. Rautio, "A de-embedding algorithm for electromagnetics." *Int. J. MIMICAE*, vol. 1, pp. 282-287, 1991.
- [33] George V. Eleftheriades, and Juan R. Mosig, "On the network characterization of planar passive circuits using the method of moments," *IEEE Trans. on Microwave Theory Tech.*, vol. 44, pp. 438-445, Mar. 1996.
- [34] Tapan K. Sarkar, Zoran A. Maricevic, and Masoud Kahrizi, "An accurate de-embedding procedure for characterizing discontinuities," *Int. J. MIMICAE*. vol. 2, pp. 135-143, 1992.
- [35] Robert Kipp, and Chi H. Chan, "Triangular-domain basis functions for full-wave analysis of microstrip discontinuities," *IEEE Trans. on Microwave Theory Tech.*, vol. 41, pp. 1187-1194, June/July 1993.
- [36] Fred Gardiol. *Microstrip Circuits*. New York: John Wiley & Sons. Inc.. 1994.



- [37] Harlan Howe, JR. *Stripline Circuit Design*. Artech House, Inc., 1974.
- [38] K. C. Gupta, Ramesh Garg and I. J. Bahl. *Microstrip Lines and Slotlines*. Artech House, Inc., 1979.
- [39] James C. Rautio, "A new definition of characteristic impedance," in *IEEE MTT-S Digest*, pp. 761-764, 1991.
- [40] James Mason Carroll and Kai Chang, "Full-wave convergence analysis of microstrip transmission parameters," *Int. J. MIMICAE*, vol. 4, pp. 140-147, Apr. 1994.
- [41] J. R. James and G. J. Wilson, "Microstrip antennas and arrays, pt. i - fundamental action and limitations," *IEE J. Microwaves, Optics, and Acoustics*, vol. 1, pp. 165-174, 1977.
- [42] Keith R. Carver and James W. Mink, "Microstrip antenna technology," *IEEE Trans. on Antennas and Propagation*, vol. 29, pp. 2-24, Jan. 1981.
- [43] R. J. Mailloux, J. F. McIlvanna and N. P. Kernweis, "Microstrip array technology," *IEEE Trans. on Antennas and Propagation*, vol. AP-29, pp. 25-37, 1981.
- [44] J. R. James, "Printed antennas," in *Proc. SBMO Int. Microwave Symp., Rio de Janeiro, Brazil*, pp. 597-606, 1987.
- [45] J. Van Bladel. *Singular Electromagnetic Fields and Sources*. Oxford Science Publications, 1991.
- [46] Y. T. Lo and S. W. Lee (Editors). *Antenna Handbook*. New York: Van Nostrand Reinhold, 1993.
- [47] M. D. Deshpande and N. K. Das, "Rectangular microstrip antenna for circular polarization," *IEEE Trans. on Antennas and Propagation*, vol. AP-34, pp. 744-746, May 1986.

- [48] Daniel H. Schaubert, Frederick G. Farrar, Arthur Sindoris and Scott T. Hayes, "Microstrip antennas with frequency agility and polarization diversity," *IEEE Trans. on Antennas and Propagation*, vol. AP-29, pp. 118–123, Jan. 1981.
- [49] Brian C. Wadell. *Transmission Line Design Handbook*. Artech House, Inc., 1991.
- [50] H. F. Pues and A. R. Van de Capelle, "Wide-band impedance-matched microstrip resonator antennas," in *IEE Second Inter. Conf. on Ant. and Propagation, Pt. 1*, pp. 402–405, 1981.
- [51] Hugo F. Pues, Antoine R. Van De Capelle, "An impedance-matching technique for increasing the bandwidth of microstrip antennas," *IEEE Trans. on Antennas and Propagation*, vol. AP-37, pp. 1345–1354, Nov. 1989.
- [52] Hongming An, Bart K. J. C. Nauwelaers, and Antoine R. Van de Capelle, "Broadband microstrip antenna design with the simplified real frequency design," *IEEE Trans. on Antennas and Propagation*, vol. 42, pp. 129–136, Feb. 1994.
- [53] C. Wood, "Improved bandwidth of microstrip antennas using parasitic elements," *IEE Proceedings*, vol. 127, pt. H., pp. 231–234, 1980.
- [54] G. Kumar and K. C. Gupta, "Non-radiating edges and four-edges gap-coupled with multiple resonator, broadband microstrip antennas," *IEEE Trans. on Antennas and Propagation*, vol. AP-33, pp. 173–178, 1985.
- [55] G. Dubost, G. Beauquet, J. Rocquencourt, and G. Bonnet, "Patch antenna bandwidth increase by means of a director." *Electronic Letters*, vol. 22, pp. 1345–1347, 1986.
- [56] R. Q. Lee, K. F. Lee, and J. Bobinchak, "Characteristics of a two-layer electromagnetically coupled rectangular patch antenna," *Electronic Letters*, vol. 23, pp. 1070–1072, Sep. 1987.

- [57] Georg Splitt and Marat Davidovitz, "Guidelines for design of electromagnetically coupled microstrip patch antennas on two-layer substrates," *IEEE Trans. on Antennas and Propagation*, vol. AP-38, pp. 1136–1140, July 1990.
- [58] D. M. Pozar and B. Kaufman, "Increasing the bandwidth of a microstrip antenna by proximity coupling," *Electronic Letters*, vol. 23, pp. 368–369, Apr. 1987.
- [59] R. Levy, and S. B. Cohn, "A history of microwave filter research, design and development," *IEEE Trans. on Microwave Theory Tech.*, vol. 32, pp. 1055–1067, Sep. 1984.
- [60] Kai Chang (Editor). *Handbook of Microwave and Optical Components, Volume I*. J. Wiley, New York, 1989.
- [61] Jia-Sheng Hong, and Michael J. Lancaster, "Couplings of microstrip square open-loop resonators for cross-coupled planar microwave filters," *IEEE Trans. on Microwave Theory Tech.*, vol. 44, pp. 2099–2109, Dec. 1996.
- [62] Bharathi Bhat and Shiban K. Koul. *Stripline-like Transmission Lines for Microwave Integrated Circuits*. Wiley Eastern Limited, 1989.
- [63] Wolfgang Schwab, Frank Boegelsack, and Wolfgang Menzel, "Multilayer suspended stripline and coplanar line filters," *IEEE Trans. on Microwave Theory Tech.*, vol. MTT-42, pp. 1403–1407, July 1994.
- [64] W. F. Richards, Y. T. Lo and D. Harrison, "An improved theory for microstrip antennas and applications," *IEEE Trans. on Antennas and Propagation*, vol. AP-29, pp. 38–46, 1981.
- [65] William F. Richards, Y. T. Lo, "Theoretical and experimental investigation of a microstrip radiator with multiple lumped linear loads," *Electromagnetics*, vol. 3, pp. 371–387, 1983.

- [66] Karthikeyan Mahadevan and Hesdam A. Auda, "Electromagnetic field of a rectangular patch of uniform and linear distributions of current," *IEEE Trans. on Antennas and Propagation*, vol. 37, pp. 1503–1509, Dec. 1989.
- [67] Tom Dhaene, Jan Ureel, Niels Fache, and Daniel De Zutter, "Adaptive frequency sampling algorithm for fast and accurate s-parameter modeling of general planar structures," in *IEEE MTT Int. Symposium*, pp. 1427–1430, 1995.
- [68] Sharath M. Narayana, Girish Rao, Raviraj Adve, Tapan K. Sarkar, Vincent C. Vannicola, Michael C. Wicks, and Steven A. Scott, "Interpolation/extrapolation of frequency domain responses using the hilbert transform," *IEEE Trans. on Microwave Theory Tech.*, vol. MTT-44, pp. 1621–1627, Oct.. 1996.
- [69] John W. Bandler, Radoslaw M. Biernacki, Shao Hua Chen, Piotr A. Grobelny, and Ronald H. Hemmers. "Space mapping technique for electromagnetic optimization," *IEEE Trans. on Microwave Theory Tech.*, vol. MTT-42, pp. 2536–2544, Dec. 1994.
- [70] J. W. Bandler, R. M. Biernacki, Q. Cai, S. H. Chen, P. A. Grobelny, and D. G. Swanson, "Heterogeneous parallel yield-driven electromagnetic cad," in *IEEE MTT-S Digest*, pp. 1085–1088, 1995.
- [71] J. W. Bandler, R. M. Biernacki, S. H. Chen, R. H. Hemmers, and K. Madsen, "Aggressive space mapping for electromagnetic design," in *IEEE MTT-S Digest*, pp. 1455–1458, 1995.
- [72] L. Davis (Editor). *Genetic Algorithms and Simulated Annealing*. Morgan Kaufmann Publishers, Inc., 1987.
- [73] J. H. Holland, "Genetic algorithms," *Scientific American*, vol. , pp. 66–72. July 1992.
- [74] D. E. Goldberg. *Genetic Algorithms*. New York: Addison Wesley, 1989.

- [75] Randy L. Haupt, "An introduction to genetic algorithms for electromagnetics," *IEEE Antennas and Propagation Magazine*, vol. 37, pp. 7–15, Apr. 1995.
- [76] Lale Alatan. *Use of Computationally Efficient MoM in the Analysis and Desing of Microstrip Antennas*. PhD thesis, Department of Electrical and Electronics Engineering, Middle East Technical University, Ankara, Turkey, 1997.
- [77] Krishna Naishadham and Pradeep Misra, "Order recursive gaussian elimination and efficient cad of microwave circuits," in *IEEE MTT-S Digest*, pp. 1435–1438, 1995.
- [78] Krishna Naishadham and Pradeep Misra, "Order recursive method of moments (ormom) for iterative design applications," *IEEE Trans. on Microwave Theory Tech.*, vol. 44, pp. 2595–2604, Dec. 1996.
- [79] M. L. Van Blaricum and R. Mittra, "A technique for extracting the poles and residues of a system directly from its transient response," *IEEE Trans. on Antennas and Propagation*, vol. AP-23, pp. 777–781, Nov. 1975.
- [80] M. L. Van Blaricum and R. Mittra, "Problem and solutions associated with prony's method for processing transient data," *IEEE Trans. on Antennas and Propagation*, vol. AP-26, pp. 174–182, Jan. 1978.
- [81] V. H. Rumsey, "Reaction concept in electromagnetic theory," *The Physical Review*, vol. 94, pp. 1483–1491, 1954.
- [82] F. B. Hildebrand. *Introduction to Numerical Analysis*. McGraw-Hill, 1974.
- [83] Daniel Shanks, "Non-linear transformations of divergent and slowly convergent sequences," *J. Math. Phys.*, vol. 34, pp. 1–42, 1955.
- [84] Surendra Singh and Ritu Singh, "On the use of shanks' transform to accelerate the summation of slowly converging series," *IEEE Trans. on Microwave Theory Tech.*, vol. 39, pp. 608–610, Mar. 1991.

- [85] Juan R. Mosig and Fred E. Gardiol, "A dynamical radiation model for microstrip structures," *Advances in Electronics and Electron Physics*, vol. 59, pp. 139–233, 1982.
- [86] J. Wimp, "Toeplitz arrays, linear sequence transformations, and orthogonal polynomials," *Numer. Math.*, vol. 23, pp. 1–17, 1974.
- [87] Surendra Singh and Ritu Singh, "On the use of chebyshev-toeplitz algorithm in accelerating the numerical convergence of infinite series," *IEEE Trans. on Microwave Theory Tech.*, vol. 40, pp. 171–173, Jan. 1992.
- [88] C. Brezinski, "Some new convergence acceleration methods," *Mathematics of Computation*, vol. 39, pp. 133–145, July 1982.
- [89] Surendra Singh and Ritu Singh, "A convergence acceleration procedure for computing slowly convergent series," *IEEE Trans. on Microwave Theory Tech.*, vol. 40, pp. 158–171, Jan. 1992.
- [90] Athanasios Papoulis. *The Fourier Integral and Its Applications*. McGraw-Hill, 1962.
- [91] Kirk E. Jordan, Gerard R. Richter and Ping Sheng, "An efficient numerical evaluation of the green's function for the helmholtz operator on periodic structures," *Journal of Computational Physics*, vol. 63, pp. 222–235, 1986.
- [92] William H. Press, Brian P. Flannery, Saul A. Teukolsky, and William T. Vetterling. *Numerical Recipes*. Cambridge University Press, 1986.
- [93] C. Brezinski and R. Zaglia. *Extrapolation Methods. Theory and Practice*. New York: North Holland, 1991.
- [94] R. Lampe, P. Klock and P. Mayes, "Integral transforms useful for the accelerated summation of periodic free-space green's functions," *IEEE Trans. on Microwave Theory Tech.*, vol. 33, pp. 734–736, Aug. 1985.

- [95] Eric Michielssen. *Electromagnetic Plane Wave Scattering from Periodically Loaded Cylinders and Doubly Periodic Slabs*. PhD thesis, Graduate College of the University of Illinois at Urbana-Champaign, Illinois, U.S.A. 1992.
- [96] Roy E. Jorgenson and Raj Mittra, “Efficient calculation of the free-space periodic green’s function,” *IEEE Trans. on Antennas and Propagation*, vol. 38, pp. 633–642, May 1990.
- [97] W. Gautschi, “Efficient computation of the complex error function,” *SIAM Journal of Numerical Analysis*, vol. 7, pp. 187–198, Mar. 1970.
- [98] Surendra Singh and Ritu Singh, “Application of transforms to accelerate the summation of periodic free-space green’s functions,” *IEEE Trans. on Microwave Theory Tech.*, vol. 38, pp. 1746–1748, Nov. 1990.
- [99] Surendra Singh and Ritu Singh, “On the use of  $\rho$  algorithm in series acceleration,” *IEEE Trans. on Antennas and Propagation*, vol. 39, pp. 1514–1517, 1991.

# Vita

Noyan Kinayman was born in Ankara, Turkey, on November 22, 1968. He received the B.Sc. and M.Sc. degrees both in Electrical & Electronic Engineering from Middle East Technical University (METU), Ankara, in 1990 and 1993 respectively.

During the period June 1990 to September 1994, he worked in the Department of Preparation to Production, ASELSAN Military Electronics Inc., as a design and test engineer. His major duty was to design computer controlled and manual RF test systems which are used on the tests of various military and non-military radios. Here, he also designed a general purpose radio test program running under MS-WINDOWS using C++ programming language.

In October 1994, he joined to the Electrical and Electronics Engineering Department of Bilkent University as research and teaching assistant.

His major professional interest is the numerical solutions of Electromagnetic problems.